# Faculdade de Engenharia da Universidade do Porto

**U.**PORTO
FEUP FACULDADE DE ENGENHARIA
UNIVERSIDADE DO PORTO

# Antenna array design for future generation of mobile communications

José Miguel Sousa Neves

Versão Final

Dissertação realizada no âmbito do
Mestrado Integrado em Engenharia Electrotécnica e de Computadores
Major Telecomunicações

Orientador: Professor Doutor Henrique Manuel de Castro Faria Salgado
Co-orientador: Doutor Luís Manuel de Sousa Pessoa

12 Março 2021

# Resumo

Nos últimos anos, devido a um crescimento exponencial no tráfego de dados sem fios, mais uma vez, a necessidade de taxas de bits mais elevadas surgiu de novo. Na transição de 4G para 5G, houve um movimento em direção ao espectro das ondas milimétricas, motivado pela necessidade de uma largura de banda maior. Hoje em dia, no caminho para o 6G, a tendência é atingir zonas do espectro de frequência ainda mais elevadas, nomeadamente, a região dos sub-terahertz (sub-THz), a fim de mitigar a escassez de espectro e as limitações de capacidade dos sistemas de comunicação sem fios atuais.

Esta dissertação está focada na simulação, fabricação e caracterização de uma matriz de antenas patch 4x4, de complexidade simples e custo baixo, de modo a operar a uma frequência central de 100 GHz, pelo que é necessário começar com um estudo do estado de arte no domínio sub-terahertz, como bem como a simulação e análise de vários tipos de métodos de alimentação de antenas e linhas de transmissão, para inferir sobre sua fiabilidade a essas frequências. De modo a validar os resultados de simulação, a antena/matriz de antenas final foram fabricadas e medidas numa câmara anecóica, com o intuito dar uma perspetiva melhor sobre a proximidade entre resultados simulados e medidos.

Embora a pesquisa científica tem sido rigorosa e o desenvolvimento de dispositivos e sistemas no domínio dos sub-THz ainda estejam a decorrer, é esperado que o trabalho realizado nesta dissertação possa fornecer uma compreensão melhor das questões, dificuldades, alternativas e abordagens a serem adotadas no projeto e fabrico de antenas/matrizes de antenas que sejam viáveis e consistentes no espectro de frequência sub-THz.

Este trabalho insere-se no âmbito das atividades em curso do projeto europeu TERAPOD (https://terapod-project.eu), no qual o INESC TEC é um dos participantes, sendo o responsável pela tarefa das antenas a implementar.

# Abstract

In recent years, due to an exponential growth in wireless traffic data yet again, the need for higher bit rates has resurfaced. In the 4G to 5G transition, there was a move towards millimetre wave spectrum motivated by the need for higher bandwidth. Now the trend towards 6G is to move to even higher zones of the frequency spectrum, into the sub-terahertz (sub-THz) region, in order to mitigate the spectrum scarcity and capacity limitations of current wireless communication systems.

This dissertation is focused on design, manufacture and characterization of a simple and cost effective 4x4 patch antenna array at an operation of 100 GHz, which is required to start off with a study of the state-of-art in the sub-terahertz domain as well as the simulation and analysis of multiple types of antenna feeding methods and transmissions lines to infer on their reliability at these frequencies. To validate simulation results, the final antenna/array were manufactured and measured in an anechoic chamber to give better insight on the proximity between simulated and measured results.

While rigorous scientific research and development in sub-THz devices and systems is still in progress, hopefully the work done in this thesis can provide a better understanding of the issues, difficulties, alternatives and approaches to take when designing and fabricating antenna elements/antenna arrays that are viable and feasible in the sub-THz frequency spectrum.

This work is part of the ongoing activities within the European TERAPOD project (https://terapod-project.eu), in which INESC TEC is one of the active participants, responsible for the design of the antennas to be implemented.

# Acknowledgements

Many people played an important role during the course of this dissertation, to whom I would like to give my sincere thanks, especially to:

Professor Henrique Salgado for supervising this thesis, providing with the most valuable help, insight and knowledge as well as careful guidance and suggestions throughout the making of this thesis.

Doutor Luís Pessoa for co-supervising and giving his expert advice and experience on the usage of measurement equipment, as well as, on antenna design approaches.

Doutor Hugo Santos for his help with the correct usage of simulation tools such as HFSS and ADS.

My family, namely my parents José and Cândida Neves and my sister Catarina Neves for the support and moral boost during some stressful and hard times during this thesis.

FEUP and INESC TEC for providing with financial resources for the manufacturing process and high-end facilities and equipment for experimental measurement process.

João Araújo for his precious assistance in the laboratory, as well as, the providing of essential work tools, and Henrique Rocha for his help on the anechoic chamber positioner and the printing of 3D parts for measurement purposes.

All the other people of FEUP and INESC TEC that I met during my thesis journey, briefly or not, provided help, kindness, availability and some type of expert advice.

# List of Contents

# List of Figures

xiii

# List of Tables

# Acronyms

In this section, a list of acronyms used in this document is presented, as follows:

| | |
|---|---|
| *ADS* | Advanced Design System |
| *AF* | Array factor |
| *AUT* | Antenna under test |
| *BW* | Bandwidth |
| *CPW* | Coplanar waveguide |
| *DC* | Direct current |
| *DCN* | Data centre networks |
| *DFW* | Dielectric filled waveguide |
| *EF* | Element factor |
| *EM* | Electromagnetic |
| *FEUP* | *Faculdade de Engenharia da Universidade do Porto* |
| *FNBW* | First-null beamwidth |
| *FW* | Fractional bandwidth |
| *GCPW* | Grounded coplanar waveguide |
| *HFSS* | High Frequency Structure Simulator |
| *HPBW* | Half-power beamwidth |
| *INESC TEC* | *Instituto de Engenharia de Sistemas e Computadores, Tecnologia e Ciência* |
| *MIMO* | Multiple input multiple output |
| *PCB* | Printed circuit board |
| *SIW* | Substrate integrated waveguide |
| *SOLT* | Short Open Load Through |
| *TE* | Transverse electric |
| *TEM* | Transverse electromagnetic |
| *TM* | Transverse magnetic |
| *TRL* | Through Reflect Line |
| *VNA* | Vector network analyzer |
| *VSWR* | Voltage standing wave ratio |
| *4G* | Fourth generation of cellular communications |
| *5G* | Fifth generation of cellular communications |
| *6G* | Sixth generation of cellular communications |

# Chapter 1: Introduction

## 1.1. Background and Motivation

The demand for bandwidth in wireless communication has been escalating quite quickly recently, essentially caused by the increased data traffic necessities from network users, translating into higher wireless data-rate requirements. In order to achieve the expected demands of data rates in the range of 100 Gbit/s in the near future, a shift towards the sub-terahertz/terahertz band is needed. Despite this side of the spectrum is still relatively unexplored for communications purposes, its transition is required in order to capitalize on its huge bandwidths and quench the scarcity and limitations on capacity in current wireless communication systems and enabling a plethora of long-awaited applications in diverse fields **[1] [2] [3]**.

The introduction of terahertz wireless links within Data Centres is one of the highly regarded steps in high bandwidth short range wireless links. In order to store and process an unprecedented amount of data, today's Data Centre Networks (DCNs) have to keep up such traffic intensity, which is proving to be very challenging, given that DCNs have to deploy enormous length of wires to interconnect a big amount of servers and switches, which causes drawbacks such as high cabling cost and complexity, lack of bandwidth efficiency and expensive cooling costs. As such, even though two main technologies are currently being used: free-space optics and 60 GHz wireless communications, the implementation of sub-terahertz short range wireless links would most certainly alleviate some of the challenges faced by DCNs **[4] [5] [6] [7]**.

Antenna figures-of-merit have been investigated using particular substrates, such as Benzocyclobutene and Polyimide, at an operation frequency of 300 GHz within the sub-Thz domain, leading to a conclusion that substrate thickness has a big impact on efficiency and bandwidth, so care must be taken when designing antennas at these frequencies **[8]**.

Many studies involving the design of differential series-fed antenna arrays for beam-steering applications to work at a frequency of 77 GHz have been developed, providing more

concrete knowledge and techniques regarding phased-array antennas, which continue to be frequently used at millimetre wave frequencies **[9]**.

In order to pursue the proper use of the sub-terahertz/terahertz frequency spectrum, many topics need to be mitigated, such as challenges that arise in devices and systems, protocols and standardization regarding the terahertz bands, which means that an interdisciplinary approach is best suited. One of those topics, namely sub-terahertz devices, in this case, sub-terahertz antennas, is the basis of this dissertation theme.

## **1.2.** Work Goals

The main goal of this dissertation is to design, manufacture and characterize a cost effective four by four antenna array matrix capable of allowing wireless communication links at a frequency of 100 GHz, which is located in a low-loss transmission window, hence this frequency was chosen as a starting point for this work. As such, in order to achieve said objective, an in-depth study is needed regarding the selection of the best suited type of antenna for a sub-terahertz short range wireless link scenario, the choice of parameter values to fulfill DCN requirements for a feasible communication link, the design rules and manufacturing limitations of antennas as well as the standard test procedures regarding the antenna measurement system, to fully and correctly characterize an antenna array **[10] [11]**.

After a proper study of what was previously mentioned, a first approach of a 3D electromagnetic simulation will be performed on an antenna element, followed by a sixteen antenna element matrix simulation and analysis of the obtained simulation results. Afterwards, manufacturing of the antenna matrix will commence, which later on will be characterize in an anechoic chamber, which was manufactured based on the work presented in **[12]**, allowing extraction of measurement results.

## **1.3.** Dissertation Structure

This thesis is composed by five chapters. Chapter 1, which is the current chapter, presents the motivation, background and work goals of this thesis, followed by Chapter 2, which gives the fundaments of antenna theory and provides a better understanding of the work done. In Chapter 3, the design of a CPW antenna element fed by a squared loop feed is presented, as well as, the design of a TRL calibration kit to properly perform experimental measurements of the antenna element. Chapter 4 depicts the design, simulation and measurement of a 4x4 differential series-fed microstrip patch antenna array, using a SIW feed network in conjunction with GCPW-SIW and SIW-microstrip transitions, including also the design and manufacture of a TRL calibration kit to be able to experimentally evaluate the reflection coefficient and

radiation pattern of the manufactured antenna array. Finally, in Chapter 5, the final conclusions of the thesis and future work are presented.

# Chapter 2: Antenna Fundamentals

## 2.1. Introduction

In this chapter, the state of the art is presented, mostly related to what is needed as a basic understanding in order to accomplish the desired objectives within this dissertation. Firstly, the antenna fundamentals are reviewed, namely the main important antenna parameters, will be described. The understanding of these parameters is quite important as they relate in most instances to measurable experimental parameters that lets one to assess the performance of an antenna or if it complies with the initial design requirements.

Secondly, array configurations are also discussed as this complies with the objective of this work. In this chapter only N-element linear arrays with uniform amplitude and spacing (linear and planar array) are discussed. Also some focus is given to microstrip antennas and its basic parameters, given their ease of fabrication and printed circuit technology (PCB) antenna measurement techniques.

An antenna is defined as: *That part of a transmitting or receiving system that is designed to radiate or to receive electromagnetic waves* [13].

In order to get a basic and clear understanding of how antennas work, how to group them, how to design them in a PCB and how to measure them after manufacture, a study of these topics was conducted and presented down below.

## 2.2. Antenna Parameters

In order to evaluate the performance of an antenna, the definition of various parameters are required, although some parameters are interrelated and can be expressed as a function of others. Some of the main used performance parameters are described.

### 2.2.1. Radiation Pattern

An antenna radiation pattern is known as the mathematical function or graphical representation of the radiation properties of the antenna and it's usually plotted as a function of the spherical directional angles φ (angle for the azimuth plane), θ (angle for the elevation plane) and usually in the far-field region.

In relation to radiation pattern lobes, they can be sub-divided in types of lobes, two of the most important ones being:

- Main (major) lobe: is known as a radiation lobe containing the direction of maximum radiation. In the case of multilobed or slip-beam radiation patterns, there may exist more than one of these type of lobes.
- Side lobe: is defined as a radiation lobe in any direction other than of the main lobe. A side lobe level is defined as the amplitude of the side lobe relative the main lobe and it's expressed usually in decibels.

The figure down below (Fig. 2.1) shows a linear two-dimensional power pattern in function of the elevation plane angle θ:
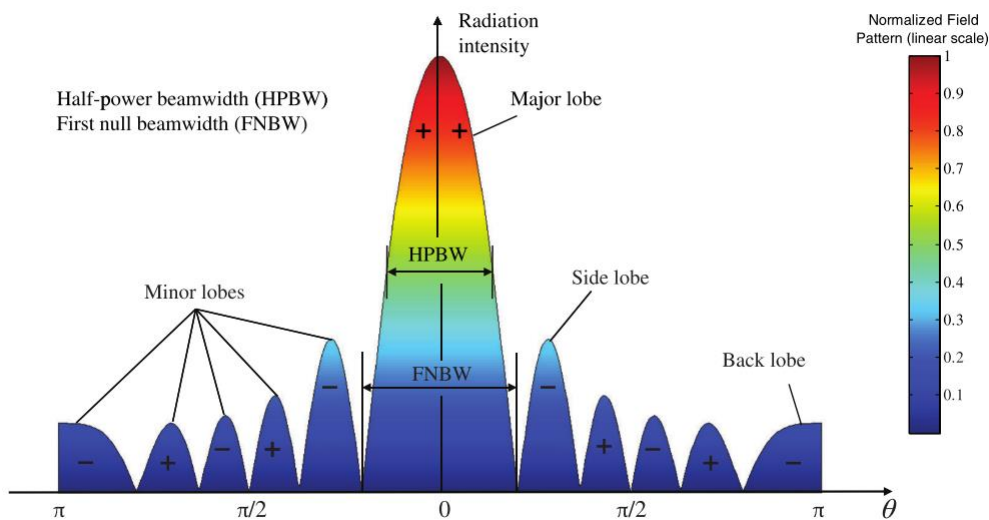


**Fig. 2.1:** Linear plot of the power pattern, showing its associated lobes and beamwidths **[14]**.

When it comes to radiation patterns directionally, they come in two types:

- Isotropic antenna: classified as a hypothetical lossless antenna having equal radiation in all directions and it is used as a reference for expressing the directive properties of an actual antenna.
- Directional antenna: defined as having the property of transmitting/receiving electromagnetic waves more efficiently only in certain directions.

In the case of a linearly polarized antenna, its performance is usually represented in terms of the E-plane and H-plane patterns.

- E-plane: defined as the plane containing the electric-field vector and the direction of maximum radiation.
- H-plane: defined as the plane containing the magnetic-field vector and the direction of maximum radiation.

## 2.2.2. Field Regions

The field around the antenna can be sub-divided into three regions (see Fig. 2.2):

- Reactive near-field: the portion of the near-field surrounding the antenna within the reactive field. This region as a maximum reach of: $R < 0.62\sqrt{D^3/\lambda}$ until its outer boundary, where $D$ is the largest dimension of the antenna, $R$ the radius of a field region and $\lambda$ is the wavelength.

- Radiating near-field (Fresnel): region located between the reactive near-field and the far-field. Within this region, radiation fields predominate and angular field distribution varies upon the distance from the antenna. This region is located between the outer boundary of the reactive–near field and reaches until a maximum of: $R < 2D^2/\lambda$, based on the criterion of the maximum phase error of $\pi/8$ .

- Far-field (Fraunhofer): region of the field of an antenna where the angular field distribution does not depend of the distance from the antenna. This region exists at ranges greater than the outer boundary of the radiating near-field: $R \geq 2D^2/\lambda$ .
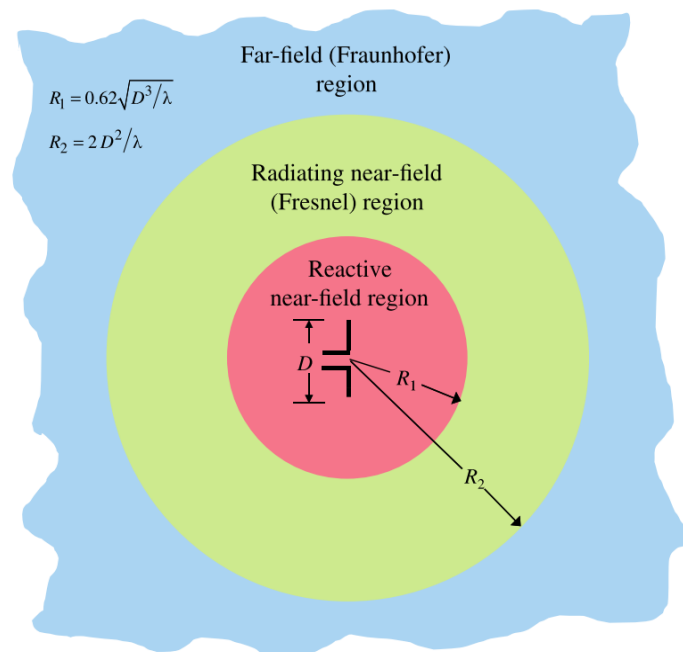
## 2.2.3. Radiation Power Density

Power density (average) $W_{av}$ is defined as the power density of the electromagnetic fields radiated by the antenna. Power density is complex, having a real component: $W_{RE}$, which is dominant in far-field region, and it has an imaginary component $W_{IM}$, which is dominant in the reactive near-field region, as shown in the following equation:

$$W = W_{RE} + jW_{IM} \qquad (W/m^2) \tag{2.1}$$

The power density associated with the electromagnetic fields of an antenna in the far-field region is referred as radiation density. The average power density is given by:

$$W_{av}(x,y,z) = \tfrac{1}{2} Re[\vec{E} \times \vec{H}^*] \qquad (W/m^2) \tag{2.2}$$

where $\vec{E}$ is the complex electric field, $\vec{H}$ is the complex magnetic field and *Re* stands for the real part.

The total power radiated by an antenna is:

$$P_{rad} = P_{av} = \oiint_S \vec{W}_{av} \cdot d\vec{S} = \oiint_S \vec{W}_{rad} \cdot \hat{n}\, da = \int_0^{2\pi} \int_0^{\pi} [\hat{a}_r\, W_0(r)] \cdot [\hat{a}_r\, r^2\, \sin\theta\; d\theta\; d\phi] \tag{2.3}$$

where $\hat{a}_r$ is the radial unit vector, $\hat{n}$ is the unit vector normal to the surface, $r$ is the sphere radius (closed surface), $da$ is the infinitesimal area of the closed surface ($m^2$) and $dS$ is the infinitesimal element of area of the surface.

## 2.2.4. Radiation Intensity

Radiation intensity (*U*) is known as the power radiated from an antenna per unit of solid angle (steradian), and it is usually determined in the far-field region.

$$U = r^2\, W_{rad} \qquad (W/sr) \tag{2.4}$$

where $W_{rad}$ is the radiation density, *r* the sphere radius and *sr* is a steradian.

The following equation shows the total power radiated, which is obtained by integrating the radiation intensity over the entire solid angle of $4\pi$:

$$P_{rad} = \oiint_S U \, d\Omega = \int_0^{2\pi} \int_0^{\pi} U \sin\theta \, d\theta \, d\phi \tag{2.5}$$

where $d\Omega$ is the element of solid angle.

## 2.2.5. Directivity

Directivity is defined as the ratio of the radiation intensity in a given direction from the antenna to the radiation intensity averaged over all directions. The averaged radiation intensity is equal to the total power radiated by the antenna divided by $4\pi$. So the directivity can be written as:

$$D_{dir} = \frac{U(\theta,\phi)}{U_0} = \frac{4\pi \, U(\theta,\phi)}{P_{rad}} \tag{2.6}$$

where $U_0$ is the radiation intensity of an isotropic source.

If the direction is not specified, it implies the direction of maximum radiation intensity (maximum directivity), the previous equation is also used, but replacing $U(\theta,\phi)$ by $U_m(\theta,\phi)$.

## 2.2.6. Input impedance

The input impedance is defined as the impedance presented by the antenna at its terminals, and it is expressed at the terminals as the ratio of the voltage to current or the ratio of the appropriate components of the electric to magnetic fields.
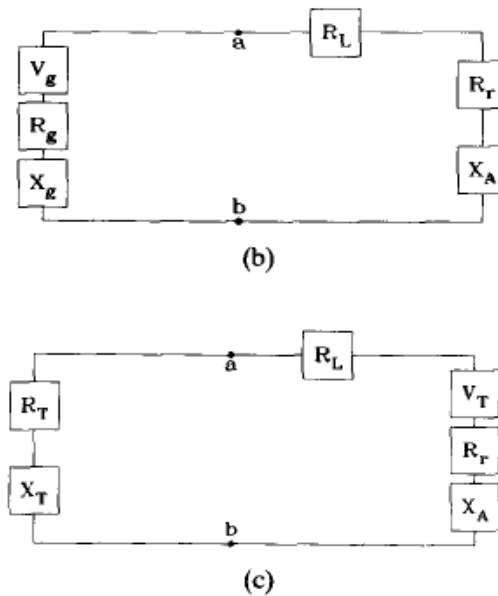


**Fig. 2.3:** Thevenin equivalent: transmitting (b) and receiving (c). **[13]**

In the previous figure (Fig. 2.3), the Thevenin equivalent of the antenna in the transmitting and receiving modes are shown. The resistance $R_r$ is referred to as the radiation resistance, and it is this resistance that represents antenna radiation or scattering. The conductive and dielectric losses of the antenna are accounted by $R_L$ and $X_A$ represents the imaginary part of the antenna impedance. The impedance of the generator and receiver (load) are represented, respectively, by $Z_g = R_g + jX_g$ and $Z_T = R_T + jX_T$.

## 2.2.7. Antenna efficiency and Radiation efficiency

The total efficiency $e_0$ takes into consideration losses at the input terminals of the antenna, as well as within its structure. Those losses could be because of:

- Reflections due to mismatch between the transmission line and antenna structure.
- Power losses due to conduction phenomenon's and in the dielectric.

Overall efficiency is represented as:

$$e_0 = e_r \, e_{cd} \tag{2.7}$$

where $e_r$ is the reflection (mismatch) efficiency, $e_{cd}$ is the conduction-dielectric efficiency.

The voltage reflection coefficient $\Gamma$ at the antenna input terminals is given by:

$$\Gamma = \frac{Z_{in} - Z_0}{Z_{in} + Z_0} \tag{2.8}$$

where $Z_{in}$ is the input impedance and $Z_0$ is the characteristic impedance.

The voltage standing wave ratio (*VSWR*) is given by:

$$VSWR = \frac{1 + |\Gamma|}{1 - |\Gamma|} \tag{2.9}$$

The total/overall efficiency can be rewritten as:

$$e_0 = e_{cd} \, e_r = e_{cd}(1 - |\Gamma|^2) \tag{2.10}$$

## 2.2.8. Gain

The gain of an antenna is defined as the ratio of the intensity, in a given direction, to the radiation intensity that would be obtained if the power accepted by the antenna (input power) was radiated isotropically. The gain (G) is a measure that takes into account the efficiency and the directivity of the antenna and it is represented by the following expression:

$$G = 4\pi \frac{U(\theta,\phi)}{P_{in}} \quad \text{(dimensionless)} \tag{2.11}$$

Just like the directivity, when the direction is not stated, the power gain is taken of maximum radiation.

The total radiated power ($P_{rad}$) is related to the total input power ($P_{in}$), and it can be written as:

$$P_{rad} = e_{cd} \, P_{in} \tag{2.12}$$

Considering the inclusion of reflection/mismatch losses (due to the connection of the antenna element to the transmission line: $e = e_0$), the gain equation is given by:

$$G(\theta,\phi) = e_0 \left[ 4\pi \frac{U(\theta,\phi)}{P_{rad}} \right] = e_{cd} \, e_r \, D_{dir}(\theta,\phi) = e_{cd}(1 - |\Gamma|^2) \, D_{dir}(\theta,\phi) \tag{2.13}$$

If the antenna is matched to the transmission line, which means, the antenna input impedance $Z_{in}$ is equal to the characteristic impedance $Z_0$ of the line, then the reflection coefficient $|\Gamma|$ is null.

## 2.2.9. Bandwidth

The bandwidth of an antenna is defined as the range of frequencies within which the performance of the antenna, with respect to some characteristics, conforms to a specific standard, usually within acceptable values of those at the centre frequency.

For narrowband antennas, the bandwidth is defined as a percentage of the frequency difference between upper and lower frequencies, over the central frequency. Such percentage indicates the frequency range of acceptable operation:

$$\frac{upper\ frequency - lower\ frequency}{central\ frequency} (\%) \tag{2.14}$$

## 2.2.10. Friis Transmission Equation

The Friis Transmission Equation correlates the power transmitted ($P_t$) from one antenna (the input power) to the power received ($P_r$) by another antenna (the power delivered to the load) within the far-field region, shown in Fig. 2.4, which includes the reflection, polarization and free space losses (losses due to spherical spreading of the radiated energy), is given by the following equation:

$$\frac{P_r}{P_t} = \left(\frac{\lambda}{4\pi d}\right)^2 D_t(\theta_t, \phi_t)\, e_{cdt}\, D_r(\theta_r, \phi_r)\, e_{cdr}\, (1 - |\Gamma_t|^2)(1 - |\Gamma_r|^2)\, |\hat{\rho}_t \cdot \hat{\rho}_r|^2 \qquad (2.15)$$

where $d$ is the separation distance between two antennas, $e_{cdt}/e_{cdr}$ is the transmitting/receiving antenna efficiency, $D_t(\theta_t, \phi_t)/D_r(\theta_r, \phi_r)$ is the transmitting/receiving directivity in the direction $\theta_{t/r}, \phi_{t/r}$, $\Gamma_t/\Gamma_r$ is the transmitting/receiving antennas reflection coefficient and $\hat{\rho}_t/\hat{\rho}_r$ is the unit vector of the transmitting/receiving wave.
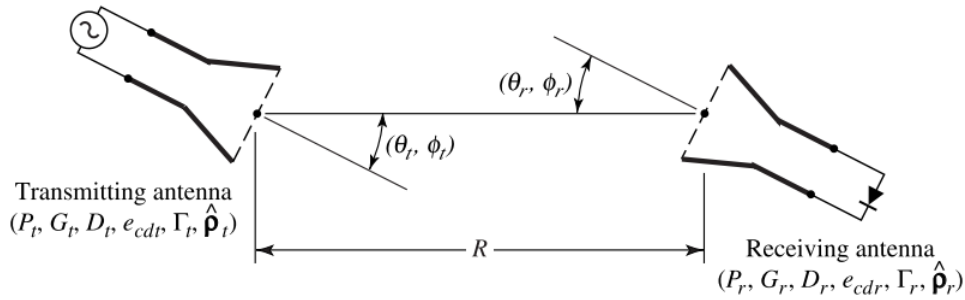


**Fig. 2.4:** Geometrical orientation of TX and RX antennas (Friis Equation) **[14]**.

The Friis equation is generally used when performing antenna gain measurements in an anechoic chamber environment. Hence it more convenient to have a direct relation between the Friis formula and the measured transmission coefficient, in dB:

Given that:

$$S21^2 = {P_r}/{P_t} \qquad (2.16)$$

So the Friis formula can be written as such (expressed in dB):

$$S21_{dB} = P_{L\,dB} + G_{t\,dB} + G_{r\,dB} \qquad (2.17)$$

where $G_t$ is the gain of the transmitting antenna and $G_r$ is the gain of the receiving antenna.

The Path Loss (in dB) is given by:

$$P_{L_{dB}} = 20\,Log\,\left(\frac{\lambda_0}{4\pi d}\right) \tag{2.18}$$

where $\lambda_0$ is the wavelength at the centre frequency and $d$ is the distance between the source antenna and the AUT [15]. It is required that the AUT is in the far field region in relation to the source antenna.

Regarding the gain measurement, there are essentially two basic methods that can be applied: the Absolute Gain method and the Gain Comparison method.

The Absolute Gain method doesn't need prior knowledge of the transmitting and receiving antenna gains. Within this method, there are two forms of determining the gain of the AUT. The first one is if both transmitting and receiving antennas are identical, or near copies, than one measurement will be enough to suffice the gain calculation. Another way, in case of both antennas being different from each other, than three antennas and three measurements will be required to assemble a set of three equations with three unknown variables in order to calculate the AUT gain.

The Gain Comparison method, a pre-calibrated source antenna (Standard Gain Antenna) is used to obtain the absolute gain of the antenna [16].

## 2.3. Arrays of Discrete Elements: Linear and Planar

Another approach to augment the overall physical size of an antenna and therefore to increase directivity (and gain) is to form an assembly of multiple elements of antennas called an array. The total field of the array is determined by the vector addition of the fields radiated by the individual elements, assuming that the current in each element is the same as that of the isolated element, meaning that coupling is neglected.

The array factor is a function of the geometry of the array and the excitation phase. By varying the separation $d$ and/or the phase $\beta$ between the elements, the characteristics of the array factor can be manipulated. Each array has its own array factor, and in general, it is a function of the number of elements and their spacing, geometrical arrangement and relative magnitudes/phases.

### 2.3.1. N-Element Linear Array: Uniform Amplitude and Spacing

An array, in this case of N elements, of identical elements and magnitudes, and each with a progressive phase is known as a uniform array.

The array factor, in normalized form, is given by:

$$(AF)_n = \frac{1}{N}\left[\frac{\sin\left(\frac{N}{2}\psi\right)}{\sin\left(\frac{1}{2}\psi\right)}\right], \; where \; \psi = kd\cos\theta + \beta|_{\theta=\theta_0} \; and \; k = 2\pi/\lambda \tag{2.19}$$

where $\theta_0$ is the angle of observation of interest.

To determine the nulls of the array, the previous equation is set to zero:

$$\sin\left(\frac{N}{2}\psi\right) = 0 \rightarrow \frac{N}{2}\psi|_{\theta=\theta_n} = \pm n\pi \rightarrow \theta_n = \cos^{-1}\left[\frac{\lambda}{2\pi d}\left(-\beta \pm \frac{2n}{N}\pi\right)\right]$$

$$, n = 1,2,3, \dots$$

$$, n \neq N, 2N, 3N, \dots \quad (2.20)$$

where $\theta_n$ is the null angle of observation.

The maximum values are determined from:

$$\frac{\psi}{2} \rightarrow \frac{1}{2}(kd\cos\theta + \beta)|_{\theta=\theta_m} = \pm m\pi \rightarrow \theta_m =$$

$$= \cos^{-1}\left(\frac{\lambda}{2\pi d}(-\beta \pm 2m\pi)\right), m = 0,1,2, \dots \quad (2.21)$$

The 3-dB point for an A.F. is:

$$\frac{N}{2}\psi \rightarrow \frac{N}{2}(kd\cos\theta + \beta)|_{\theta=\theta_h} = \pm 1.391 \rightarrow \theta_h = \cos^{-1}\left(\frac{\lambda}{2\pi d}\left(-\beta \pm \frac{2.782}{N}\right)\right) \quad (2.22)$$

where $\theta_h$ is the half-power point angle of observation and $f(x) = \frac{\sin x}{x} = 0.707 \rightarrow x = 1.391$.

## 2.3.2. Broadside Array

A broadside array is a type of array where the maximum radiation of an array directed normal to the axis of the array. For optimum performance, the maximum direction of the single element and of the array factor should both be directed toward $\theta_0 = 90^o$, where an example can be seen in Fig. 2.5. In order to an array to properly radiate broadside, the antenna element can be manipulated regarding its physical shape and dimensions, meanwhile the array factor can be altered by adjusting the separation and excitation of the individual antenna elements.

The first maximum of the array factor occurs when:

$$\varphi = kd\cos(\theta_0) + \beta = 0 \quad (2.23)$$

As it is desired a maximum at $\theta_0=90^o$:

$$\varphi = kd\cos(\theta_0) + \beta \xrightarrow{\theta=90^o} \beta = 0 \quad (2.24)$$

So have the maximum of the array factor of a uniform linear array (same amplitude excitation) directed broadside to the axis of the array, all the elements need have the same phase excitation.
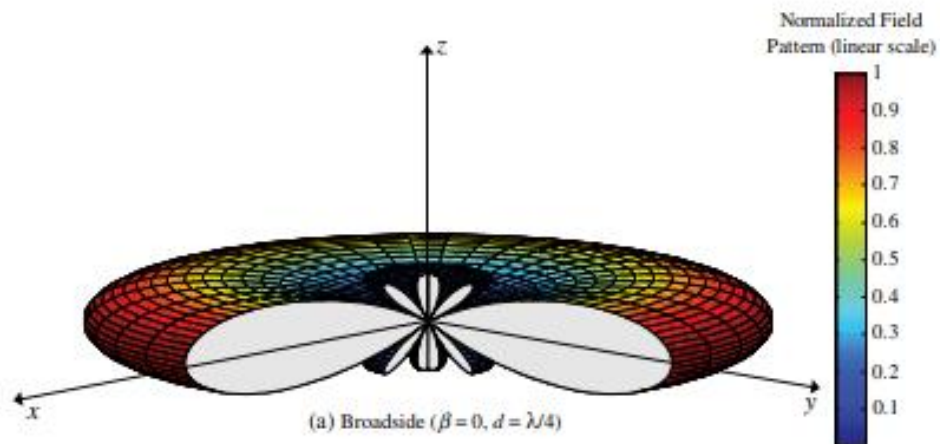


**Fig. 2.5:** Example of a three-dimensional amplitude pattern for a broadside array with N = 10 elements **[14]**.

The separation between the elements can be of any value, although to make sure that there aren't any other main lobes (maxima), also known as grating lobes, the separation between the elements should not be equal to multiples of a wavelength (d ≠ nλ, for n = 1, 2, 3...) when $\beta$ = 0. Hence, to avoid any grating lobes, the largest spacing between the elements for a broadside array should be less than one wavelength: $d_{máx.}$<λ **[14]**.

## 2.3.3. Planar Array

In comparison with linear arrays, planar (rectangular grid) arrays provide additional variables which can be used to manipulate the beam pattern of the array.

Both linear and planar geometries are shown in Fig. 2.6:
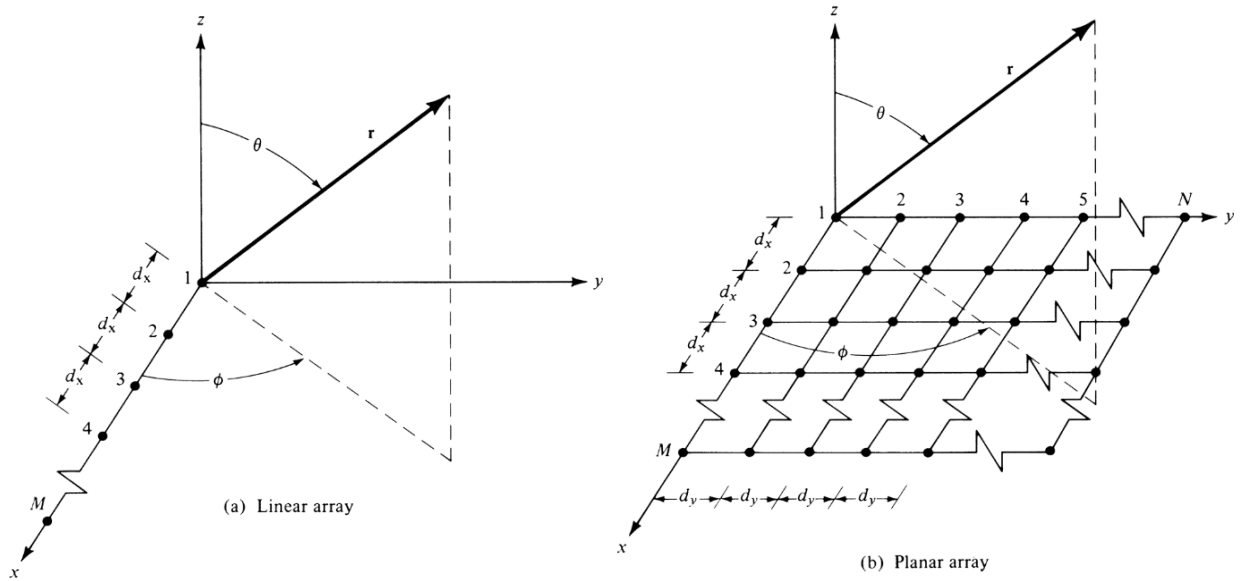
**Fig. 2.6:** Linear (a) and planar (b) geometries **[14]**.

The normalized array factor of a planar array is given by:

$$AF_n(\theta, \phi) = \left\{ \frac{1}{M} \frac{\sin\left(\frac{M}{2}\psi_x\right)}{\sin\left(\frac{\psi_x}{2}\right)} \right\} \left\{ \frac{1}{N} \frac{\sin\left(\frac{N}{2}\psi_y\right)}{\sin\left(\frac{\psi_y}{2}\right)} \right\}, \quad where \quad \psi_x = kd_x \sin\theta \cos\phi + \beta_x$$

$$\psi_y = kd_y \sin\theta \cos\phi + \beta_y \quad (2.25)$$

In order to avoid the formation of grating lobes, which are other maxima other than the major/main lobe, the spacing between elements (same principles as for a linear array) must not be sufficient large to allow in-phase addition of radiated fields in more than one direction. So, to avoid grating lobes in the x-z and y-z planes, the spacing between elements must not be equal or exceed $\lambda_0/2$ . True grating lobes occur if both the following equations lead to the same $\theta$ value:

$$\theta = \sin^{-1}\left[\frac{\sin\theta_0 \, \cos\theta_0 \pm m\lambda/d_x}{\cos\phi}\right] = \sin^{-1}\left[\frac{\sin\theta_0 \, \sin\theta_0 \pm n\lambda/d_y}{\sin\phi}\right] \qquad (2.26)$$

## 2.4. Patch Antennas

These type of antennas are known for their low-profile, compatible with planar/non-planar surface, simple and low-cost to manufacture using printed-circuit boards, and allow to manipulate in terms of resonant frequency, impedance, polarization and pattern, but possess major disadvantages such as low efficiency, low power, high quality factor, poor polarization purity and scan performance, spurious feed radiation and narrow frequency bandwidth.

One way to increase bandwidth and efficiency is to increase the height of the substrate, but as a result, surface waves are introduced and degrade the antenna pattern and polarization, and as such, some power is extracted from the total available power for direct radiation. However, some techniques are used to reduce such phenomenon like for example, the use of cavities.

There are many methods of analyses for microstrip antennas, three of the most used methods being: the transmission line model, the cavity model and the full-wave analysis [14].

## 2.4.1. Rectangular patch

The rectangular patch is one the most widely used microstrip antenna configuration, being it fairly easy to study using the transmission line and cavity models (good accuracy for thin substrates) [14].

A rectangular microstrip patch antenna can be represented by an equivalent circuit, which consists of as an array of two radiating narrow apertures (slots) (two parallel equivalent admittance $Y$, in parallel as well), with conductance $G$ and susceptance $B$, each of width $W$ and height $h$ (substrate height), separated by a distance $L$ (length of the patch) of low-impedance $Z_c$, as shown by the following figure (Fig. 2.7):



(a) Rectangular patch      (b) Transmission model equivalent
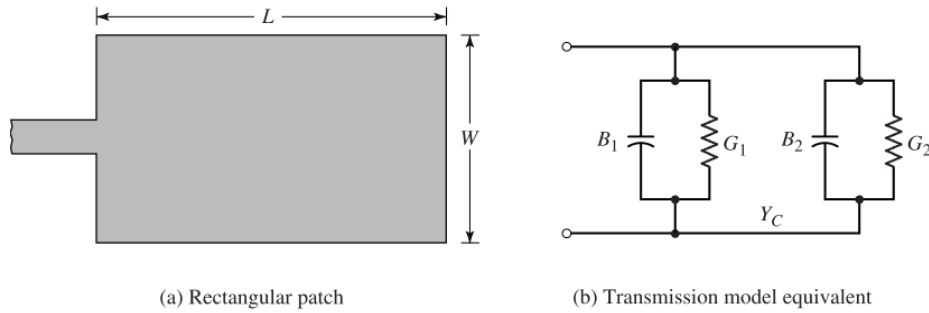
**Fig. 2.7:** Rectangular microstrip patch (a) and its equivalent circuit transmission line model (b) **[14]**.

where $Y_x = G_x + jB_x$ and $Z_x = 1/Y_x$ .

Due to the finite dimensions of the patch along the length and width, the fields at the edges of the patch undergo fringing, as seen in the Fig. 2.8 (the same is applied along the width).



(a) No Fringing      (b) Fringing
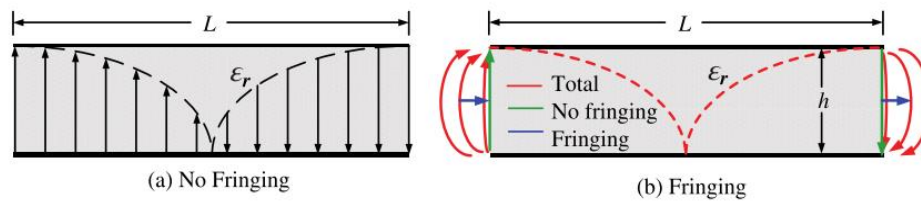
**Fig. 2.8:** Side view of microstrip antenna, without fringing (a) and with fringing (b) **[14]**.
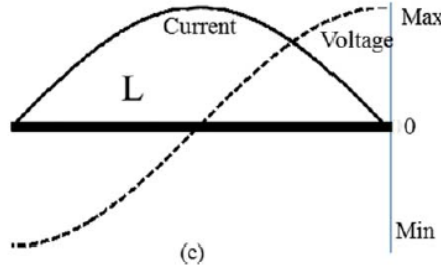
**Fig. 2.9:** Current and voltage waveforms along the antenna length (c) **[17]**.

The patch can be viewed as an open circuited transmission line ($|\Gamma| = 1$), and as such, as seen in Fig. 2.9, the voltage and current are out of phase. At the start and at the end of the patch, the current is null (open circuit), which its low value at the feed gives arise to a high impedance value. The current is at its maximum at the centre of the patch. Meanwhile, the voltage is minimum at the start of the patch, while it is maximum at the end **[18]**.

Due to the fringing effects, the electrical length of the patch will be greater than its physical length, hence a length compensation of $\Delta L$ is needed (on both sides), giving arise to the effective length of the patch:

$$L_{eff} = L + 2\Delta L \tag{2.27}$$

For the E-field in the XY-plane, fringing is a function of the ratio of the length of the patch ($L$) to the height ($h$) and the relative dielectric constant ($\varepsilon_r$) of the substrate. For microstrip antennas, where $L/h \gg 1$, the fringing effect is reduced, but it can cause a shift in the resonance frequency and with also $W/h \gg 1$, the electric field lines are concentrated mostly in the substrate. It's worth mentioning that higher order modes appear if the width is very wide **[9]**.

For the dominant $TM_{010}$ mode (first mode), the resonant frequency, which is the one most desired in almost all cases, of the microstrip antenna is a function of its length, and it is given by:

$$(f_r)_{010} = \frac{1}{2L\sqrt{\varepsilon_r}\sqrt{\mu_0\varepsilon_0}} = \frac{c}{2L\sqrt{\varepsilon_r}} \tag{2.28}$$

where $c$ is the speed of light in free space.

For a given $\varepsilon_r$ , $f_r$ and $h$, to design a rectangular patch, $W$ and $L$ can be determined:

$$W = \frac{c}{2f_r}\sqrt{\frac{2}{\varepsilon_r+1}} \tag{2.29}$$

For ($W/h > 1$), the effective dielectric length ($\varepsilon_{reff}$) is given by:

18

$$\varepsilon_{reff} = \frac{\varepsilon_r + 1}{2} + \frac{\frac{\varepsilon_r - 1}{2}}{\sqrt{\left[1 + 12\frac{h}{W}\right]}} \tag{2.30}$$

After obtaining $W$ and $\varepsilon_{reff}$, $\Delta L$ can be determined by the following equation:

$$\frac{\Delta \text{L}}{h} = 0.412 \frac{(\varepsilon_{reff} + 0.3)\left(\frac{W}{h} + 0.264\right)}{(\varepsilon_{reff} - 0.258)\left(\frac{W}{h} + 0.8\right)} \tag{2.31}$$

The above equations can be used to calculate the antenna dimensions given a desired resonant frequency and a specific substrate.

## 2.4.2. Quality factor, Bandwidth and Efficiency

Quality factor, bandwidth and efficiency are figures-of-merit, which are dependent of each other, and cannot be separately optimized, unfortunately requiring some sort of trade-off between them.

The quality factor represents the antenna losses from radiation ($Q_{rad}$), conduction ($Q_c$), dielectric ($Q_d$) and surface waves ($Q_{sw}$).

The total quality factor ($Q_t$) can be expressed as:

$$\frac{1}{Q_t} = \frac{1}{Q_{rad}} + \frac{1}{Q_c} + \frac{1}{Q_d} + \frac{1}{Q_{sw}} \tag{2.32}$$

Fractional bandwidth (*FW*) of an antenna is a measure of how wideband the antenna is. If the antenna operates with a centre frequency ($f_c$), between an upper ($f_{hi}$) and lower frequency ($f_{lo}$), then:

$$FW = \frac{f_{hi} - f_{lo}}{f_c} \tag{2.33}$$

Or it can be represented by the following equation, which takes into account the impedance matching, as long as, the range of frequency where the VSWR at the input terminals is less or equal to the desired maximum value and assuming VSWR near unity at the centre frequency:

$$FW = \frac{\Delta f}{f_0} = \frac{VSWR - 1}{Q_t \sqrt{VSWR}} \tag{2.34}$$

If the surface wave power is much smaller than the radiated power and $|\Gamma| \leq 1/3$, than an approximate equation for the bandwidth is given by [14]:

$$BW = \frac{16}{3\sqrt{2}}\left[\frac{\varepsilon_r - 1}{(\varepsilon_r)^2}\right]\frac{h}{\lambda_0}\left(\frac{W}{L}\right), \quad \text{only if} \quad h \ll \lambda_0 \tag{2.35}$$

As already known, the radiation efficiency is defined as the radiated power over the input power, but it can also be expressed in terms of the quality factors (for a microstrip antenna), as it follows:

$$e_{c,d,sw} = \frac{1/Q_{rad}}{1/Q_t} = \frac{Q_t}{Q_{rad}}$$ (2.36)

## 2.4.3. Coupling

Coupling (electromagnetic mutual effects) between two patches, apertures or wires is described as a function of the position of one element in relation to another, and is mainly attributed to the fields that exist along the air-dielectric interface.

When comparing the coupling effect between elements collinearly along the E-plane and elements collinearly along the H-plane, for an edge separation of $\Delta d$, the smallest coupling isolation for a very small spacing ($\Delta d < 0.1\,\lambda_0$) is observed for the E-plane, while for the H-plane, the smallest coupling isolation is seen for large spacing ($\Delta d > 0.1\,\lambda_0$). Meanwhile, the spacing for each coupling from one element overtakes another element also depends of the electrical e geometrical properties of the antenna.
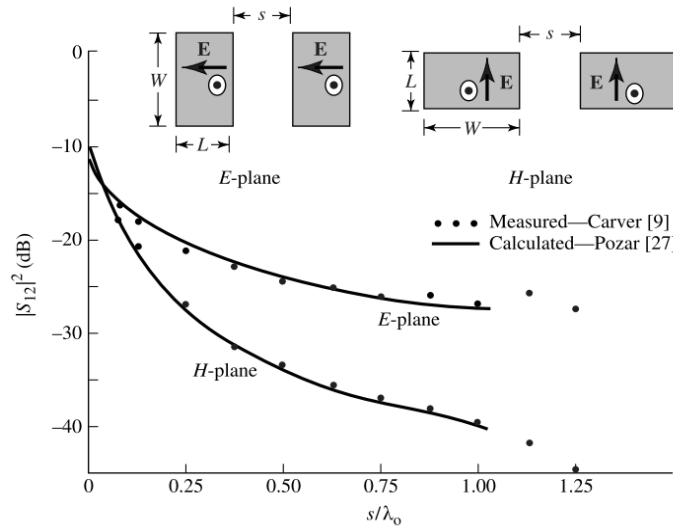


**Fig. 2.10:** Measured and calculated mutual coupling (E-plane and H-plane) between two coax-fed microstrip antennas **[14]**.

In the case of a rectangular patch, the EM fields are TM in a direction of propagation along the E-plane and TE in a direction of propagation along the H-plane. For the E-plane arrangement (seen in Fig. 2.10) there is a stronger surface wave excitation between the elements: the coupling is larger. However for the H-plane arrangement, there isn´t a strong dominant mode surface wave excitation, so there is less coupling between the elements.

However, if the thickness of the substrate increases, it allows higher order TE surface wave excitation.

Mutual coupling between elements can introduce scan blindness, which limits, for a maximum reflection coefficient, the angular volume over which the arrays can be scanned. Scan blindness is mostly influenced by surface waves within the substrate.

## 2.4.4. Feeding methods

Of all configurations that exist and can be used to feed signal to a microstrip antenna, four of the most famous ones include the microstrip line feed, the coaxial probe feed, aperture coupled feed and proximity coupled feed, which are shown in Fig. 2.11 and their equivalent circuit in Fig. 2.12.

Starting with the microstrip line feed, shown in Fig. 2.11 (a), it is the simplest one, just consisting of a microstrip line that feeds signal to the antenna (a conducting strip), being easy to manufacture and simple to match by adjusting the inset position. Since this technique takes advantage of the impedance variation with the length of the patch, so it is possible to obtain the desired input impedance by finding an optimal position for the feeding point. However, as the substrate thickness increases, surface waves and spurious feed radiation increase, limiting maximum bandwidth achievable.

Next up is the coaxial probe feeding method, illustrated in Fig. 2.11 (b), which consists of coaxial line, where the inner conductor of the cable is attached to the radiation patch while the outer conductor is connected to the ground plane of the antenna. Just like the microstrip feed, it is easy to fabricate and simple to match. Although this technique has low spurious radiation, it suffers from narrow bandwidth and parasitic inductance limitations, since the feed length varies as a function of the substrate thickness.

Both of the previous described contacting inset feeding methods possess inherent asymmetries which generate higher order modes, creating cross-polarized radiation.

In relation to the non-contacting feeding methods, the aperture coupling technique (Fig. 2.11 (c)) consists of two substrates separated by a ground plane. On the bottom side of the lower substrate, typically a high dielectric material, there is a microstrip feed line whose energy is coupled to the patch, which is on top of the upper substrate, typically a low dielectric material, through a slot on the ground plane separating the two substrates. The ground plane acts as an isolator between the feed and the patch, which reduces spurious radiation and polarization purity. This configuration allows independent optimization by adjusting the feedline length and the size and position of the slot. However, this technique has narrow bandwidth, it is the most difficult of the four methods to manufacture and generates moderate spurious radiation.

Lastly, the proximity coupled feed or the magnetic coupling feed (Fig. 2.11 (d)), consists of two substrate layers, with the microstrip line between both substrate layers and the patch on the top of the upper substrate. In order to manipulate the input impedance, the length of the feeding stub and the width-to-line ratio of the patch can be changed. Out of the four feeding methods, the proximity coupling provides the largest bandwidth and has low spurious radiation.



(a) Microstrip line feed

(b) Probe feed

(c) Aperture-coupled feed

(d) Proximity-coupled feed
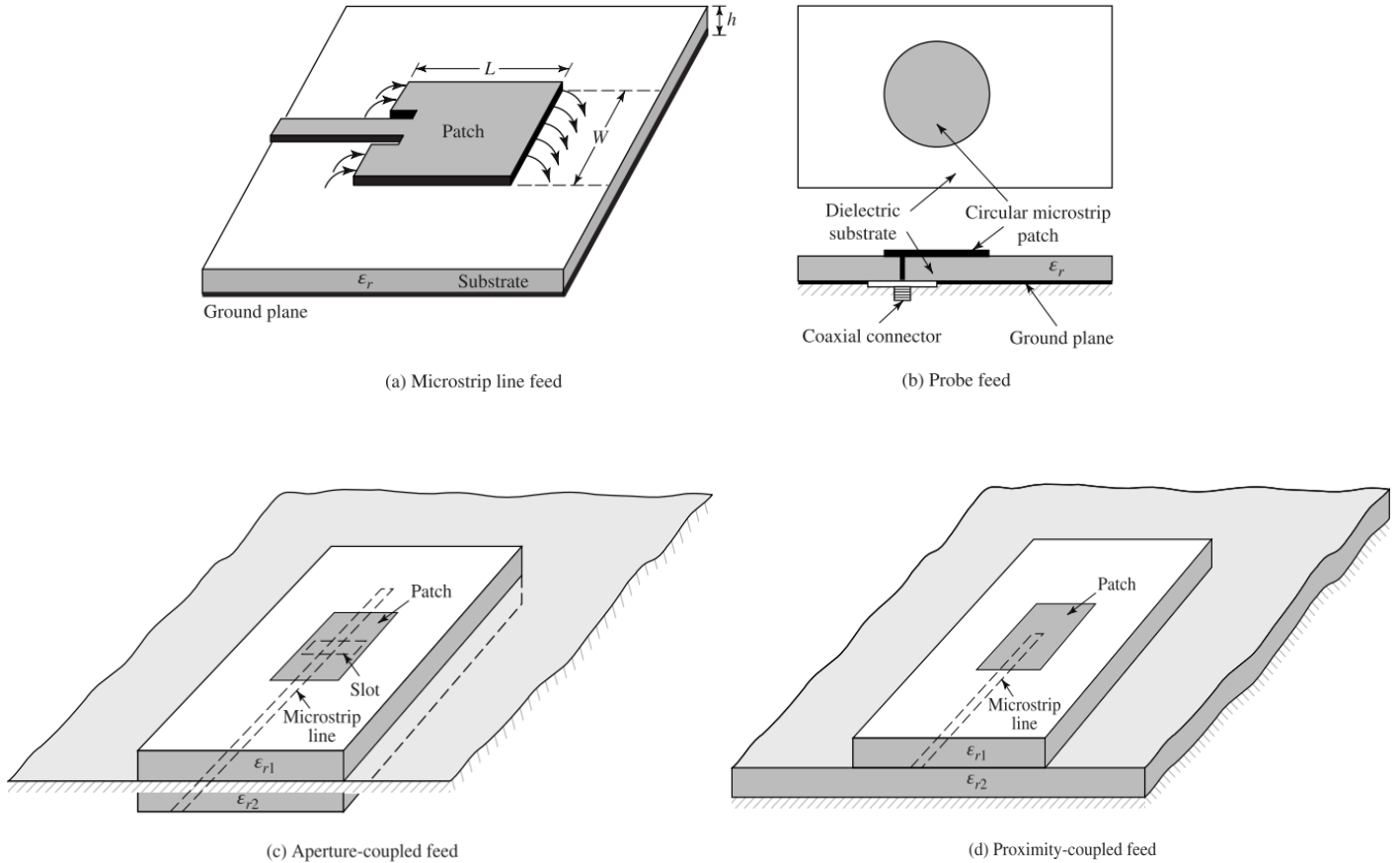
**Fig. 2.11**: Types of feeds for microstrip antennas: (a), (b) - contacting inset feeds and (c), (d) – non-contacting aperture-coupling feeds **[14]**.



(a) Microstrip line

(b) Probe

(c) Aperture-coupled

(d) Proximity-coupled
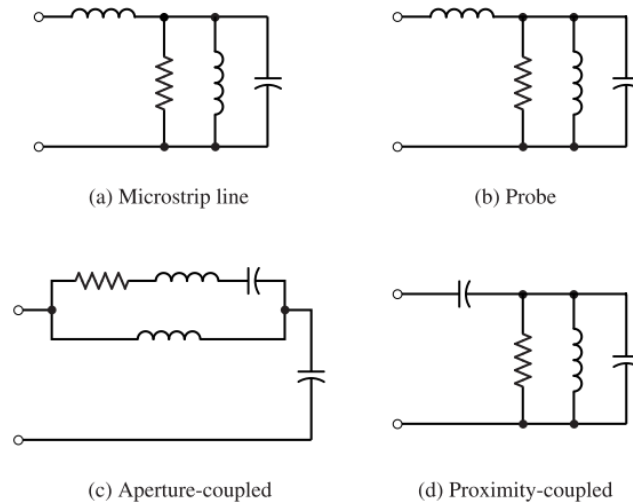
**Fig. 2.12:** Equivalent circuits of the types of feeds from Fig. 2.11 **[14]**.

## 2.5. Conclusions

In this chapter, important antenna figures-of-merit were presented and discussed, these being part of the very basic antenna theory necessary to proceed onward with the design and analysis of a single antenna element and an antenna array that were developed within this work.

# Chapter 3: Antenna Element Design

## 3.1. Introduction

Antenna designs targeting the sub-THz region generally involve complex manufacturing processes such as multi-layer configurations **[19]**. So in order to follow a more cost effective and less complex manufacture process, a single substrate layer configuration was approached. Given the advantages the coplanar waveguide have over microstrip configurations at high frequencies, such as low frequency dispersion, most noticeably for narrow width lines, lower crosstalk, higher isolation, and reduced radiation losses **[20]**, an antenna element fed by a CPW structure is proposed in order to evaluate its performance at an operation frequency of 100 GHz.

The need to meet design requirements, at higher frequencies, where radiation loss dominates, justifies the need for more expensive alternatives such as multi-layered substrate structures, complex feeding methods, or even the use of non-commercially available substrate materials. This antenna element explores the use of a single substrate layer through the application of uniplanar transmission lines such as CPW, to evaluate its performance, efficiency and feasibility in the sub-Terahertz range.

This chapter is structured in such that, following this introduction, the design of the components that form the antenna element are shown and explained, followed by the design process behind the TRL calibration kit. Lastly, a direct comparison between simulated and measured reflection coefficient and radiation pattern of the antenna element is performed, followed by a summary of the main observations and conclusion obtained from this chapter.

Throughout the dissertation, the simulator used was a commercial finite element method solver for electromagnetic structures named HFSS, from ANSYS.

## 3.2. Patch antenna design

### 3.2.1. Square Loop Feeding Method

The theoretical values that can be obtained from formulas in **[14]** and **[21]**, for the patch antenna and the quarter-wavelength transformer, and for both the CPW and GCPW transmission lines in **[22]**, is a starting point for the dimensions of all the components that form the antenna element. Since the actual process of optimization is done through simulations, parametric sweeps of each variable presented in Fig. 3.1 were performed. Given the implementation of a single substrate layer, and in order to obtain a high radiation efficiency and wide bandwidth **[23]**, a Rogers RT/duroid 5880, with a thickness of 0.127 mm and dielectric constant of 2.2 was used. A minimum substrate height of 0.127 mm was chosen as a starting value, to minimize the radiation losses from the feed line **[24]**.

For this design, three forms of antenna feeding were considered, taking advantage of the CPW feed line type, those being: inductive feed (CPW short-end structure) **[25] [26]**, capacitive feed (CPW open-end structure) and square loop feed **[27]**. All three of these feeding types were modelled and simulated, the latter being the only one that performed above the minimum requirements. The schematic of all three patch antenna CPW feeding configurations are shown in Fig. 3.1. When comparing the obtained simulated reflection coefficients, shown in Fig. 3.2, and the radiation patterns, depicted in Fig. 3.3, of all three mentioned antenna feed structures, the square loop feed structure presents a desirable minimum bandwidth of at least 5% fractional bandwidth, the trade-off being a lower front-to-back ratio. Regarding the results presented in Fig. 3.2 and Fig. 3.3, the solid red line represents the square loop feed, from Fig. 3.1 (c), the long dashed blue line represents the inductive feed structure, from Fig. 3.1 (a) and the short dashed green line represents the capacitive feed structure from Fig. 3.1 (b).

It is worth mentioning that it is important that the CPW feed is completely covered by the patch antenna, to maximize electromagnetic coupling efficiency **[25] [27]**. However, if the current value of the substrate height is not enough to provide the minimum required bandwidth, then the following available value of height of the Rogers RT/duroid 5880 series would need to be used (h=0.254 mm). The dimensions of the final design are given in Table 3.1.

(a)



(b)

(c)



(d)
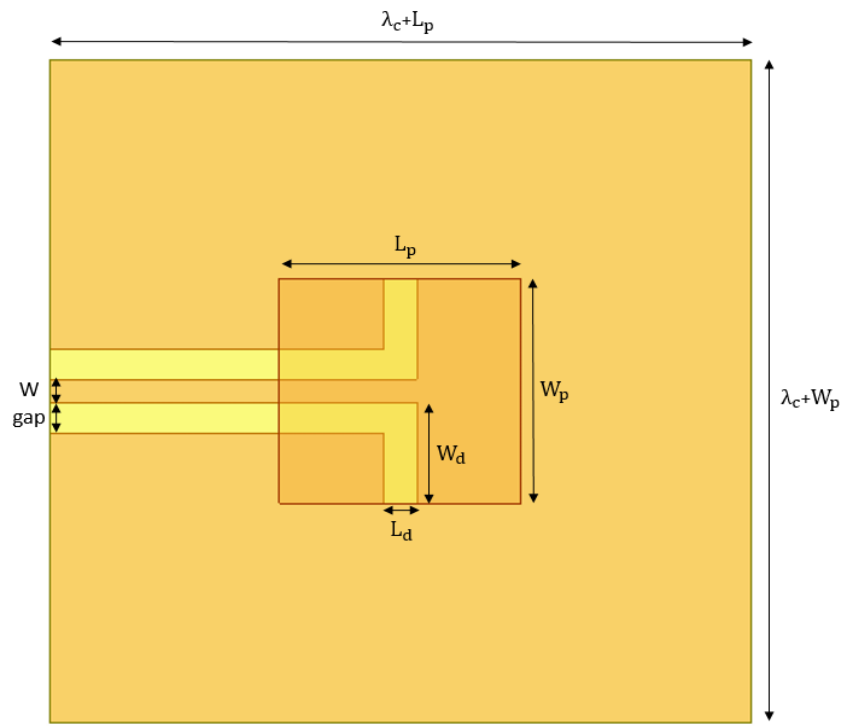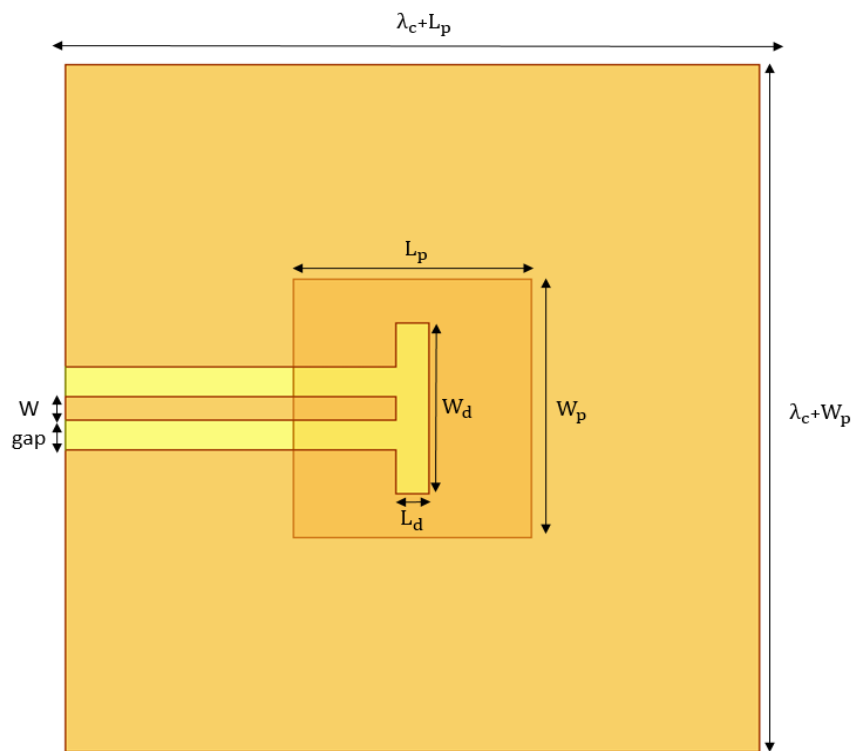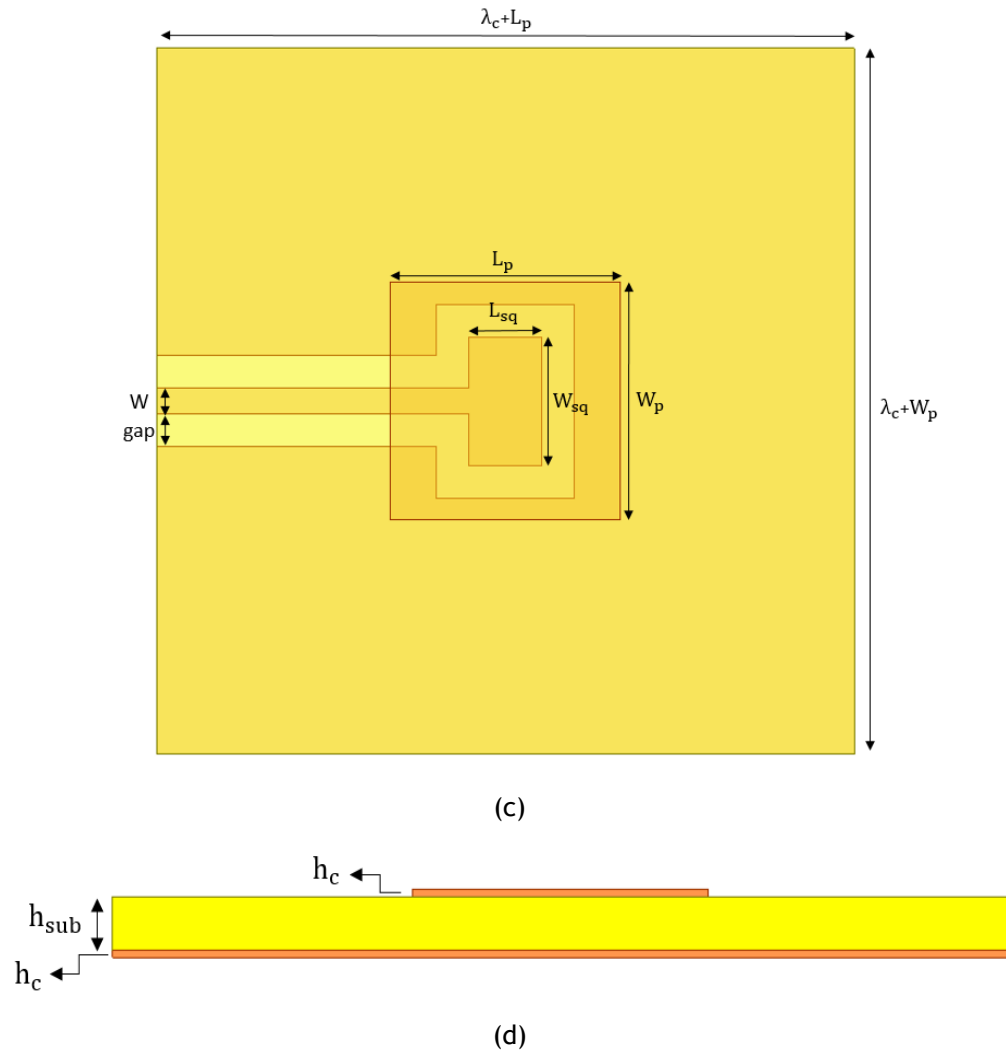
**Fig. 3.1.** Schematic of the patch antenna fed by a: inductively CPW feed (a), capacitive CPW feed (b), square loop CPW feed (c) and Z plane view common to all configurations (d).

**Table 3.1** — Variable values for the patch antenna and the square loop feed for Fig. 3.1 (c) and (d).

| Variable | Values (mm) |
|----------|-------------|
| W | 0.814 |
| gap | 0.105 |
| $W_{\mathrm{p}}$ | 0.76 |
| $L_{\mathrm{p}}$ | 0.742 |
| $W_{\mathrm{sq}}$ | 0.411 |
| $L_{\mathrm{sq}}$ | 0.235 |
| $\lambda_{\mathrm{c}}$ | 1.5 |
| $h_{\mathrm{sub}}$ | 0.127 |
| $h_{\mathrm{c}}$ | 0.018 |
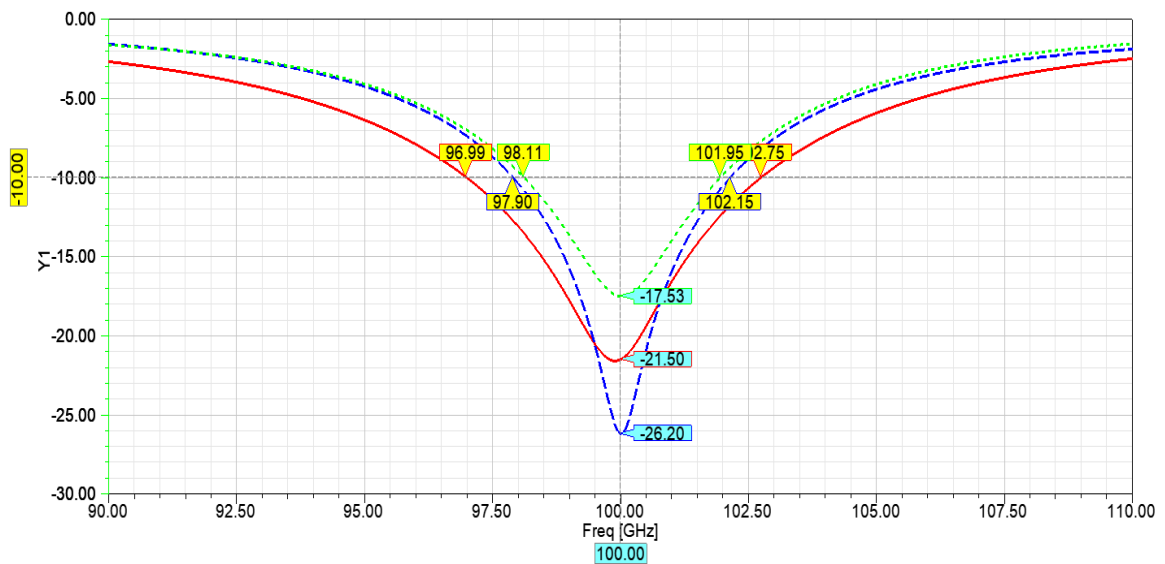


**Fig. 3.2.** S-parameters of all three antenna CPW configurations from Fig. 3.1.

| Name | Theta | Ang | Mag |
|---|---|---|---|
| Square Loop Feed | 0.0000 | 0.0000 | 7.1955 |
| Inductive Feed | 0.0000 | 0.0000 | 7.5599 |
| Capacitive Feed | 0.0000 | 0.0000 | 7.8315 |

**Fig. 3.3.** Simulated radiation patterns of all three antenna CPW configurations from Fig. 3.1, for the θ plane, at φ = 90°.

### 3.2.2. GCPW-CPW Feed Line Design

A description of the feed line, from the GCPW line where the connector is attached, to the CPW line that connects to the square loop feed is given. A schematic of the line, top and bottom views is shown in Fig. 3.4, along with the reference number of the different line sections.

The connector to be used for the measurement of the full antenna element is a 1.0 mm jack (female) end launch connector (DC up to 110 GHz), model 2492-04A-6, from Southwest Microwave, to be connected to a 50 Ω GCPW line (section 1 in Fig. 3.4). The lines represented in section 3 (GCPW) and 4 (CPW) are chosen to have an impedance of 90 Ω, due to their similarity in line width and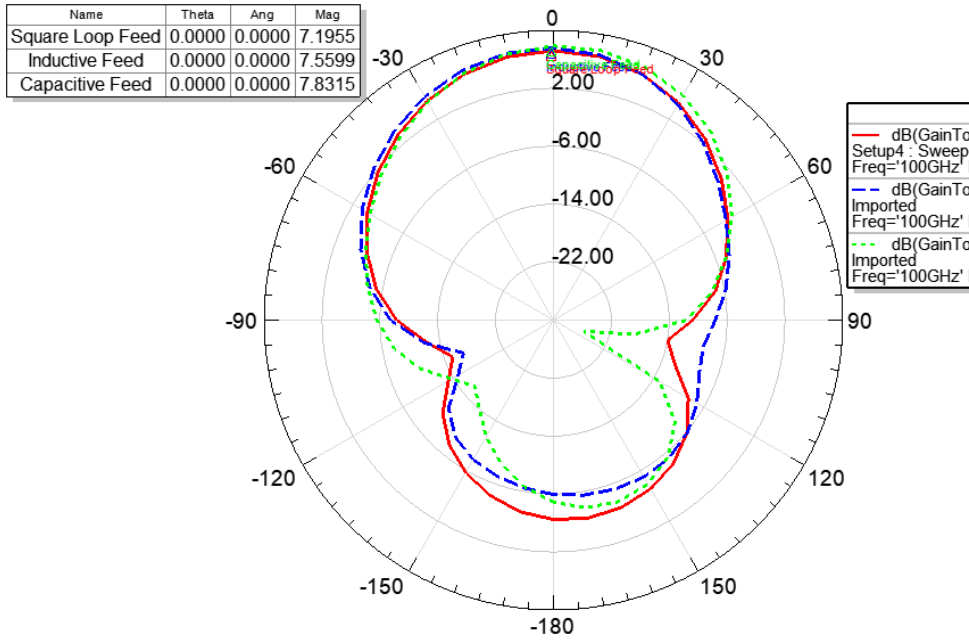 gap values. In section 2, a quarter-wavelength transformer was used to adapt de 50 Ω GCPW line to the 90 Ω GCPW line. The GCPW-CPW transition (section 3 to section 4) was implemented by a gradual tampering of the bottom ground plane of the GCPW side until it reached a width value limit, considering the manufacturing design constraints/limits. In section 5 of the feed line, another quarter-wavelength transformer, in the CPW side, was used to adapt the 90 Ω CPW line to the CPW line impedance leading into the square loop feed (112.6 Ω CPW line). The values of the impedance, line width and gap values of each section are presented in Table 3.2.

The simulated S-parameters of the entire GCPW-CPW feed structure, described previously, are shown in Fig. 3.5, for the frequency band of interest (from 90 GHz to 110 GHz).
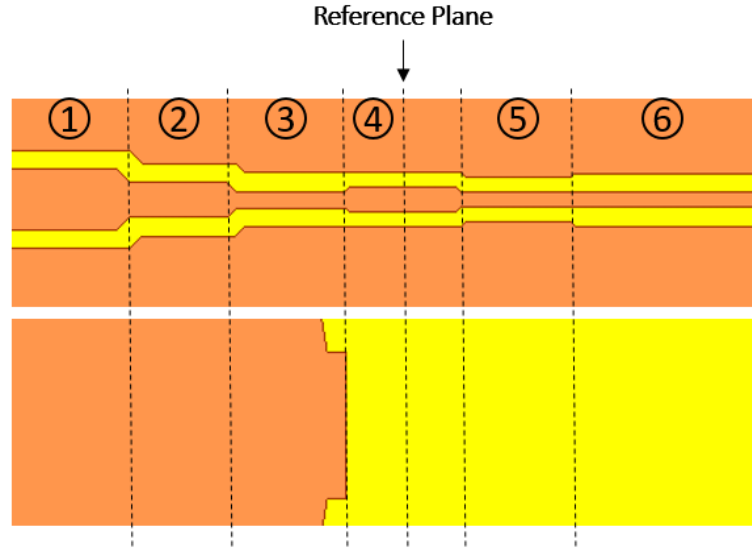
**Fig. 3.4.** Zoomed-in schematic of GCPW-CPW feed line leading into the antenna feed structure (view of the line (above) and view of the ground plane (below)).

**Table 3.2** − Variable values for the various line sections of the GCPW-CPW feed line structure.

| Line Type | Line Section | Impedance Value (Ω) | Line Width (mm) | Line Gap (mm) |
|-----------|--------------|---------------------|-----------------|---------------|
| GCPW | 1 | 50 | 0.325 | 0.1 |
| GCPW | 2 | 67.08 | 0.185 | 0.1 |
| GCPW | 3 | 90 | 0.091 | 0.1 |
| CPW | 4 | 90 | 0.135 | 0.08 |
| CPW | 5 | 110.66 | 0.084 | 0.08 |
| CPW | 6 | 112.6 | 0.075 | 0.105 |
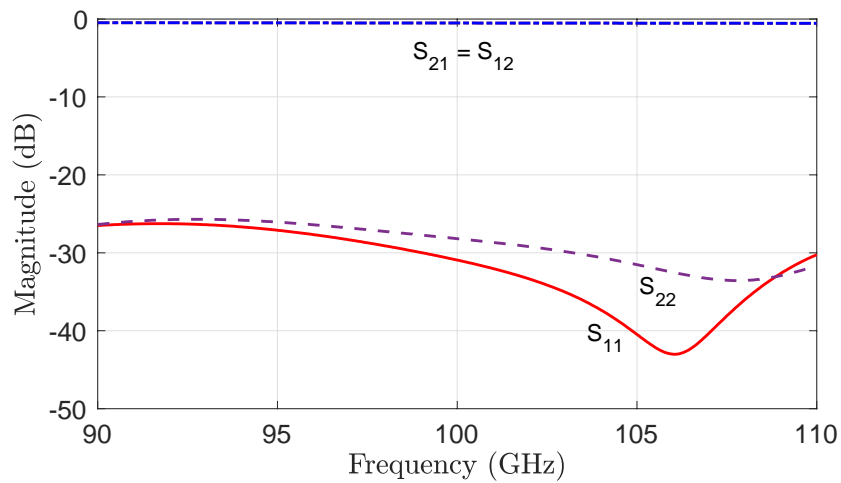


**Fig. 3.5.** S-parameters of GCPW-CPW feed line leading into the antenna feed structure.

Fig. 3.6 shows a schematic of the full antenna designed in HFSS, which includes an approximate model for the 1 mm end launch connector. Upon simulation it was observed, as seen in Fig. 3.7 (radiation pattern in dashed blue), that initially, without any line length extension, the radiation pattern showed considerable side lobes at the right side of the polar plot. In order to reduce said side lobes, the distance between the connector structure and the patch antenna, starting at a length value of 0 mm, was increased, by extending the 90 Ω CPW line length, by a length of 15 mm, obtaining the radiation pattern in orange. Note that not only the radiation pattern becomes more distorted, but also the antenna radiation efficiency decreases slightly (it decreased from 91% to 80%), as a result of increasing the line length, leading to a decision of not increasing it above 15 mm. This is considered as a trade-off point.



(a)



(b)



(c)

**Fig. 3.6**. Top (a), bottom (b) and side view (c) of the connector with the full antenna element HFSS model.

**Fig. 3.7.** Antenna radiation pattern for the θ plane at φ = 90° for the variation of the CPW 90 Ω line length – 0 mm and 15 mm, at 100 GHz.

## 3.3. TRL calibration kit design

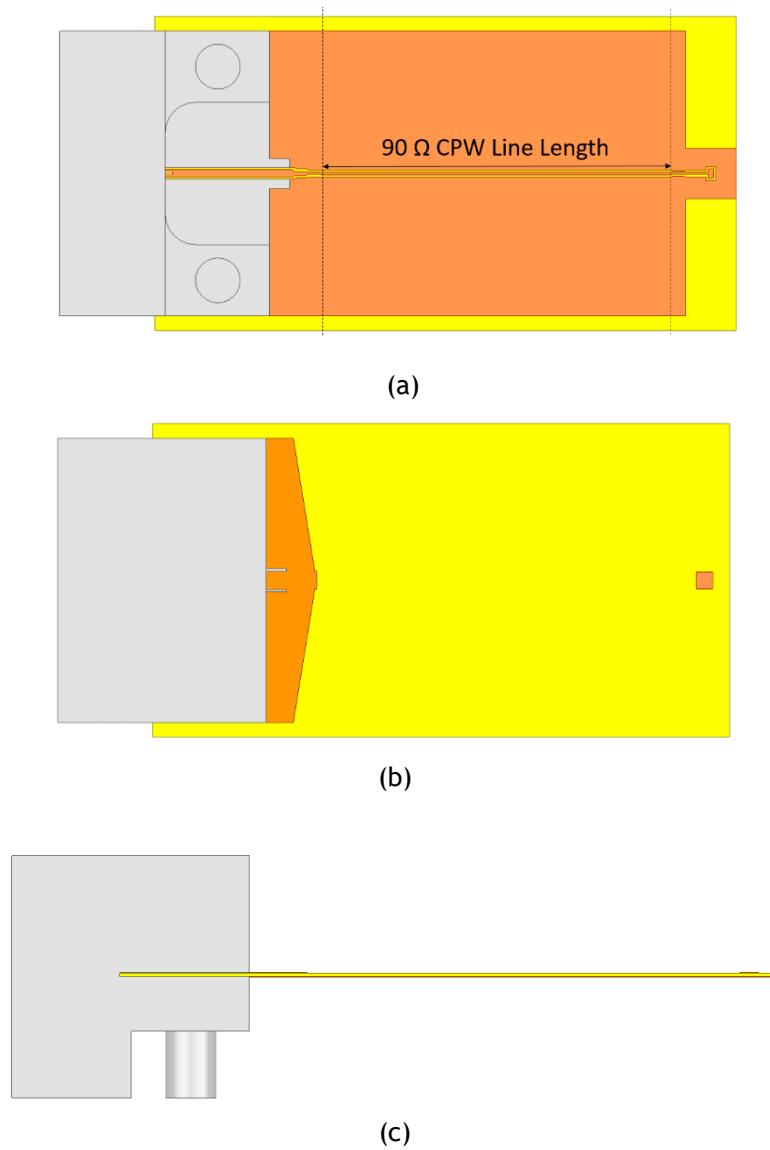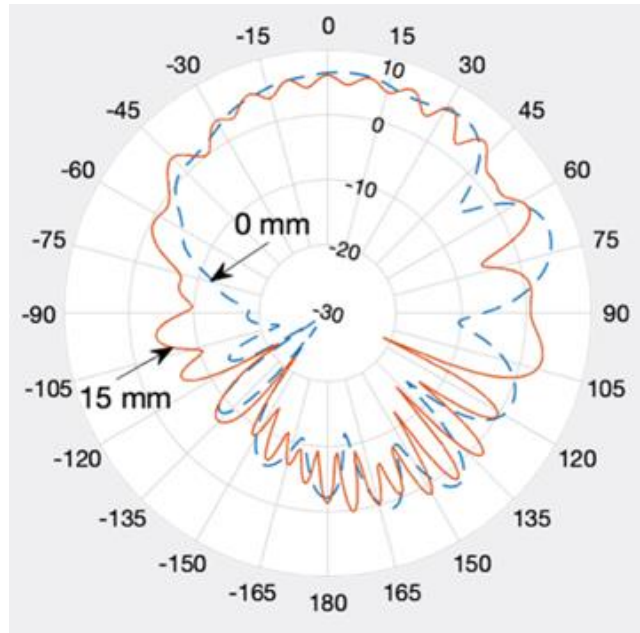In order to perform measurements, a calibration kit suitable for the antenna element was designed so that the latter can be accurately measured using a vector network analyser (VNA). A VNA is a precision measuring device that tests the electrical performance of components within the radio, microwave and millimetre frequency bands **[28]**.

Measurement errors in network analysis can be divided in systematic and random errors. Systematic errors are calibrated out of the measurement process with the use of a calibration kit to allow an accurate comparison between simulated and experimental results, regarding the reference plane, while random errors are defined as non-repeatable and unpredictable measurement variations **[29]**.

The SOLT calibration method provides a 12-term error model, through the measurement of a set of know standards, those being: Short, Open, Load and Through **[24]**.
The full two-port model includes all six terms: directivity, reflection tracking, load match, transmission tracking, source match and isolation for the forward and reverse direction, giving a total of twelve error terms **[28] [30]**.

As opposed to the SOLT calibration, which is not viable at high frequencies, due to parasitic capacitances on load resistors (load standard of the SOLT) **[31]**, a TRL (Through(Thru)-Reflect-Line) was designed, where for this type of calibration, only the line standard needs to be precisely known. A TRL kit is often used also to de-embed two-port data, using an eight-term error correction model, and it was developed to make accurate measurements of non-coaxial devices at millimetre waves **[32]**. The line standard, which is a portion of a transmission line between the reference ports of the Through Standard, is characterized by a line impedance,

offset delay and line loss, parameters that can be modified when configuring the calibration kit in a VNA device.

The offset delay value necessary for input in the VNA can be theoretically obtained using the following formula:

$$\text{offset delay} = \frac{l \times \sqrt{\varepsilon_r}}{c} \ (ps) \tag{3.1}$$

where $l$ is the physical offset length from the reference planes, $\varepsilon_r$ is the relative permittivity (dielectric constant) and $c$ is speed of light in vacuum.

The thru standard is a zero-length distance between the desired reference planes of each port.

For the reflect standard, the use of a short standard was preferred, due to the fact that open standards radiate more. The line standard is essentially the thru standard, but with an extra line length between both reference planes. In comparison with the thru standard, the transmission coefficient phase of the line standard should only vary between 20º and 160 º. As a rule of thumb, 90º is usually preferred (as it is the centre value) **[24]**. The effective length should never reach $0^o$ or $180^o$ for the frequency band of interest, although some margin is left regarding those two values, to account for problems such as line parasitics, spurious mode launches, amongst other problems, hence the rule of thumb previously mentioned **[33]**.

From the simulations results, the transmission coefficient phase difference between the through and line standard was set at $\Delta\varphi \approx 90.53°$, and as such, the offset delay of the 90º electrical length line portion was set at $\Delta t \approx 3.11$ ps, the latter needed for the VNA configuration of the TRL. In Fig. 3.8, the HFSS model of the TRL is shown, and in Fig. 3.9, the simulated results of the S-parameters for the three standards of the TRL are displayed.
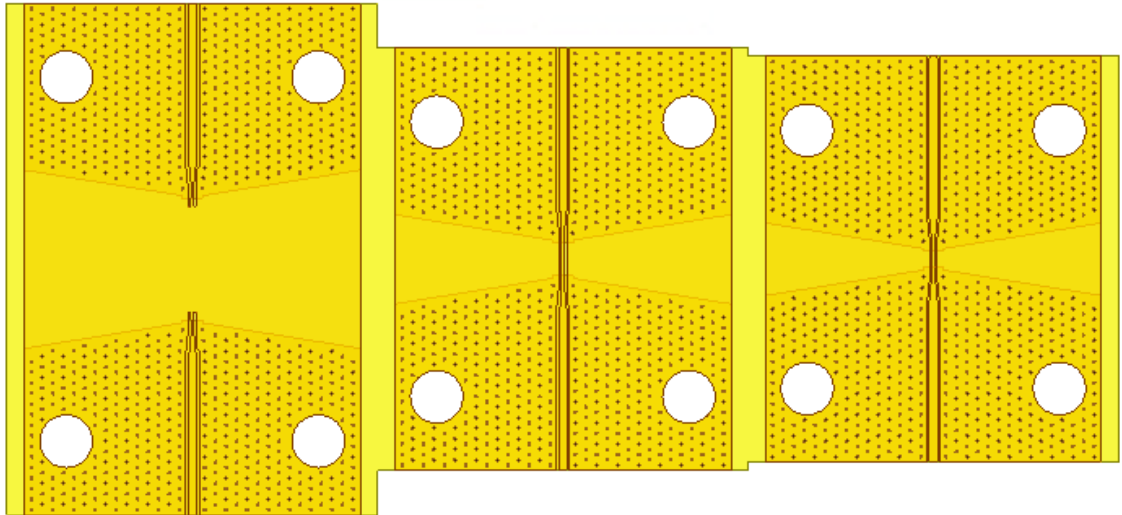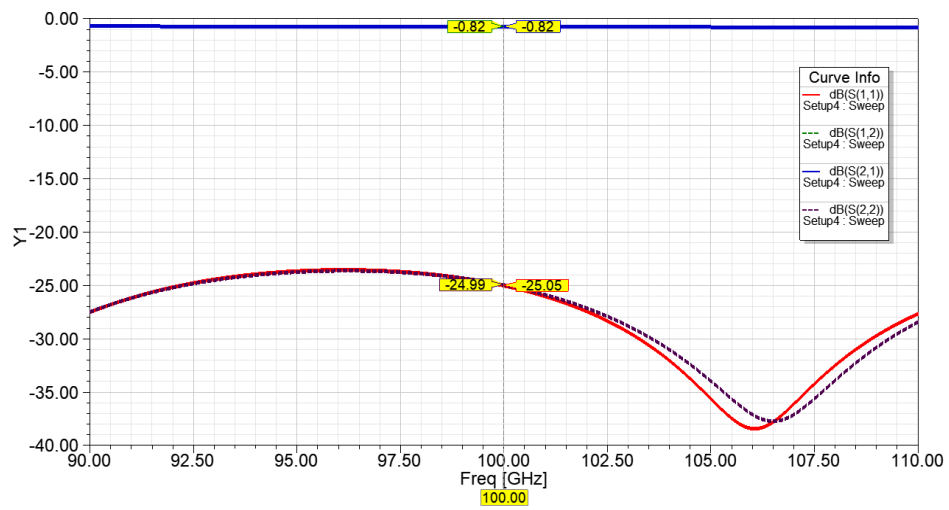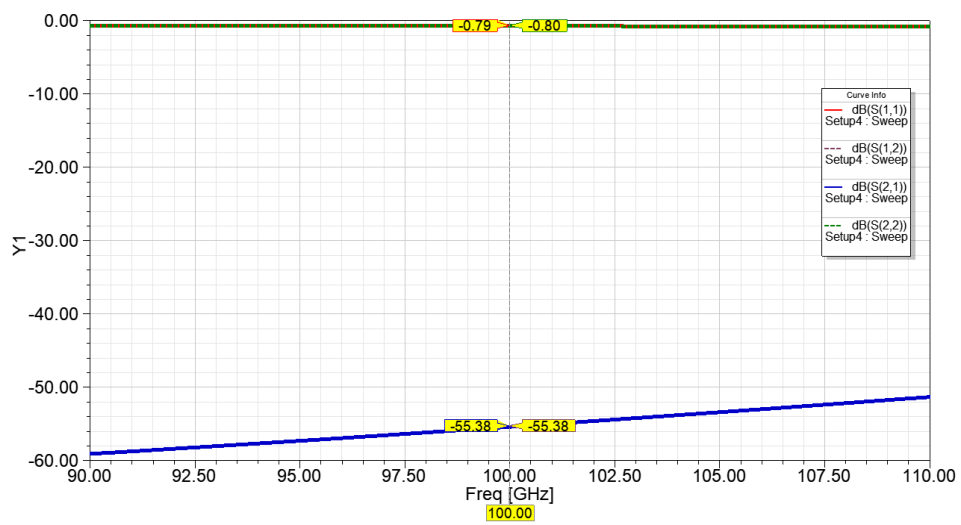
**Fig. 3.8.** HFSS models of the Through (a), Reflect (Short) (b) and Line (c) standards.



(a)



(b)

35

(c)
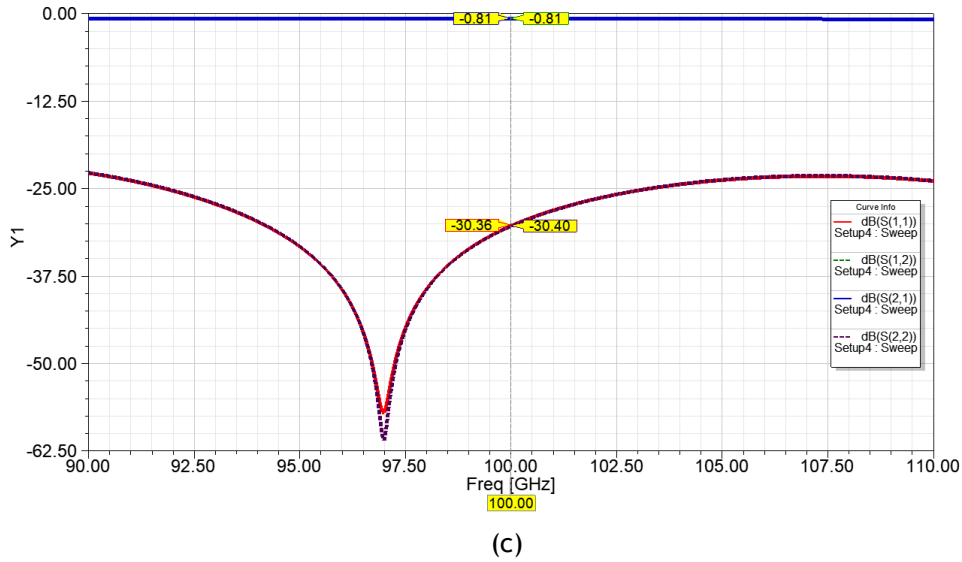
**Fig. 3.9.** Simulated S-parameters of the Through (a), Reflect (Short) (b) and Line (c) standards.

## 3.4. Simulation and Experimental Results Comparison

In this section, a comparison analysis of reflection coefficient and radiation pattern (θ plane, φ=90°) between simulated and measured results is presented. A picture of the fabricated antenna element and TRL calibration kit, with the connectors attached, is displayed in Fig. 3.10. In terms of the reflection coefficient results, observed in Fig. 3.11., simulation and experiment are in close agreement. The resonant dip in the measured reflection coefficient is shifted slightly below the intended resonant frequency of 100 GHz, and a bandwidth of approximately 6.7 GHz was measured, in comparison to the 7.66 GHz obtained for the simulation. Regarding the measured radiation pattern, the measurement in the anechoic chamber was performed in 5° intervals and it was only possible to measure from -90° to 90°, due to mechanical restrictions, while for the simulated results, it is shown in 1° intervals for all angles. Both simulated and measured radiation pattern were normalized and are shown in Fig. 3.12.
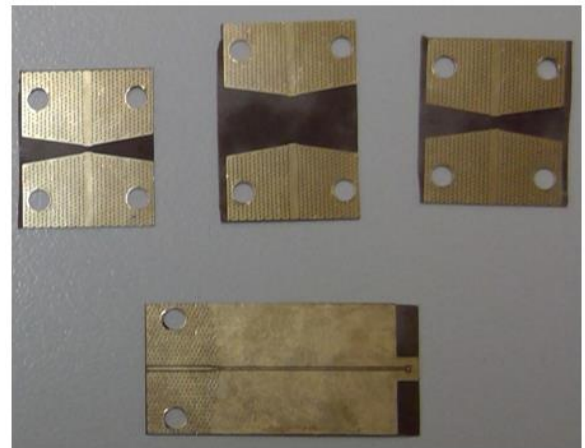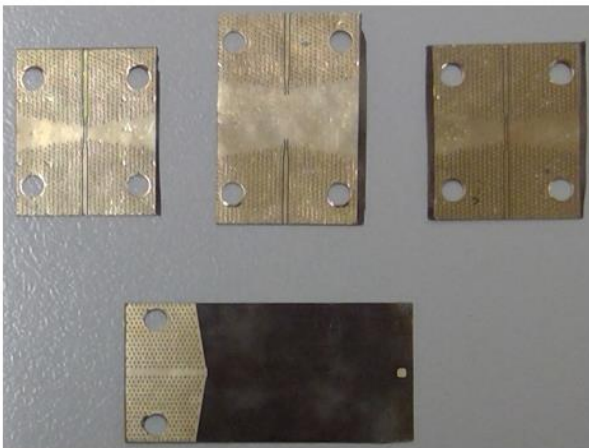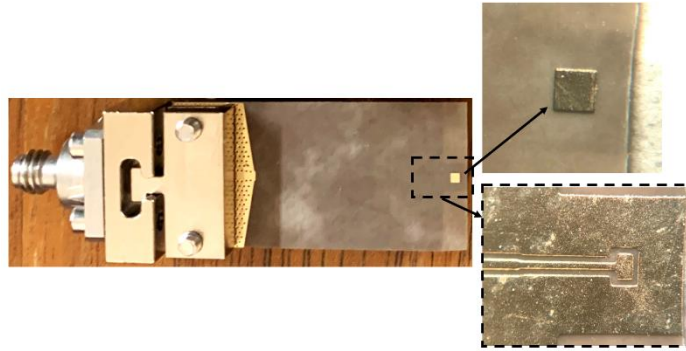
**Fig. 3.10.** Fabricated antenna element and TRL calibration kit.



| Name | X | Y |
|------|---|---|
| simulated_resonant_dip | 100.0000 | -34.9693 |
| simulated_bandwidth_right_side_limit | 103.8000 | -10.0819 |
| simulated_bandwidth_left_side_limit | 96.2000 | -10.0272 |
| measured_resonant_dip | 99.0500 | -39.0590 |
| measured_bandwidth_right_side_limit | 101.0000 | -10.1161 |
| measured_bandwidth_left_side_limit | 94.3000 | -10.1140 |
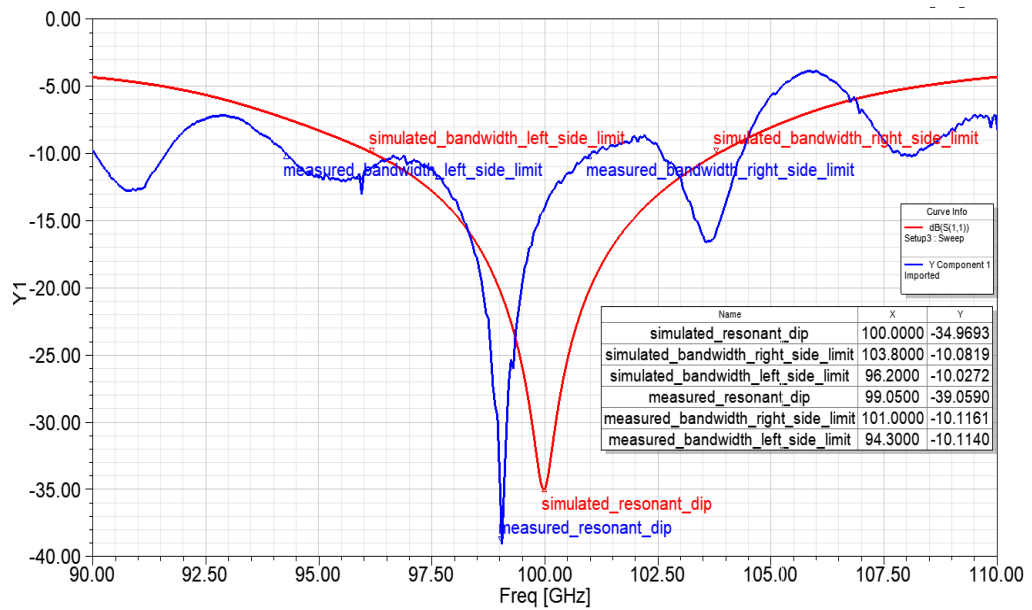
**Fig. 3.11.** Simulated and Measured Reflection Coefficient.



| Name | Theta | Ang | Mag |
|------|-------|-----|-----|
| Simulated | 0.0000 | 0.0000 | 6.0940 |
| Measured | 0.0000 | 0.0000 | 6.3326 |
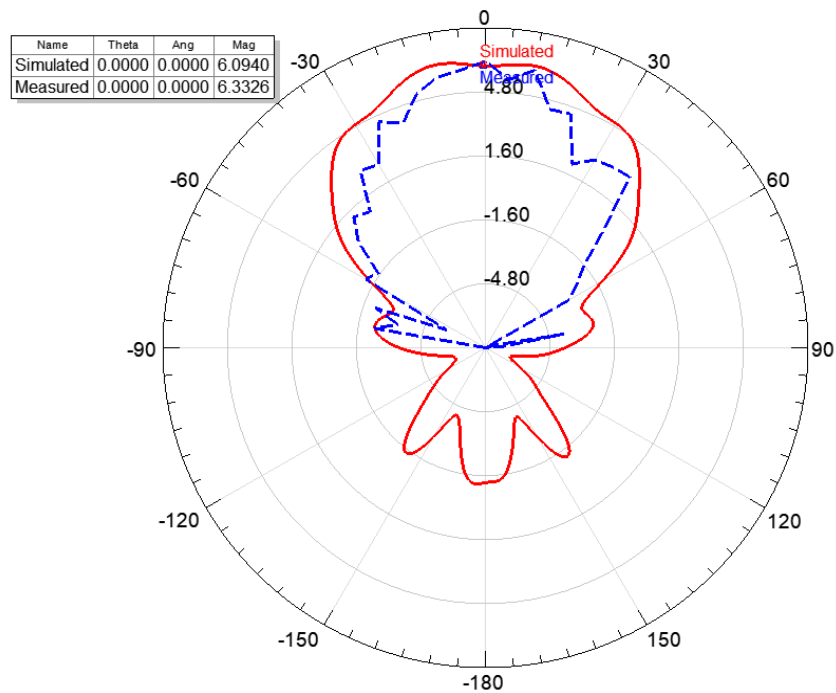
**Fig. 3.12.** Simulated and Measured Normalized Radiation Patterns for the θ plane, at φ = 0°.

37

## 3.5. Conclusions

In this chapter, an antenna element fed by a GCPW-CPW square loop feed on a 0.127 mm thick and $\varepsilon_r = 2.2$ substrate, including a TRL calibration kit, was designed, fabricated and characterized experimentally, having obtained at least 5 percent of fractional bandwidth. Further optimization and the application of this type of feeding method on an antenna array that also operates at a frequency of 100 GHz is a possible approach and its feasibility will be further discussed in the next chapter.

# Chapter 4: 4x4 Antenna Array Design

## 4.1. Introduction

In this chapter, a final design of a series fed 4x4 patch antenna array design, using a SIW feed network, is described, including the simulated components needed for the final design. Some previous design options will be discussed, justifying the final choice of a SIW feed network.

The use of a corporate feed network type was not feasible due to lack of space, considering the manufacturing constraints of the line and gap widths. For this reason, and in order to maintain a beam squinting free antenna array, the corporate feed network was discarded, directing focus to the differential series feed networks as an alternative.

For this design, as a way to decrease the random errors during experimental measurements, such as the flexibility of PCB board, as mentioned in the previous chapter, the substrate thickness was increased to 0.254 mm (from 0.127 mm) and the copper thickness increased to 0.035 mm (from 0.017 mm). The design constraints used for the antenna array was a conductor width and spacing of 0.1 mm, a via radius of 0.1 mm and an annular ring of 0.175 mm. These changes were only applied upon switching to the SIW Feed Network.

## 4.2. Feed Networks

### 4.2.1. Corporate and Series Feed Networks

The elements of an array can be feed by two types of feeding arrangements, either by a single line, referred as a series-feed network (Fig 4.1. (a)), or by multiples lines, designated corporate-feed network (Fig. 4.1. (b)).

Series fed techniques is restricted to be used in arrays to produce fixed beams with frequency dependent scanning and it can be used in linear and planar arrays with single or dual polarization. Apart from mutual coupling and internal reflections, any changes that occur in one element, affects all others. Since it adds phase delay, this technique is not suited for phase scanning arrays.

Corporate fed arrays provides more control over the feed of each element (amplitude and phase), and it is suited for scanning phased, multi-beam and shaped-beam arrays. This type of feed network is used to provide power splits of $2^n$, by using tapered lines or by using quarter-wavelength impedance transformers. Phase shifters control the phase of each element, while amplifiers/attenuators control the amplitude.

The use of either types of feeding networks, the radiation from the feedline imposes a limitation on the side lobe level and cross-polarization of arrays **[14] [34] [35]**.
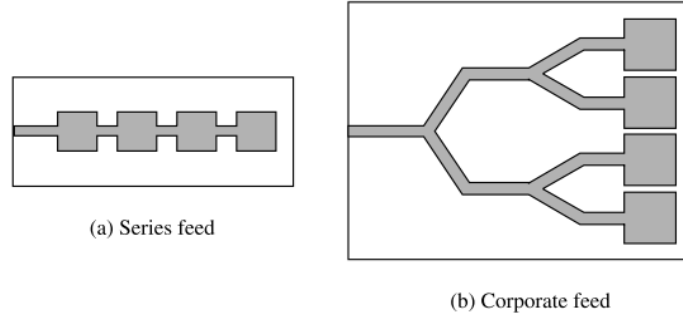


(a) Series feed

(b) Corporate feed

**Fig. 4.1:** Feed network types: series feed (a) and corporate feed (b) **[14]**.

## 4.2.2. Series Differential Feeding

Following up the comparison between series and corporate feed, in order to maintain frequency beam stability at a broadside direction, the series fed method is implemented by feeding an additional excitation signal to the second input port. In this case, the superposition of two radiation patterns of the cases when one port is excited with an input signal, and the other port is terminated is obtained (depicted in Fig 4.2.) **[9]**. If both ports are excited with the same phase difference, a subtraction of each individual signal's E-fields will occur at the centre of the series fed antenna array, creating a null in the radiation pattern at broadside ($\theta = 0^o$). A representation of the four cases of signal feeding of the structure from Fig. 4.2 are presented in Fig. 4.3. Assuming that the antenna array is geometrically symmetric in relation to the centre (at broadside), an E-field symmetric plane can be said to exist, a condition that allows the simulation of only half the series fed antenna array model **[12]**.
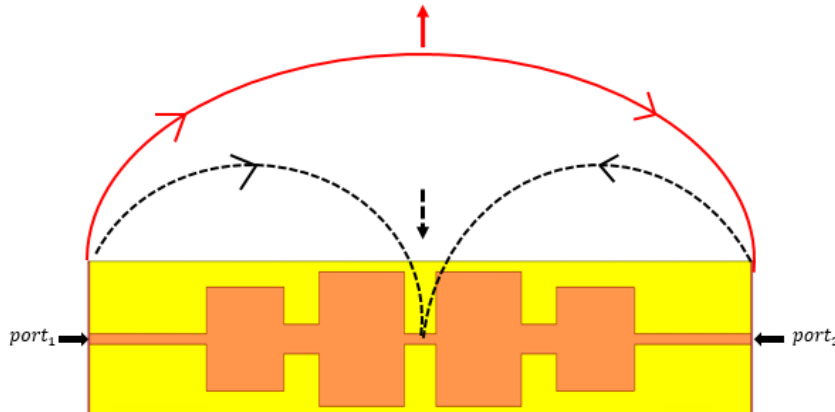
**Fig. 4.2.** E-field representation at broadside: dual fed antenna array when port phase difference = $180^o$ (solid line) and = $0^o$ (dashed line).
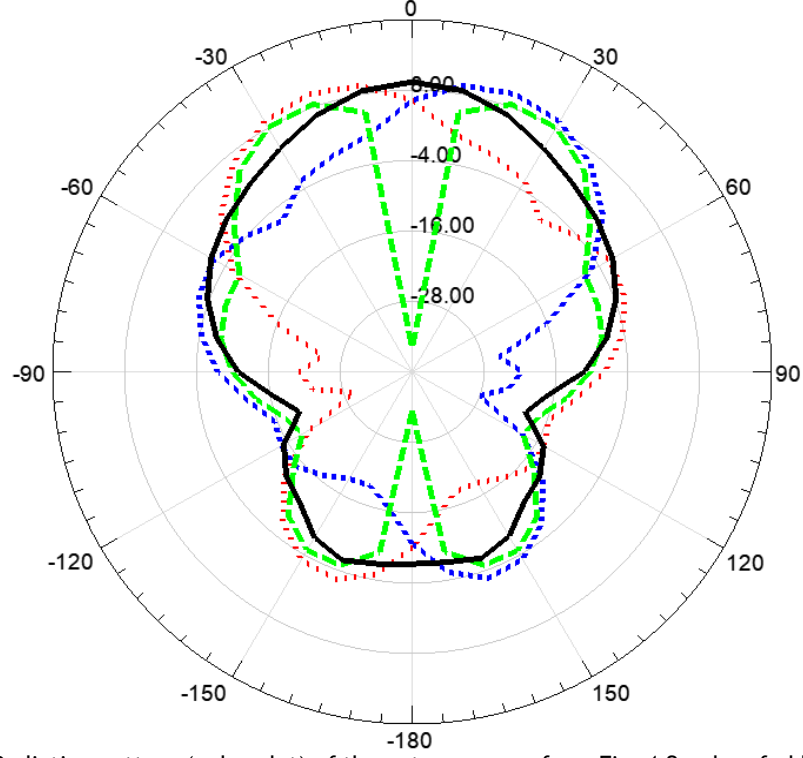


**Fig. 4.3.** Radiation pattern (polar plot) of the antenna array from Fig. 4.2. when fed by: only port 1 (dotted line), only port 2 (short dashed line), port 1 and 2 when $\Delta\theta = 0^o$ (long dashed line) and when $\Delta\theta = 180^o$ (solid line).

In order to create a radiation pattern with the main lobe at broadside, independent of the frequency, meaning both E-fields need to add up to each other, the phase difference between both feeds needs to be $\Delta\theta = 180^o$ **[36]**.

As mentioned before, regarding the antenna array theory, the overall radiation pattern is a result of the product of the field of the element and the array factors **[36] [34]**:

$$RF(\theta) = EF \cdot AF_{total} = EF \cdot \left(A_{port1} \cdot AF(\theta) + A_{port2} \cdot AF(-\theta) \cdot e^{j\Delta\phi}\right) \qquad (4.1)$$

where the magnitude and the phase difference of the excitation signals regarding both ports are, respectively:

$$A_{mag.} = \sqrt{A_{port1}^2 + A_{port2}^2} \qquad (4.2)$$

$$\Delta\phi = \theta_{port2} - \theta_{port1} \qquad (4.3)$$

## 4.3. CPW Feed network

Before reaching the description of the final antenna array design, various feed networks were designed and attempted, namely with the use of CPW and GCPW transmission lines. However, this approach led to some design issues, namely small dimensions that exceed the manufacture constraints and the high mutual coupling effects between antenna elements and feed network transmission lines, which led to their rejection, and as such, for the search for a more doable transmission line type. This turned out to be the SIW line.

Regarding the GCPW feed network, some issues arose first in the HFSS simulations, most likely due to incorrect impedance matching, as it was showing lower transmission coefficients when compared with the CPW feed network. Knowing that the GCPW transmission line provides better isolation performance than the CPW transmission line, only the CPW feed network was actually addressed. In spite of this, in order to justify its rejection, the CPW feed network was simulated and the following S-parameters were obtained, shown in Fig. 4.5, and the HFSS model with the wave port numbers depicted in Fig. 4.4.
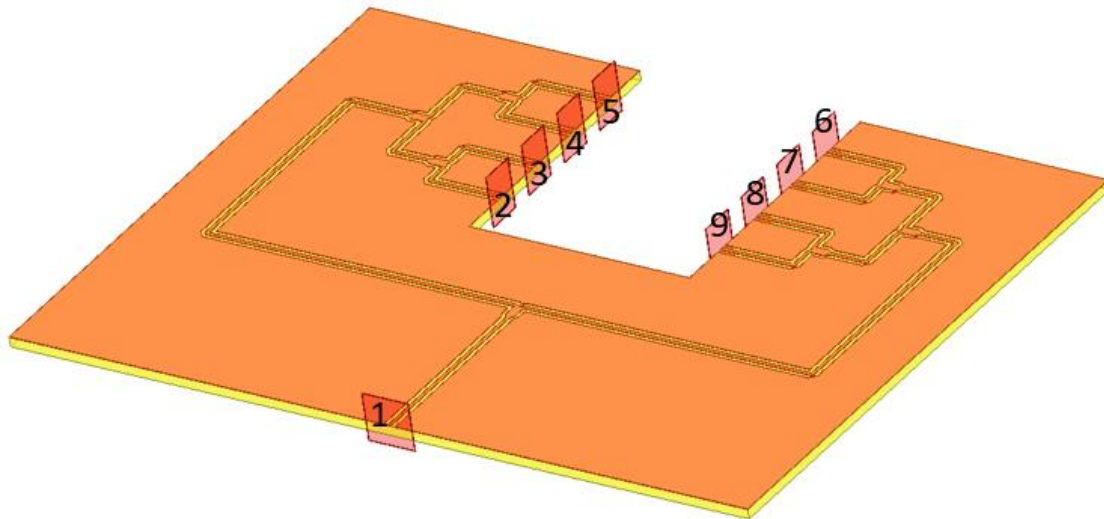


**Fig. 4.4.** HFSS model of the CPW Feed Network (with the port numbers depicted).
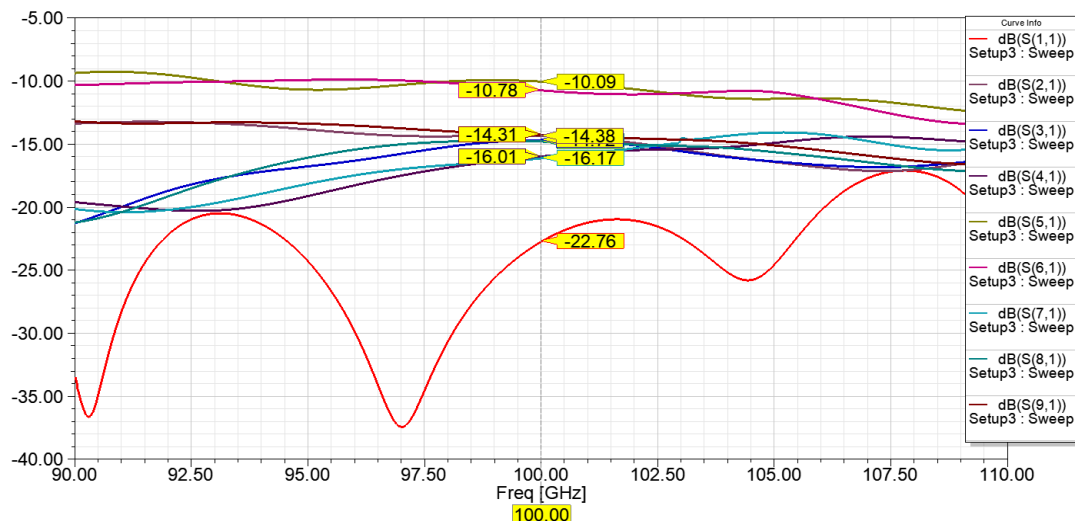
**Fig. 4.5.** Simulated S-Parameters of the CPW Feed Network.

Observing the obtained transmission coefficients of the simulation, it can be seen that the transmission coefficients are not similar, and so, the CPW transmission line does not provide enough isolation between lines, as the theoretical value should only be slightly above 9 dB, given that at least three T-junctions (equal split divider: -3 dB) [21] are used on each side of the differential feed network. Note that one of the sides will have a higher line loss, as it needs to be longer in order to create the necessary 180º phase difference.

Looking at these conclusions, another type of transmission line needs to be approached, one that can provide a better isolation, lower losses and still maintain a simple design implementation, for a single substrate layer.

## 4.4. SIW Feed Network

As mentioned previously, the Substrate Integrated Waveguide (SIW) was picked as an outstanding alternative transmission line for the feed network, providing a low manufacturing cost, low loss, high isolation and higher line bandwidth. It is also known as a recurrent transmission line type in planar compact components for millimetre wave applications [37] [38].

### 4.4.1. SIW Transmission Line

The substrate integrated waveguide (SIW) can be seen as a guided transmission line, such as a dielectric filled rectangular waveguide (DFW) [39], as depicted in Fig. 4.6. For a rectangular waveguide, where $a$ is the width and $b$ the height, the cut-off frequency of an arbitrary mode can be found with the following formula:

$$f_c = \frac{c}{2\pi} \sqrt{\left(\frac{m\pi}{a}\right)^2 + \left(\frac{n\pi}{b}\right)^2} \qquad (4.4)$$
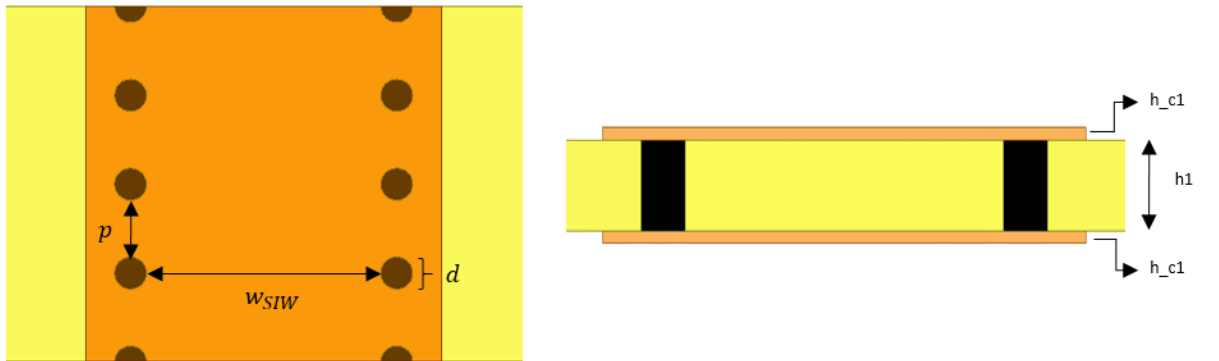


**Fig. 4.6.** SIW line schematic: top view (left) and transversal view (right).

Since there are vias at the sidewalls, resembling a discontinued wall, the transverse magnetic (TM) modes do not propagate and therefore dominant mode cut-off frequency is the same as the $TE_{10}$ mode of the rectangular waveguide. The previous equation can then be simplified to the following equation:

$$f_c = \frac{c}{2a} \tag{4.5}$$

The width of the DFW with the same cut-off frequency is given by:

$$w_{siw} = \frac{a}{\sqrt{\varepsilon_r}} \tag{4.6}$$

In order to implement an intermediate width sized SIW line, since the lower cut-off frequency increases with the decrease of the SIW line width, the chosen cut-off frequency was 70 GHz, as it is an arbitrary acceptable agreement between line width and cut-off frequency, obtaining a value of approximately 1.45 mm for $w_{siw}$, which as seen in Fig. 4.6, is the distance between the two parallel rows of vias that form the side walls. For this case, the substrate height is $h_1$ = 0.254 mm and copper thickness is $h_{c1}$= 0.035 mm.

Based on empirical rules, as seen in many SIW related works, regarding the placement of the vias, the diameter (d), the pitch (p) and guided wavelength ($\lambda_g$) should follow the following criteria, in order to minimize radiation loss, as leaky waves can radiate from the gaps between the vias, decreasing the efficiency of the SIW wave guiding property [38] [40]:

$$\lambda_g = \frac{2\pi}{\sqrt{\frac{\varepsilon_r (2\pi f)^2}{c^2} - \left(\frac{\pi}{a}\right)^2}} \tag{4.7}$$

$$d < \frac{\lambda_g}{5} \tag{4.8}$$

$$p < 2d \tag{4.9}$$

The values used for the diameter and pitch of the vias was d=0.2 mm and p=0.35 mm. Although only a substrate thickness of 0.254 mm was used for this case, a thicker substrate could be used has it decreases the influence of conductor loss of the SIW structure [40]. The simulated results of the S-parameters for the SIW line can be seen in Fig. 4.7.
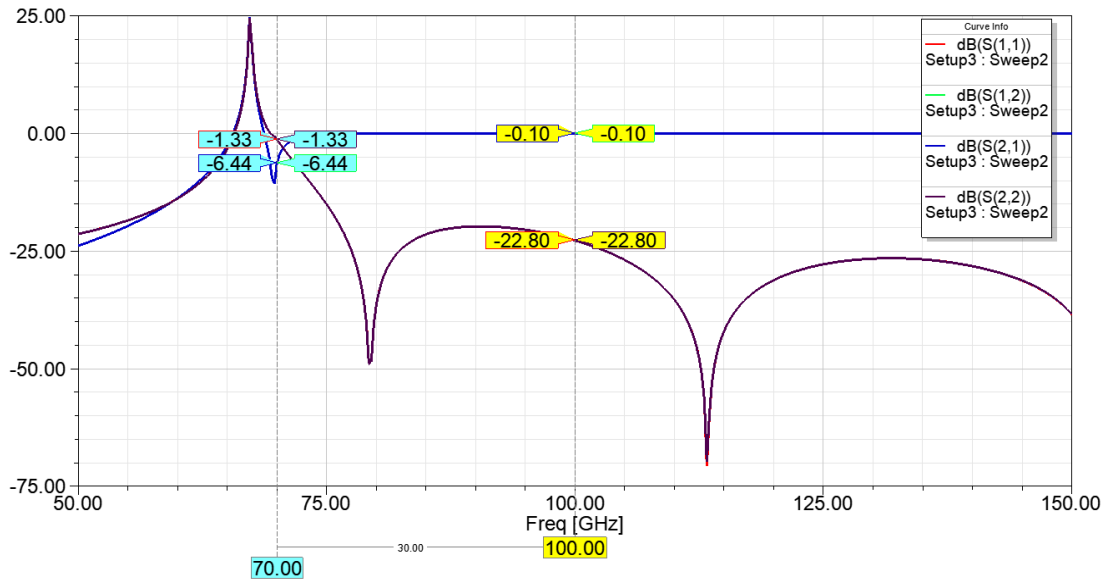
**Fig. 4.7.** Simulated S-Parameters of the SIW line.

### 4.4.2. SIW $90^o$ Bend

For the feed network in mind, multiple 90º bends of the SIW transmission line will be required in order to accomplish the differential feeding method. Wave propagation discontinuities, such as, bends or chamfers in planar transmission lines, if not properly compensated **[37]**, can lead to significant radiation loss, degradation of reflection and transmission coefficients, generation of odd propagation modes and efficiency reduction, the latter due to leaky EM waves. Hence the careful placement of the vias throughout the bend arcs, as seen in Fig. 4.8, is crucial for the S parameter performance of the SIW 90º bends **[12] [41]**.
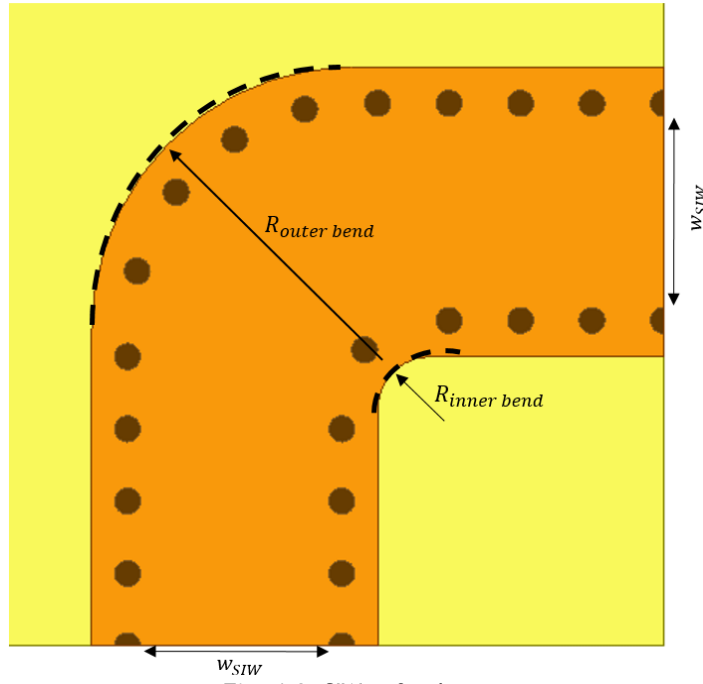
**Fig. 4.8.** SIW 90º schematic.

In this case, the outer radius arc of vias ($R_{outer\,bend}$) has 2mm of curve radius, while the inner radius arc has 0.4 mm of curve radius. The simulated S-parameter of the SIW 90º bend HFSS model in present in Fig 4.9.


**Fig. 4.9.** SIW 90º simulated S-parameters.

### 4.4.3. SIW 1x2 Power Divider

Given that a differential feeding method will be used on this feed network, both SIW lines coming from the series fed antenna array need to be merged into one SIW line, where the excitation signal is applied. Hence a 1x2 power divider was designed and implemented, as shown in Fig 4.10.
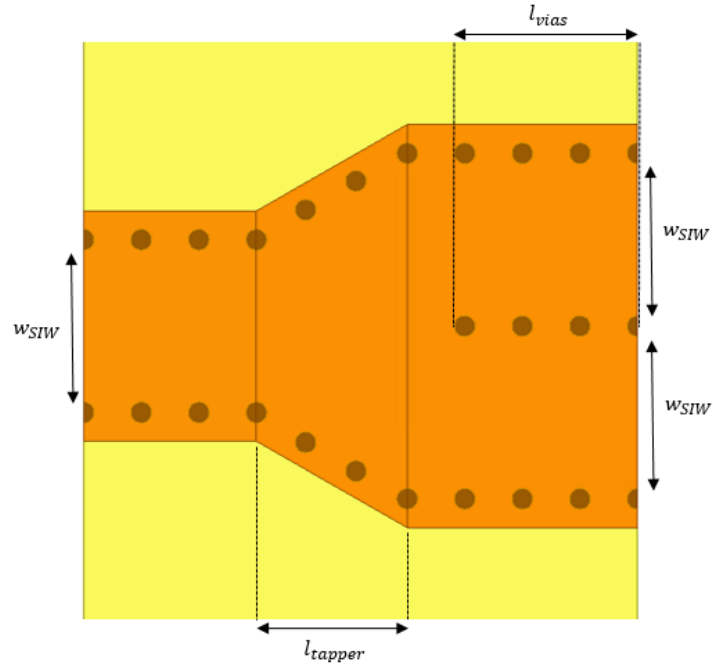
**Fig. 4.10.** 1x2 SIW power divider schematic.

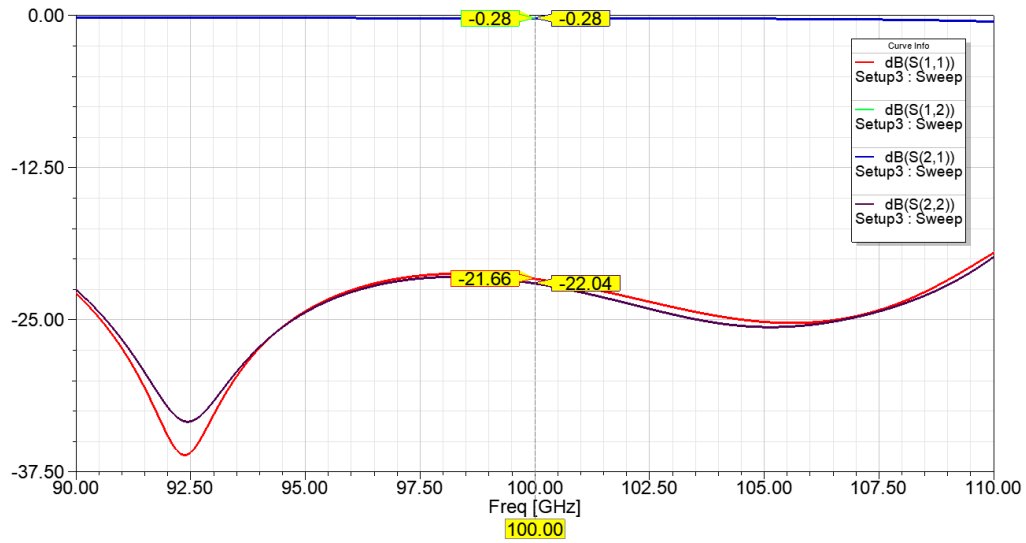This SIW power divider geometric shape, based on the work in **[12]**, has a few parameters that heavily influence the S-parameter performance of the power divider, namely the length of the tapper ($l_{tapper}$) and the number of vias ($l_{vias}$) placed of the middle row, that separate both output transmission lines. After parametric sweeps, the values for $l_{tapper}$ and $l_{vias}$ obtained were 1.44 mm and 1.75 mm respectively. The simulation results of the S-parameters are depicted in Fig. 4.11., in which port 1 is the input port (left side) and ports 2 and 3 are the output ports (right side) of Fig. 4.10.



**Fig. 4.11.** 1x2 SIW power divider simulated S-parameters.

It can be observed from Fig. 4.11 that the values obtained for the transmission coefficients are very close to the theoretical value of an equal split power division ratio of -3 dB of a power divider.

### 4.4.4. SIW 1x4 Power Divider

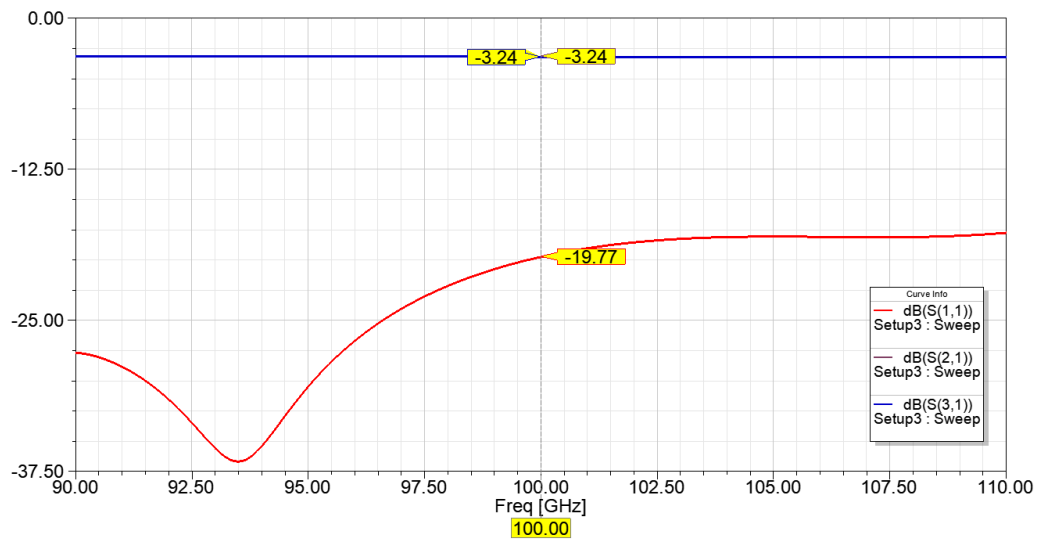Following similar reasons, but different purposes, in comparison to the 1x2 power divider, a 1x4 power divider will be necessary to feed a 4x4 series fed antenna array that has four ports on each side, where signal coming from the 1x2 power divider will need to be divided yet again into four separated SIW transmission lines. The 1x4 power divider schematic is presented in Fig. 4.12.
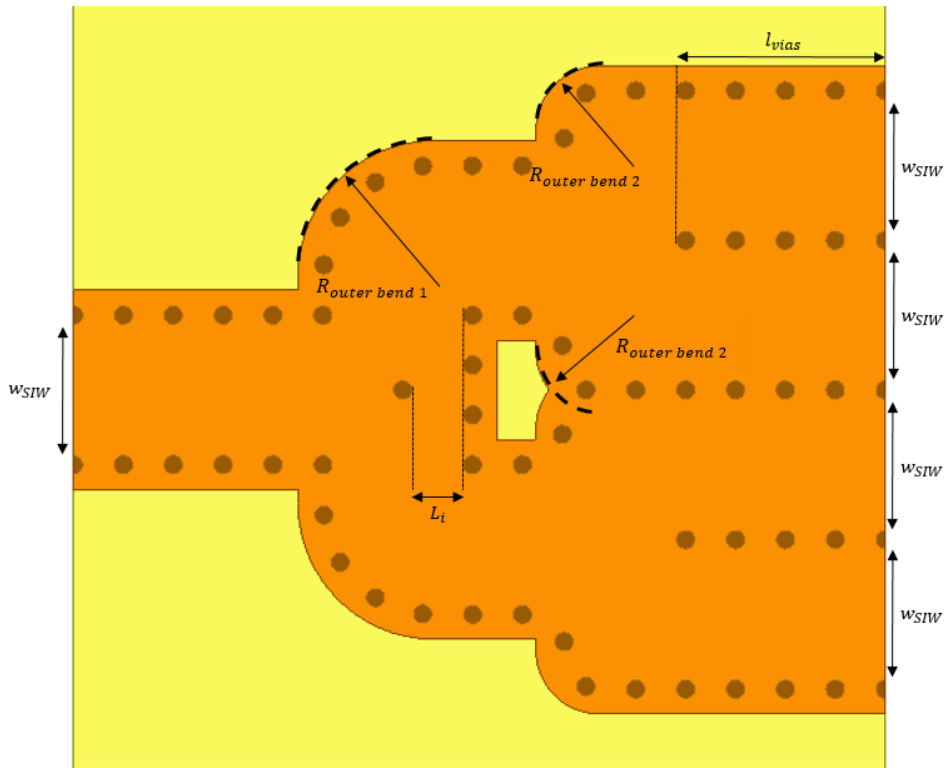


**Fig. 4.12.** 1x4 SIW power divider schematic.

Regarding the 1x4 power divider, a similar design approach, as used in the 1x2 power divider and in the 90° bend, namely the optimization of the variable $l_{vias}$ and the $R_{outer\ bend}$ variables. For this design, $R_{outer\ bend\ 1}$ = 1.5 mm, $R_{outer\ bend\ 2}$ = 0.7 mm and $l_{vias}$ = 2.3 mm. The main difference in this design was the inclusion of an inductive post after the input line in order to obtain optimum reflection and transmission coefficients. In this design, only the distance between the via wall near the output of the first 1x2 power divider and the inductive post was manipulated, opting for a value of $L_i$ = 0.275 mm, obtaining the S-parameters depicted in Fig. 4.13 **[42]**.

**Fig. 4.13.** 1x4 SIW power divider simulated S-parameters.

From the results, a reflection coefficient below -10 dB was obtain for the entire frequency band of interest and transmission coefficients near the -6 dB theoretical value, equivalent to two consecutive T-junctions. Slight differences were obtain between both pairs of output ports, due to some phase non-uniformity after the SIW line divisions.
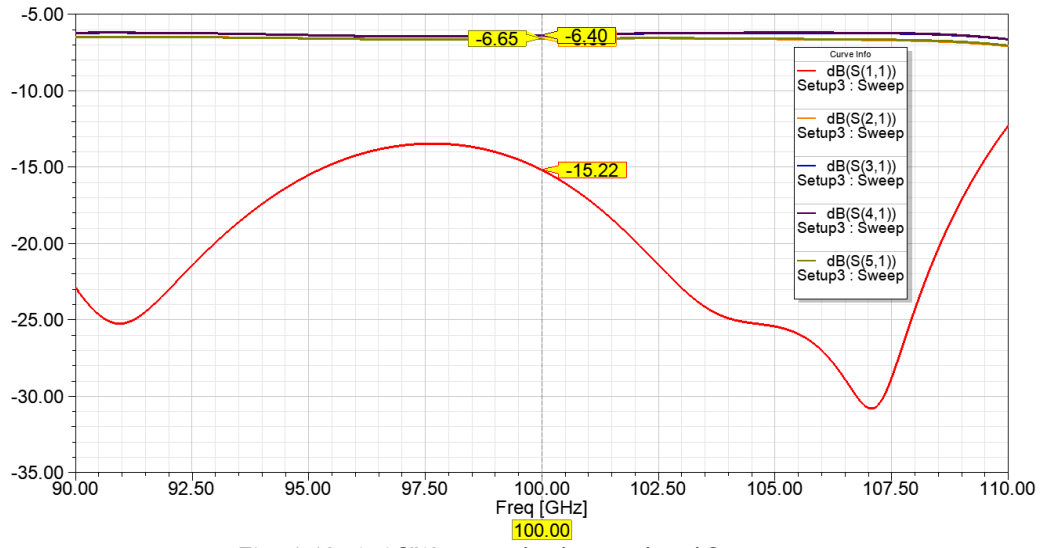
## 4.4.5. SIW to GCPW Transition

In order to perform experimental measurements, the antenna array structure needs to be attached to a connector, the same one already mentioned in Chapter 3, which supports the GCPW or microstrip transmission lines. Given the advantages of GCPW over microstrip lines at millimetre wave frequencies, as it is less prone to radiate and has higher isolation, very weak mutual coupling effects and it is not very sensitive to substrate thickness, hence allowing a wide range of line impedance **[20]**, a GCPW to SIW transition was also designed. The width and gap for the GCPW line used, for a substrate height of 0.254 mm and copper thickness of 0.035 mm, was $W_0$ = 0.559 mm and gap = 0.1 mm respectively, obtaining a line impedance of nearly 50 Ω. The overall schematic of the transition is present in Fig. 4.14.
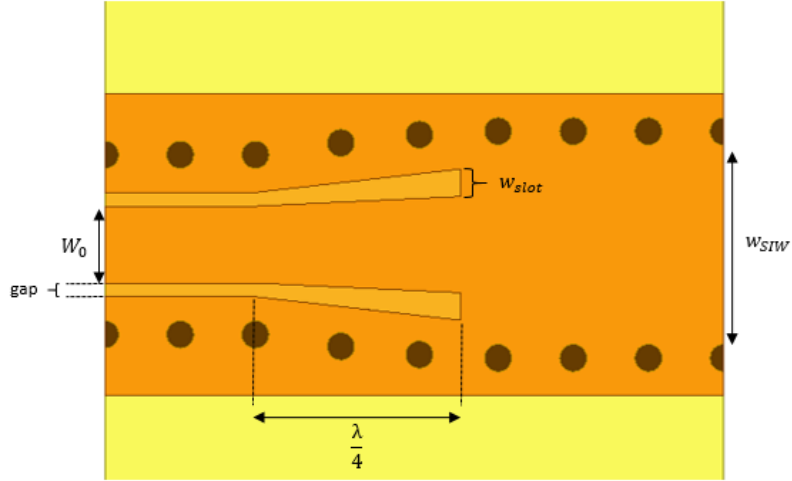
**Fig. 4.14.** GCPW to SIW transition schematic.

Based on work in **[41]**, the actual transition section is composed by a tampered coupling slot in a triangle shape, in which a wide bandwidth is obtainable in the frequencies of interest and allows the direction of the E-field in the coupling slot to stay perpendicular to the SIW sidewalls. In this design, vias are purposely placed along the GCPW line portion to avoid any parallel plate modes and to stop the waveguide modes to pass across, from the SIW to the GCPW section.

It was suggested in the author's work that the taper coupling slot length should be $\lambda/4$ at the centre frequency. Only one variable was subjected to parametric sweeps which was the taper coupling slot width, and a value of $w_{slot}$ = 0.2 mm was chosen as the optimum value. The simulated S-parameters of the GCPW to SIW transition HFSS model is presented in Fig. 4.15.



**Fig. 4.15.** GCPW to SIW transition simulated S-parameters.

## 4.4.6. SIW to microstrip Transition

50

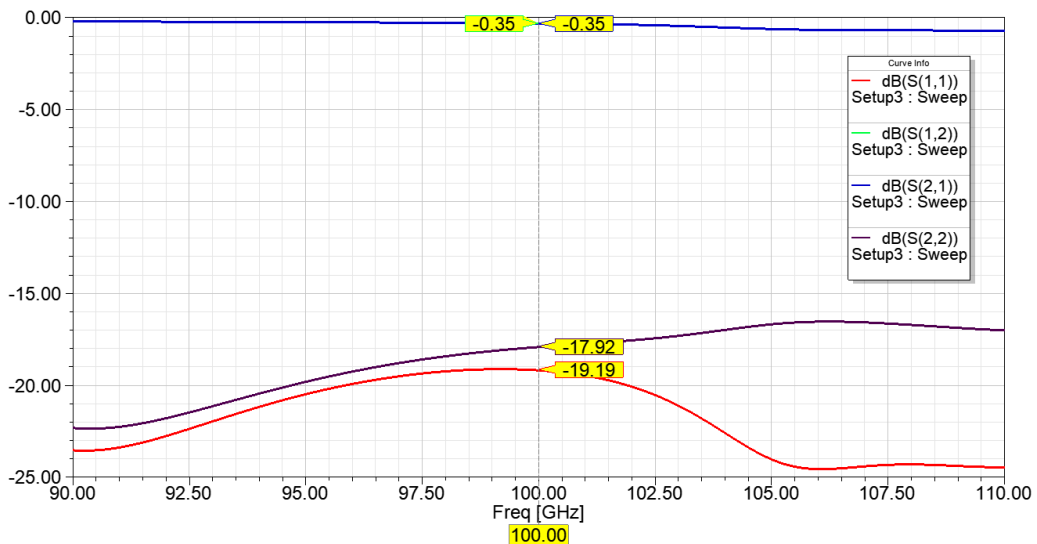Before going into details regarding the SIW to microstrip transition, it is to be noted that: a previous attempt to design a CPW differential series fed antenna array was performed, but after analysing the obtained results, a radiation pattern with a very low front-to-back ratio was observed, with approximately ≈13 dB in the front lobe and ≈7 dB in the back lobe, which led to opt for the use of an antenna type with a bottom reflector plane, typical of the microstrip antenna configuration. Although the use of microstrip lines is undesirable at sub-terahertz frequencies, due to the lack of other alternatives, this approach was carried on. For this reason, instead of a CPW design, it was decided to use a microstrip technique. Only the transition from SIW to microstrip will be presented, and not the SIW to CPW transition. A schematic of the transition is present in Fig. 4.16.
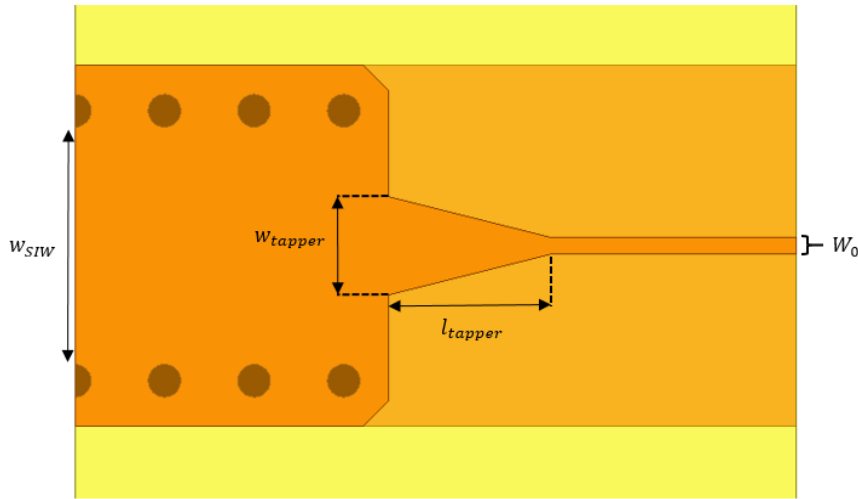


**Fig. 4.16.** SIW to microstrip transition schematic.

In order to connect the SIW feed network to the dual fed antenna array, a transition from SIW to microstrip is mandatory to implement. The transition consists of a tapered line on one of the plates of the SIW, leading into a microstrip line, converting the SIW impedance to the standard microstrip impedance [43]. The parametric swept variables were $w_{tapper}$ and $l_{tapper}$, for which the optimized values are 0.6 mm and 1 mm respectively. The transition simulated S-parameters are shown in Fig. 4.17. Given that, at very high frequency, the width of the microstrip line should be narrow, less than $\lambda_0/8$ , where $\lambda_0$ is the wavelength at the centre frequency, according to [20], in order to avoid high radiation losses, the line width was set to $W_0$ = 0.1 mm, which was the defined design constraint for the full 4x4 antenna array. The simulated impedance value was 119.88 Ω.
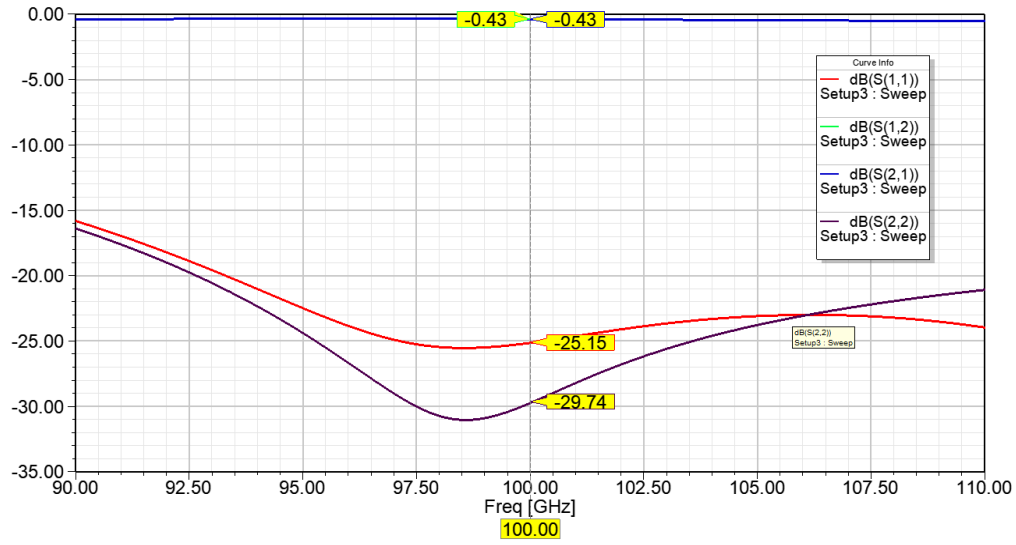
**Fig. 4.17.** SIW to microstrip transition simulated S-parameters.

## 4.4.7. Full Feeding Network

Finally, with all the components necessary, the final SIW feed network, presented in Fig. 4.18., was assembled and simulated. As seen from said figure, the right SIW arm was extended in length, in comparison to the left arm, in order to create an outphasing of $180^o$, which can be seen in Fig. 4.19, necessary for the differential feeding method. The phase difference between transmission coefficients: ang(S(6,1))-ang(S(2,1)), ang(S(7,1))-ang(S(3,1)), ang(S(8,1))-ang(S(4,1)) and ang(S(9,1))-ang(S(5,1)) take a value close to $180^o$ .
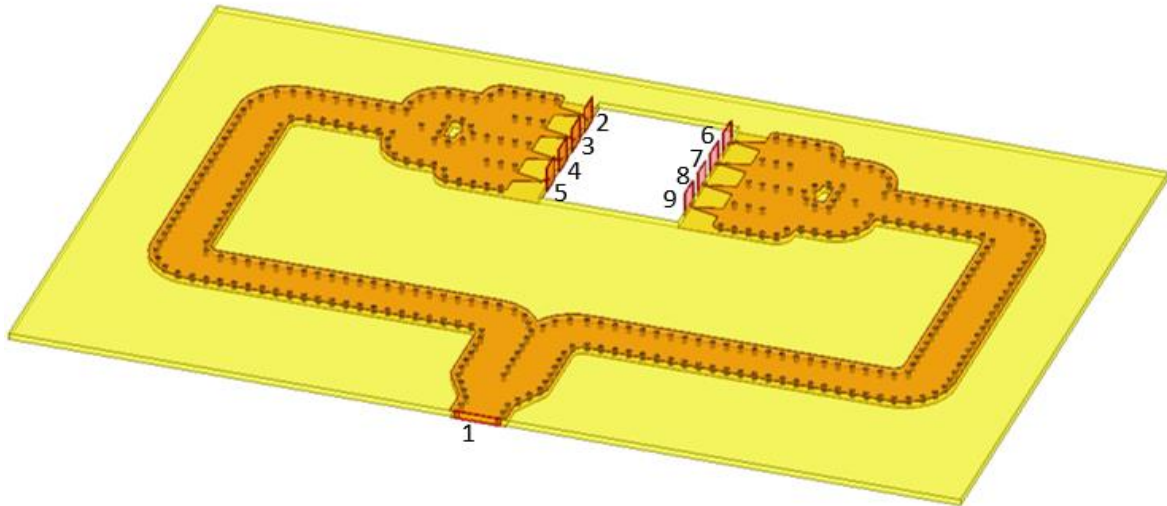


**Fig. 4.18.** HFSS model of the SIW Feed Network (with the port numbers depicted).
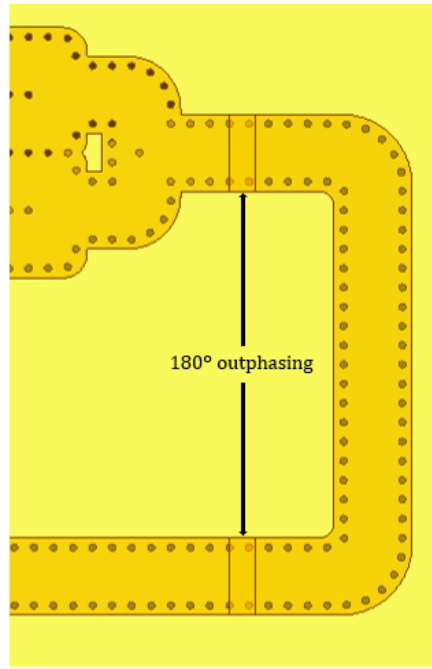
**Fig. 4.19.** Representation of the right arm of the SIW Feed Network and the extra line length to create a 180$^o$ outphasing.

Depicted in Fig. 4.20., the simulated S-parameters results of the feed network, from Fig. 4.18., show that the transmission coefficients improved moderately and its similarities in magnitude show that there is a smaller phase difference between output ports in comparison with the CPW feed network. Although the reflection coefficient does cover the entire frequency band of interest, regarding the -10 dB limit, it is observed that at some frequencies, the magnitude of the reflection coefficient is very close to the -10 dB limit, which could very much surpass the -10 dB border upon the manufacturing process.



**Fig. 4.20.** Simulated S-Parameters of the SIW Feed Network.

## 4.5. Passive and Active S-parameters

The scattering matrix gives out a description of the incident, reflected and transmitted waves of an N-port network, when dealing with high frequency networks. This matrix relates the incident voltage waves on the ports to those reflected from the ports. The scattering parameters, which are frequency dependent, can be calculated using network analysis techniques, or they can be measured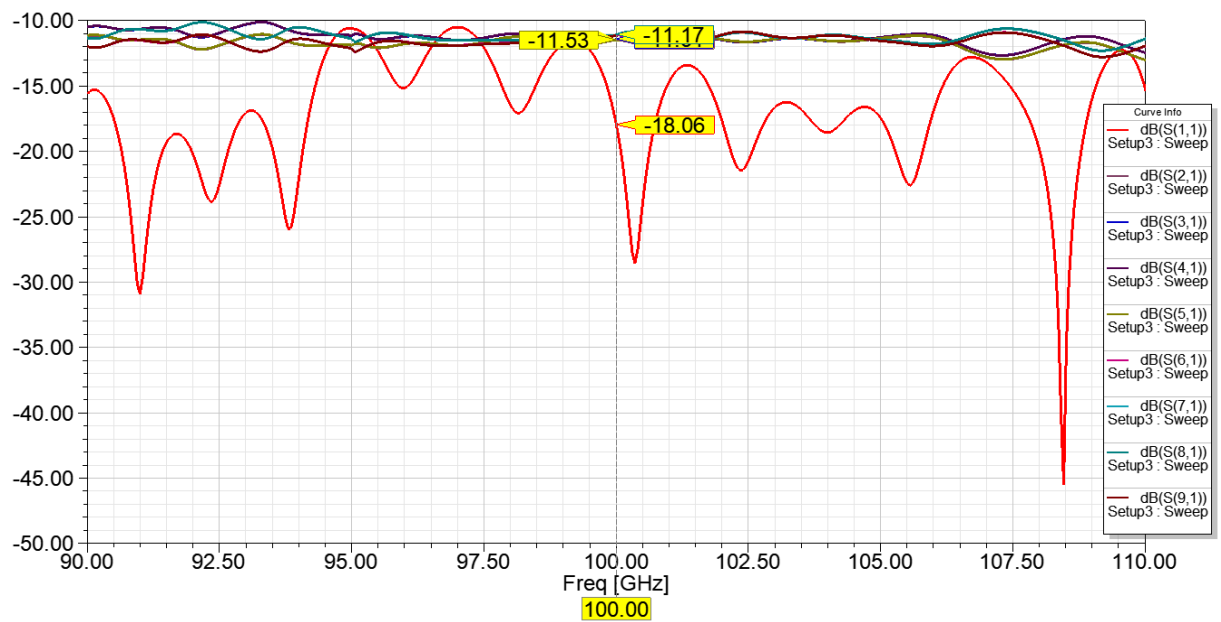 directly with a vector network analyzer (VNA). The scattering matrix, or [S] matrix, is defined by the relation between the incident and reflected voltage waves:

$$[V^-] = [S][V^+] \tag{4.10}$$

Specific elements of the [S] matrix can defined as:

$$S_{ij} = \left.\frac{V_i^-}{V_j^+}\right|_{V_k^+ = 0 \; for \; k \neq j} \tag{4.11}$$

where $V_i^-$ is the voltage of the reflected wave at port $i$ and $V_j^+$ is the voltage of the incident wave at port $j$.

In general, $S_{ij}$ represents the voltage amplitude transferred from Port $i$ to Port $j$ in a multi-port network. So $S_{ii}$ is the reflection coefficient seen looking into port $i$ when all the other ports are terminated in matched loads, while $S_{ij}$ is the transmission coefficient from port $j$ to port $i$ when all other ports are terminated in matched loads. Changing the terminations or excitations of a network does not change its scattering parameters, but it can change the reflection coefficient seen at a given port, or the transmission coefficient between two ports, so care must be taken when analysing such cases. If the device is passive and contains no anisotropic materials, its scattering matrix will be symmetric $S_{ij} = S_{ji}$ **[21]**. A two-port port network is depicted in Fig. 4.21, as well as a signal flow graph representation in Fig. 4.22.
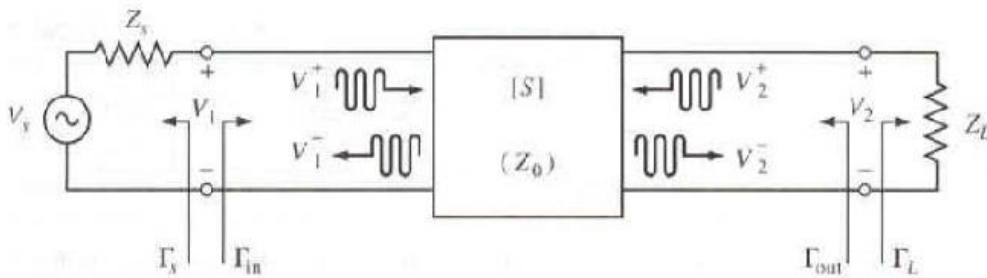


**Fig. 4.21.:** A two port network with general source and load impedance **[44]**.

So, in a two-port network (port 1 and port 2), a parameter $S_{11}$ defines the amplitude of the reflected voltage wave back to port 1 relative to the input power to port 1 (reflection coefficient), while the parameter $S_{21}$ defines the voltage amplitude received at port 2 relative to the power input to port 1 (transmission coefficient) **[21] [45]**.
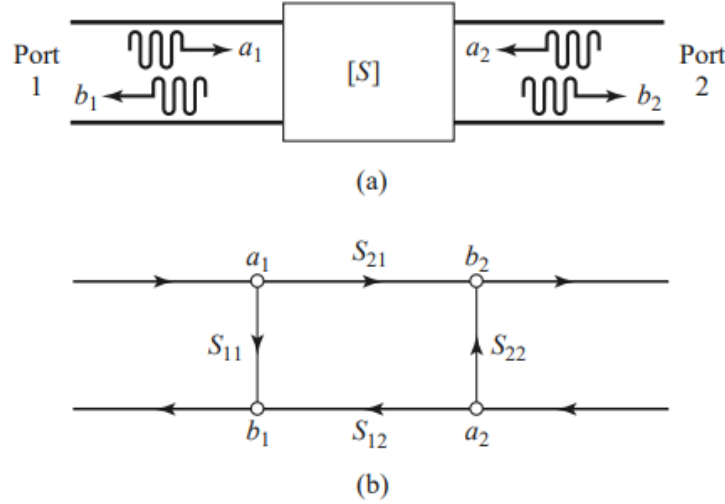


**Fig. 4.22.:** Signal flow graph of a two-port network: incident/reflected waves (a) and signal flow graph (b) **[21]**

For the case of differential feeding, both port voltages will be different from 0 and are simultaneous active in a two-port network (such scenario can be applied to a multi-port network), meaning that said network cannot be analyzed with the standard passive reflection coefficients, as it assumes that only one port is active at any given time, but all simultaneous port contributions must be taken into account.

A study and analysis of active S-parameter theory is performed in **[46]** and **[12]**, and for the case of differential feeding in symmetrical two port network, where $V_2 = -V_1$, the following is obtained: $S_{11a} = S_{22a} = S_{11} - S_{12} = S_{22} - S_{21}$.

The electromagnetic simulator HFSS possesses in-built active S-parameter options to plot the reflection coefficient graphs and facilitates the analysis of its behaviour.

## 4.6. 4x4 patch antenna array

In this section, the steps regarding the design and implementation of the differential series fed 4x4 patch antenna array will be discussed, as well as, changes that were made to the final design as further simulations were conducted. For this design, an array of uniformly-spaced alike antenna elements of equal magnitude and progressive phase between elements was chosen due to its simplicity – Uniform Distribution **[47]**. As simulations were being performed, it was concluded that, the transitions needed to connect the SIW feed network to the antenna array were the main source of radiation loss closest to the antenna array, since there are four

1x4 series fed antenna array, hence four parallel microstrip lines, four transitions are used on each side of the array, inducing noticeable side lobes to the antenna array radiation pattern. So in order to account the influence of the SIW-microstrip transitions and facilitate the optimization process, a HFSS model with both the antenna array and transitions together was designed and simulated.

### 4.6.1. SIW-Microstrip Antenna Array with transitions

After performing simulations, firstly with only the 4x4 antenna array, this design is composed by four parallel 1x4 series-fed antenna arrays. The wave ports were placed next to the feed line leading into the first patch of each of the 1x4 series fed antenna array. For the antenna array, port placement and variables simulated are depicted in Fig. 4.23., and the final variable values shown in Table 4.1.
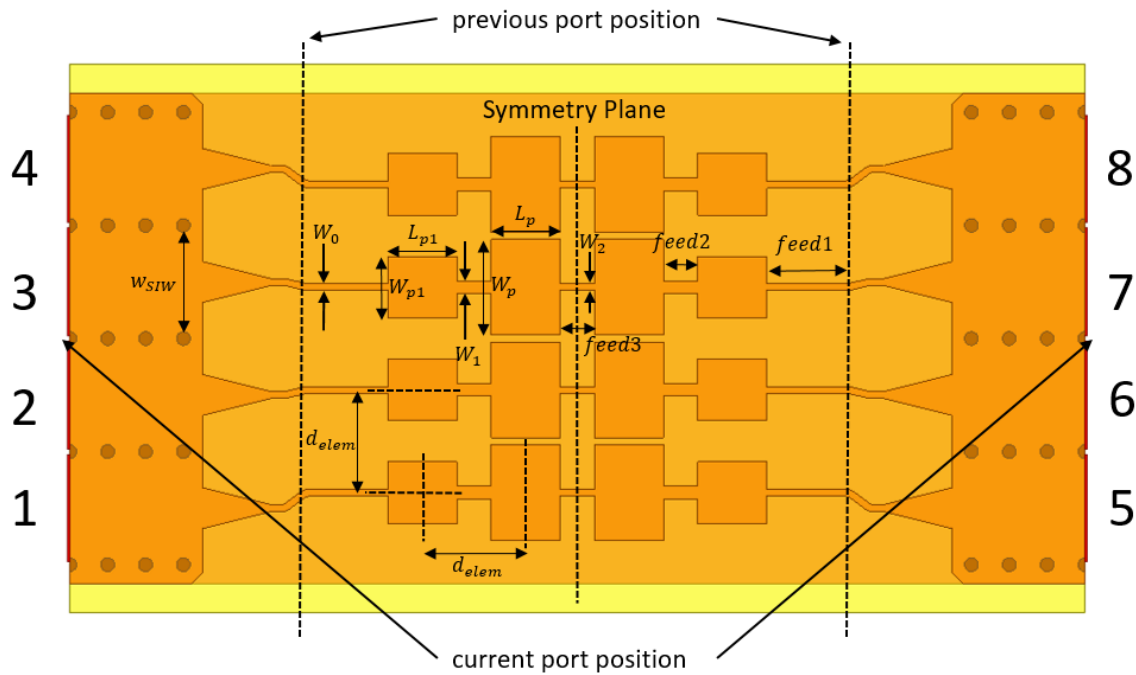


**Fig. 4.23.** HFSS model of the 4x4 microstrip series-fed antenna array with SIW-microstrip transitions included.

**Table 4.1** — Variable values for a 1x4 series-fed patch antenna array.

| Variable | Values (mm) |
|---|---|
| $W_p$ | 1.4 |
| $L_p$ | 1 |
| $W_{p1}$ | 0.9 |
| $L_{p1}$ | 1 |
| feed1 | 1 |
| feed2 | 0.5 |
| feed3 | 0.5 |
| $W_2$ | 0.1 |
| $W_1$ | 0.185 |
| $W_0$ | 0.1 |
| $d_{elem}$ | 1.5 |

Since each SIW line, depicted by $w_{SIW}$, is wider than the distance between the centres of each element $d_{elem}$ , after the SIW to microstrip, a curved microstrip line had to be placed to the feed line to each of the 1x4 series-fed arrays. In this design, to avoid grating lobes while using a broadside antenna array, the spacing between each antenna element is spacing is 1.5 mm ($d_{elem}$), which corresponds to half a wavelength at the centre frequency of operation (100 GHz). It is also worth mentioning that the patch width cannot exceed 1.4 mm, otherwise the patch antennas would touch each other, and hence radiation efficiency couldn't be further improved due to this restriction.

Given the total width of the four SIW lines in parallel, coming from the 1x4 power divider, the microstrip curves of the interior ports: 2, 3, 6 and 7 will have a shorter total length in comparison with the lines applied to the exterior ports: 1, 4, 5 and 8, and so there will be a transmission coefficient phase difference between interior and exterior lines. A simulation was performed, and the phase difference was minimal, yet a method presented in **[48]** was tested in this design, where one or more vias from the via rows that separate the interior (2, 3, 6, 7) from the exterior lines (1, 4, 5, 8), depending on the amount the phase shift needed, were shifted, inwards or outwards, allowing to reduce the phase difference to a value close to $0^o$. The disadvantaged to this method is that, as the via shift increases, the performance regarding the S-parameters of the feed network is degraded.

Upon further testing, an outward shift of about 0.116 mm is sufficient to impact the performance of the S-parameters, but simultaneously it was observed that the radiation pattern of the antenna did not change significantly. Hence this method wasn't applied to the design.

The obtain simulation results are shown in Fig. 4.24., for the active S-parameters, and in Fig. 4.25., for the radiation patterns.
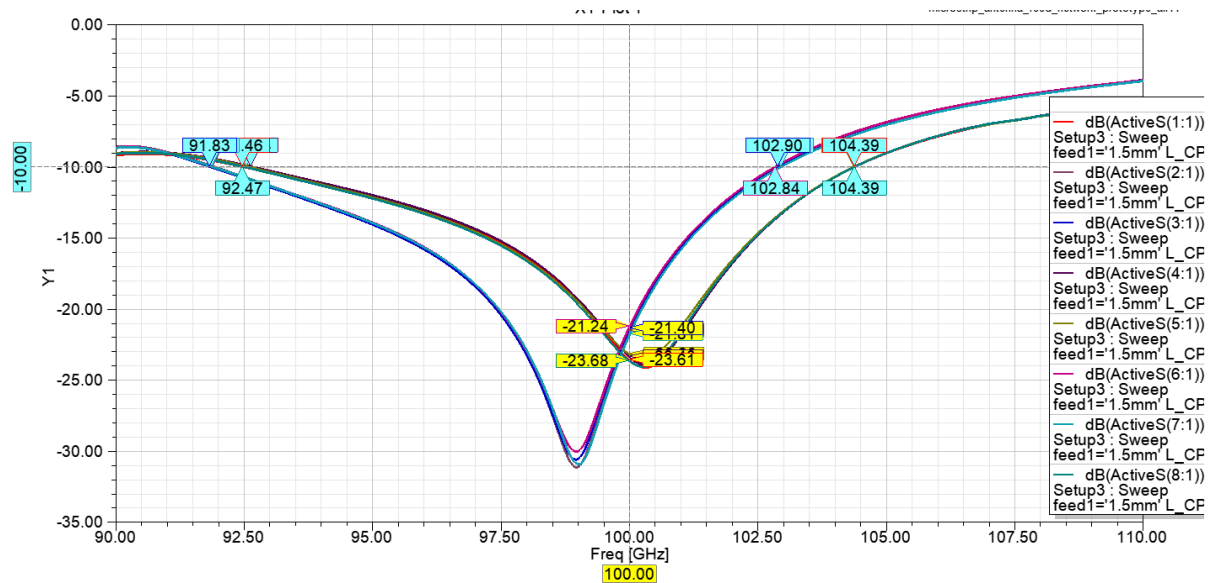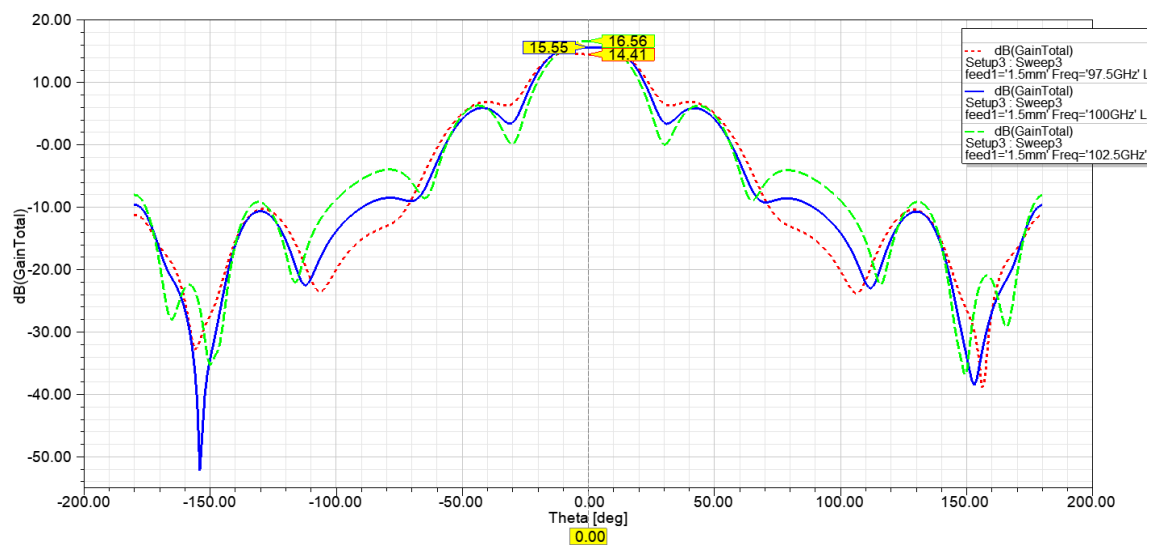


**Fig. 4.24.** Simulated active S-parameters of the 4x4 microstrip series-fed antenna array with SIW-microstrip transitions included.
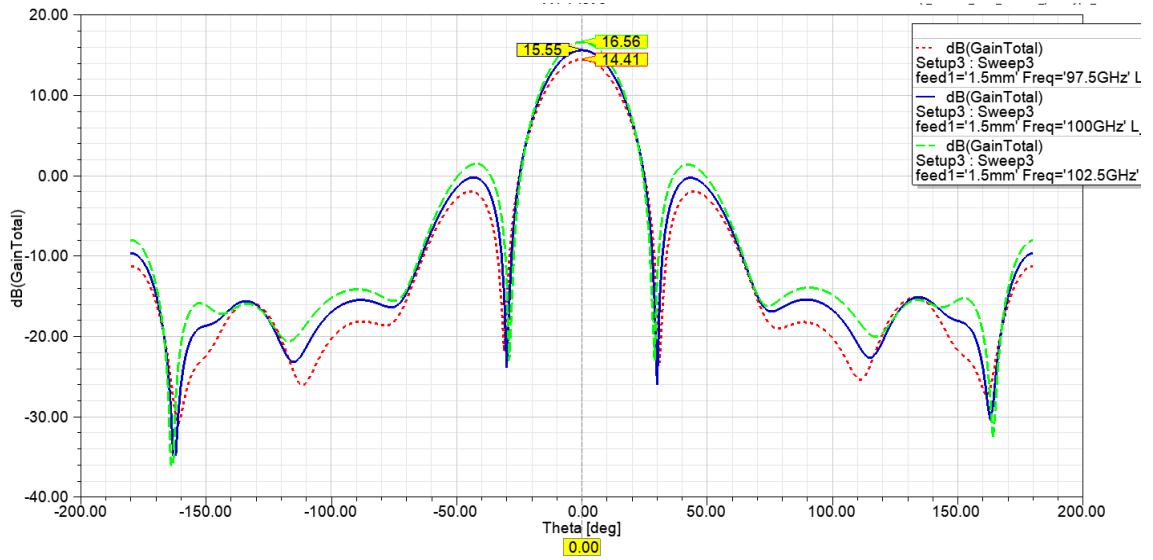
**Fig. 4.25.** Simulated active S-parameters of the 4x4 microstrip series-fed antenna array with SIW-microstrip transitions included (for the θ plane, φ = $0^o$ (top plot), φ = $90^o$ (bottom plot)).

From Fig. 4.24., it can be observed that, due to mutual coupling between all four parallel 1x4 series-fed arrays, the reflection coefficients of the inward ports have their resonant peak at around 99 GHz, meanwhile at the outward ports, the resonant peak is slightly above 100 GHz. A minimum of 5% fractional bandwidth (5 GHz) was also obtained.

Regarding the radiation pattern results, it was obtained, for a frequency of 100 GHz, a peak gain of 15.55 dB at broadside, it is also observed that the radiation pattern has a fixed beam at broadside for multiple frequencies, validating the absence of beam squinting.

## 4.6.2. Full Antenna Array

Connecting the SIW feed network with the microstrip 4x4 series-fed antenna array, the radiation pattern depicted in Fig. 4.28 was obtained (blue long dashed line curve). Although the reflection coefficient of the input port, at the TRL reference plane, showed an acceptable bandwidth, the obtained radiation pattern depicts moderate side lobes, with both lobes near a magnitude of 5 dB. This is a consequence of the SIW-microstrip transitions having radiation losses and adding its contribution to the radiation pattern. As an attempt to reduce said side lobes, an excess of microstrip line, that leads into the first patch antenna of each 1x4 series-fed array, was removed, effectively reducing the physical distance between the first patch and the transition, as presented in Fig. 4.26. After a simulation with the altered structure, the radiation pattern obtained is depicted in Fig. 4.28 (solid red line). It is observed that, due to both patches and transitions being closer to each other, the side lobes somewhat merged partially with main lobe, effectively increasing its peak gain by roughly 1 dB. The simulated reflection coefficient, presented in Fig. 4.29. (solid red line). The final HFSS model with the last modification is presented in Fig. 4.27.
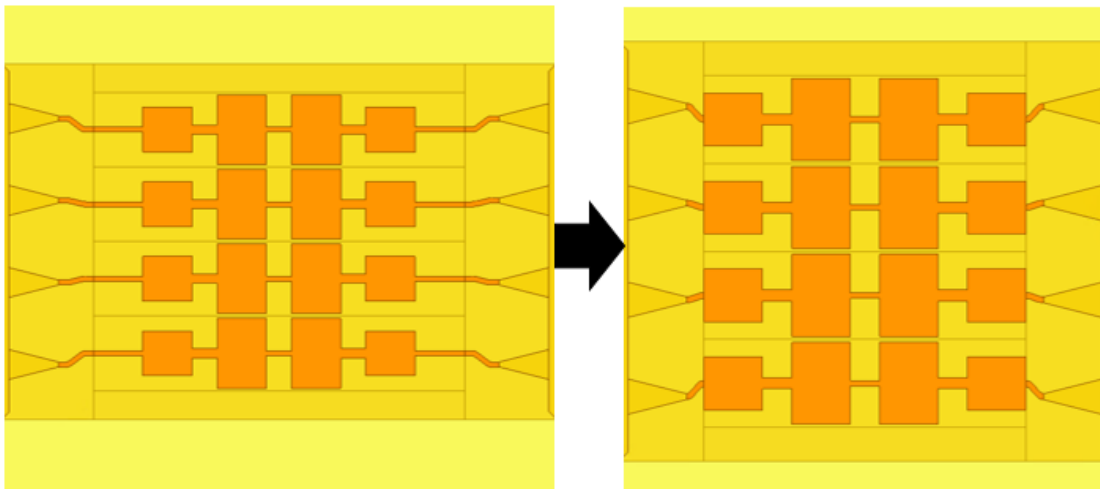
**Fig. 4.26.** HFSS models before (left side) and after (right side) the removal of the excess microstrip line, situated between the SIW-microstrip transition and the first patch.
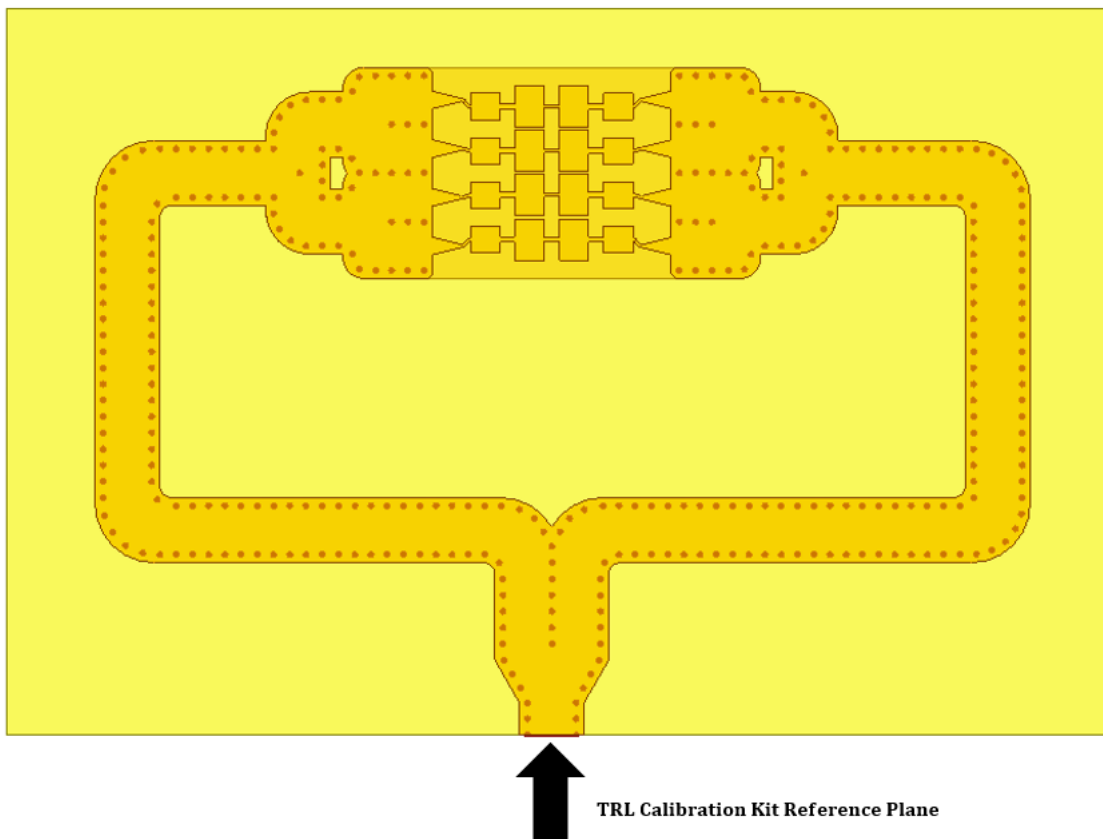


**TRL Calibration Kit Reference Plane**

**Fig. 4.27.** HFSS model of the full antenna array (starting from the TRL reference plane).

60
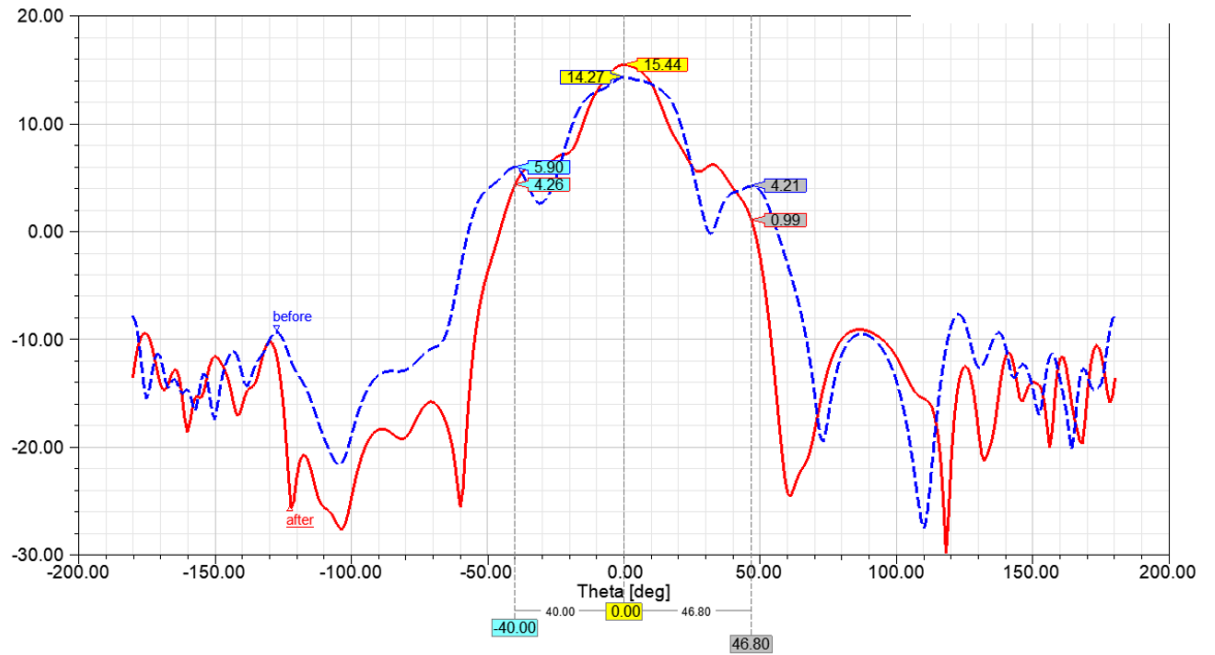
**Fig. 4.28.** Simulated radiation patterns before and after the removal of the excess microstrip line (shown in Fig. 4.26.), for the θ plane, at φ = 0º.

## 4.6.3. Simulation and Experimental Results Comparison

In this section, a comparison and discussion is done between simulated and measured results, with the manufactured 4x4 antenna array and TRL calibration kit depicted in Fig. 4.34 and the anechoic chamber environment depicted in Fig. 4.35.



| Name | X | Y |
|---|---|---|
| simulated_array | 100.5000 | -40.6661 |
| array_5 | 100.1500 | -32.7918 |
| array_1 | 100.3500 | -29.4999 |

**Fig. 4.29.** Comparison between simulated and measured reflection coefficient of the full antenna array (from Fig. 4.27.).

A total of eight copies of each PCB were manufacture, but only a few TRL kits and only some antenna array radiation patterns were measured due to time restrictions. The TRL kit results will be mentioned later on.

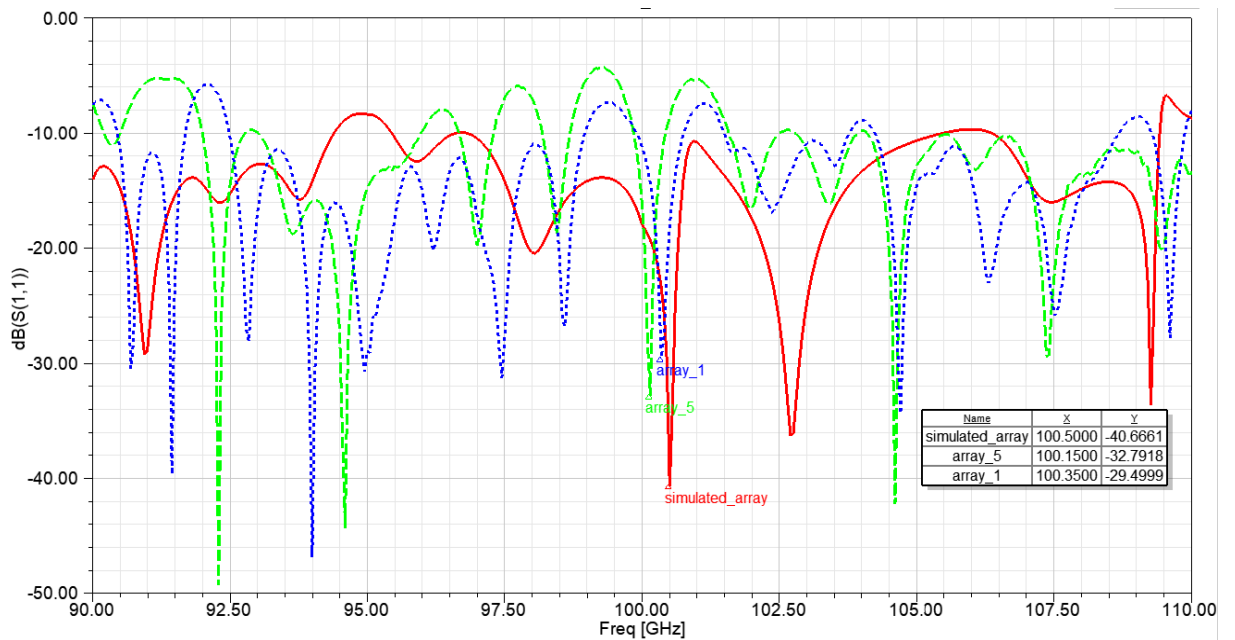Starting with the reflection coefficient, it is worth mentioning that after measuring the reflection coefficient of all arrays and analysing the overall behaviour of all the fabricated antenna arrays, two of the antenna arrays, depicted in Fig. 4.29. (represented in dashed lines), present a good similarity with simulated result regarding the resonant peak near the frequency of 100 GHz. The rest of the fabricated and, specifically the reflection coefficient, did not exhibit as good agreement as these ones. We attribute this to the manufacture variability between samples. The investigation of the design parameters and their tolerance on the final antenna performance will be subject of future study.
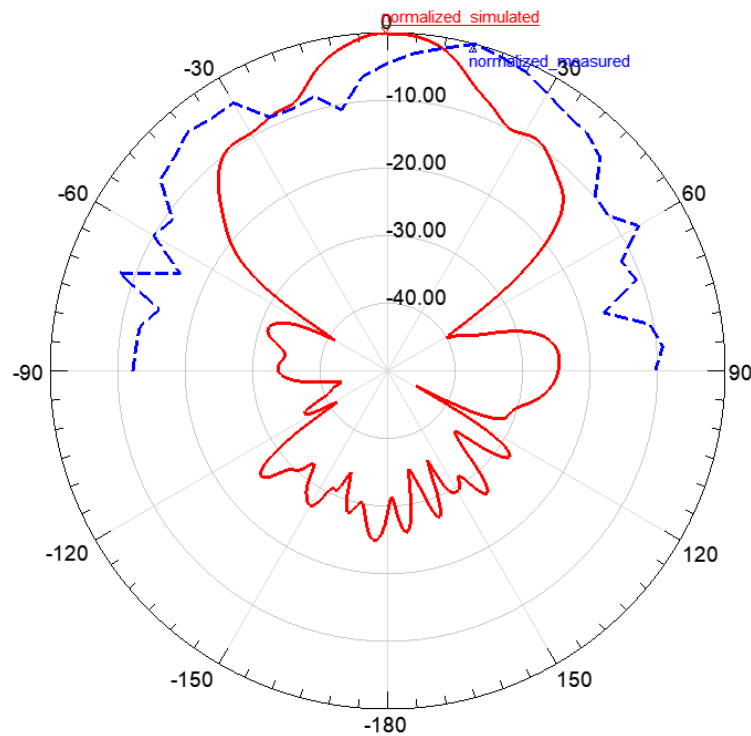


**Fig. 4.30.** Comparison between simulated and measured normalized radiation pattern of the full antenna array, for the θ plane, at φ = 0º (from Fig. 4.27.).

In terms of the radiation pattern measurements, simulated and measured results, presented in Fig. 4.30, the measured radiation pattern depicted is from array_1 (blue short dashed line from Fig. 4.29), which has a reasonable fractional bandwidth percentage roughly between 92.5 GHz and 99 GHz. Experimental measurements differ significantly from the numerical simulation at larger angles, yet with better match for small angles.

At this stage it is important to mention that the current experimental measurement setup has a few issues regarding the accuracy and reliability of the measurements themselves. Two possible issues, which require further investigating and testing, are: i) The cable used to connect the AUT to port 2, of the PNA N5224B using the WR-10+ VDI frequency extension

modules, is semi-rigid and robust, still allowing some bending, it is observed that while the positioner is rotating, hence twisting and bending the cable occurs, degradation of the reflection coefficient is observed. ii) Another possible problem is that, since the cable is somewhat limited in length, when the positioner reaches $0^o$ or $180^o$, it tends to push the AUT out of position, compromising the radiation pattern angle direction. Other arrays were also measured, to discard any possibility of a fabrication defect, but comparable behaviour was observed, leading to believe that there might be some issue in the antenna array structure itself, namely associated with manufacturing precision constraints. In the latter case, it is important to note that, during the manufacturing process, a via can be placed within a certain radius of its intended position, also known as annular ring. One specific crucial via placement is the inductive post location in the 1x4 power divider, presented in Fig. 4.31, as its position is extremely important to maintain the power divider component matched for the frequency band of interest.

A parametric sweep of the via position, shifted in 0.15 mm in multiple directions, in regard to its default position, was performed and its simulated results of the reflection coefficient and radiation pattern are depicted in Fig. 4.32 and Fig. 4.33 respectively. It can be observed that, if the via is not placed exactly as specified in the simulations, it can moderately impact the obtained reflection coefficient of the full antenna array. However, the same cannot be said of the obtained simulated radiation patterns, meaning that the manufacture tolerance of the position of said vias does not explain the difference observed between simulated and measured radiation pattern results from Fig. 4.30. It is also worth mentioning that the possible problems previously referred are only probable causes to the observed discrepancies. This will still require further study to ascertain the validation and explain better the obtained results.
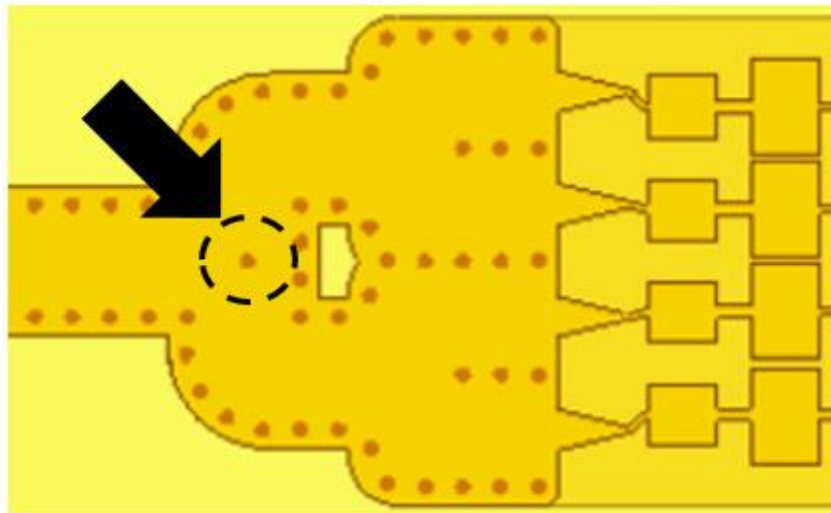


**Fig. 4.31.** Partial image of the HFSS model for the 1x4 power divider showcasing the mentioned crucial via.

**Fig. 4.32.** Simulated reflection coefficient variations of the via position of the 1x4 power divider (regarding Fig. 4.31.), using the full antenna array HFSS model.



**Fig. 4.33.** Simulated radiation pattern variations of the via position of the 1x4 power divider (regarding Fig. 4.31.), using the full antenna array HFSS model (θ plane, at φ = 0°).

64
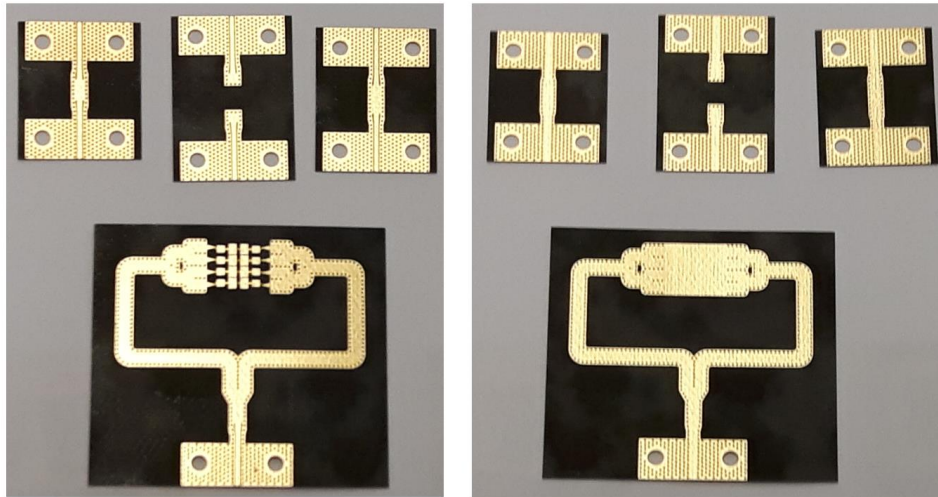
**Fig. 4.34.** Manufactured SIW 4x4 Antenna Array and TRL Calibration Kit.



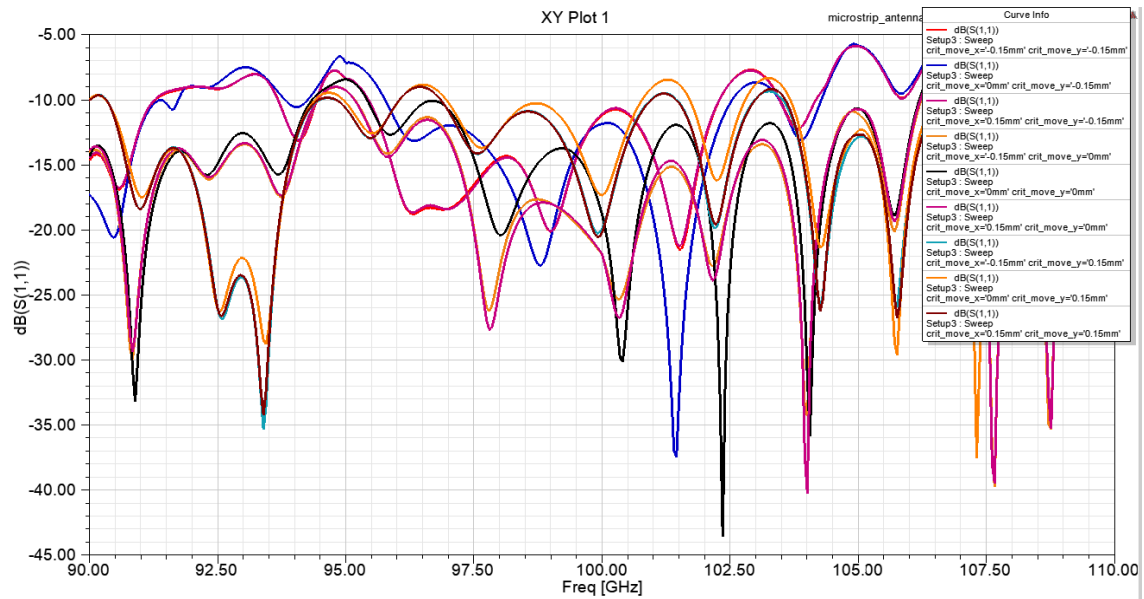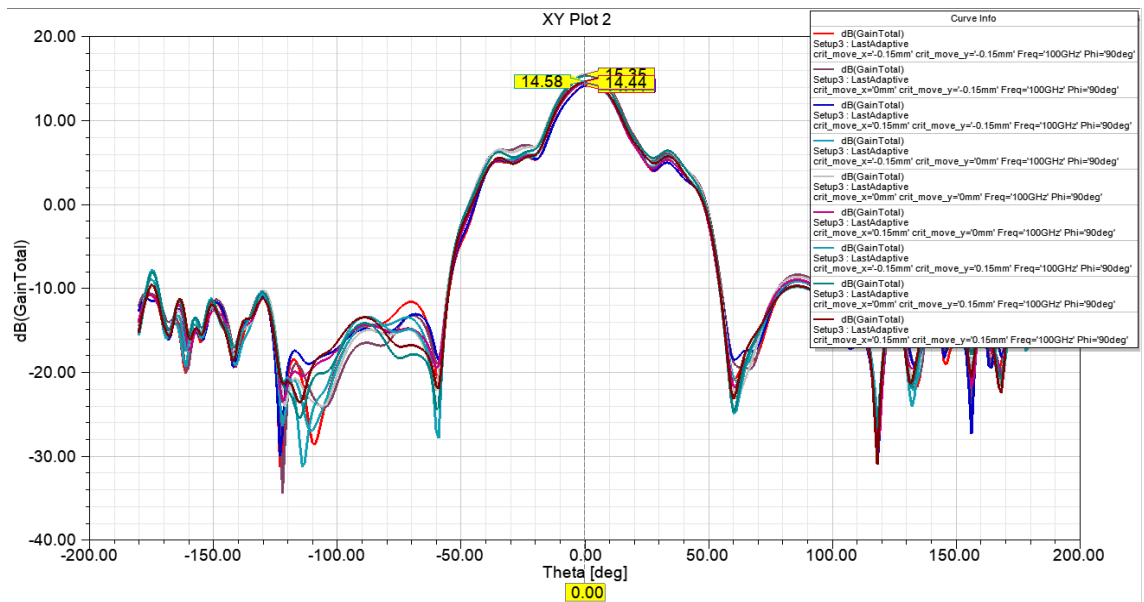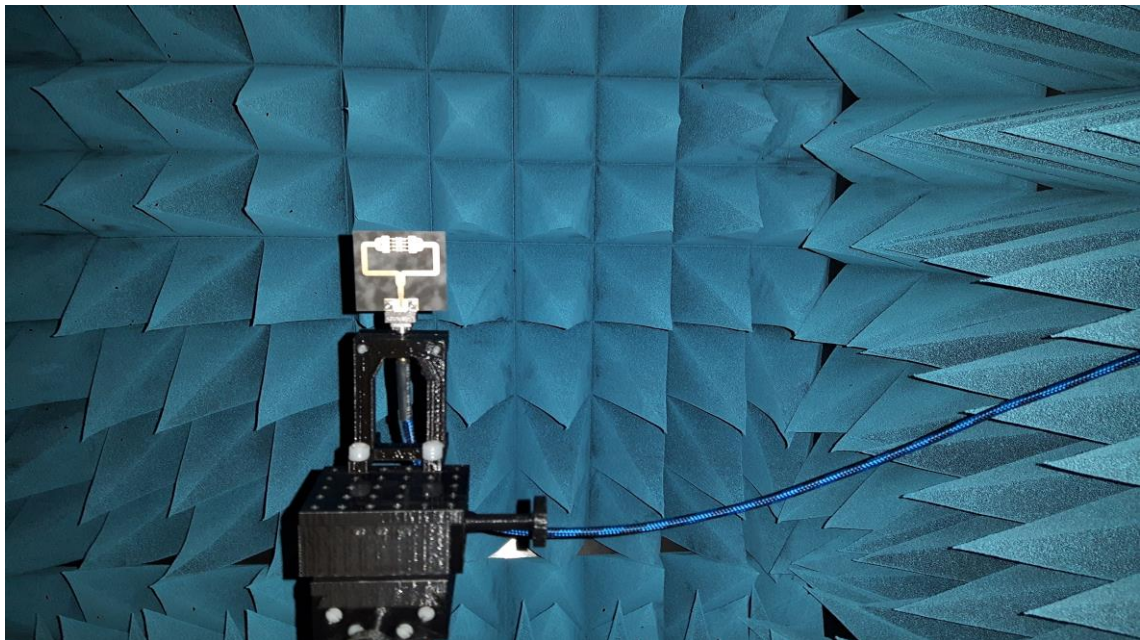**Fig. 4.35.** Anechoic Chamber environment (measurement of the 4x4 antenna array).

## 4.7. TRL Calibration Kit

As mentioned previously, the manufactured TRL calibration kit is presented also in Fig. 4.34. Most of the theory regarding the TRL calibration method and kit design rules were already discussed in Chapter 3, and the same methodology was also applied to the design of this kit. A HFSS schematic representing the reference port planes of each standard is presented in Fig. 4.36. Regarding the line standard, and comparing with the through standard, there was only an increase in one via, disregarding the via halves from each side of the line standard, which is equivalent to a transmission coefficient phase of approximately $\approx 150^o$. Applying the offset

delay formula to this case as well, it was obtained a value of 5.44 ps to be inserted in the VNA. Only one kit was measured and a similar S21 phase in the line standard was obtained, with a value of approximately $\approx 145^o$.

The simulation and measured results can be seen in Fig. 4.37 and Fig. 4.38 respectively.
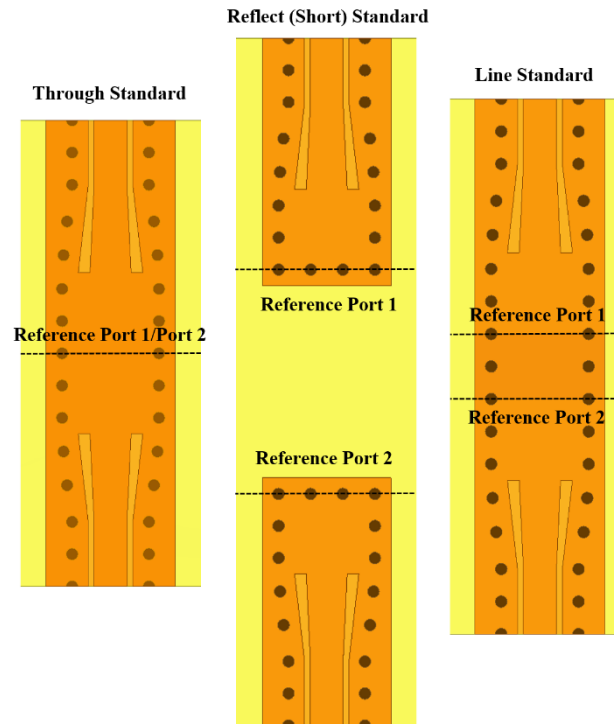


**Fig. 4.36.** HFSS model of the SIW Calibration Kit Standards.
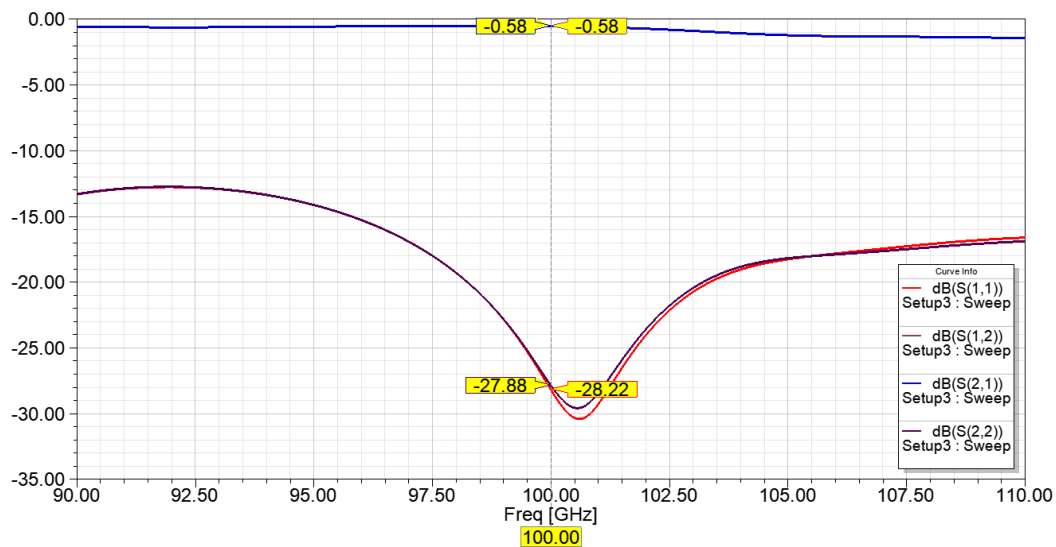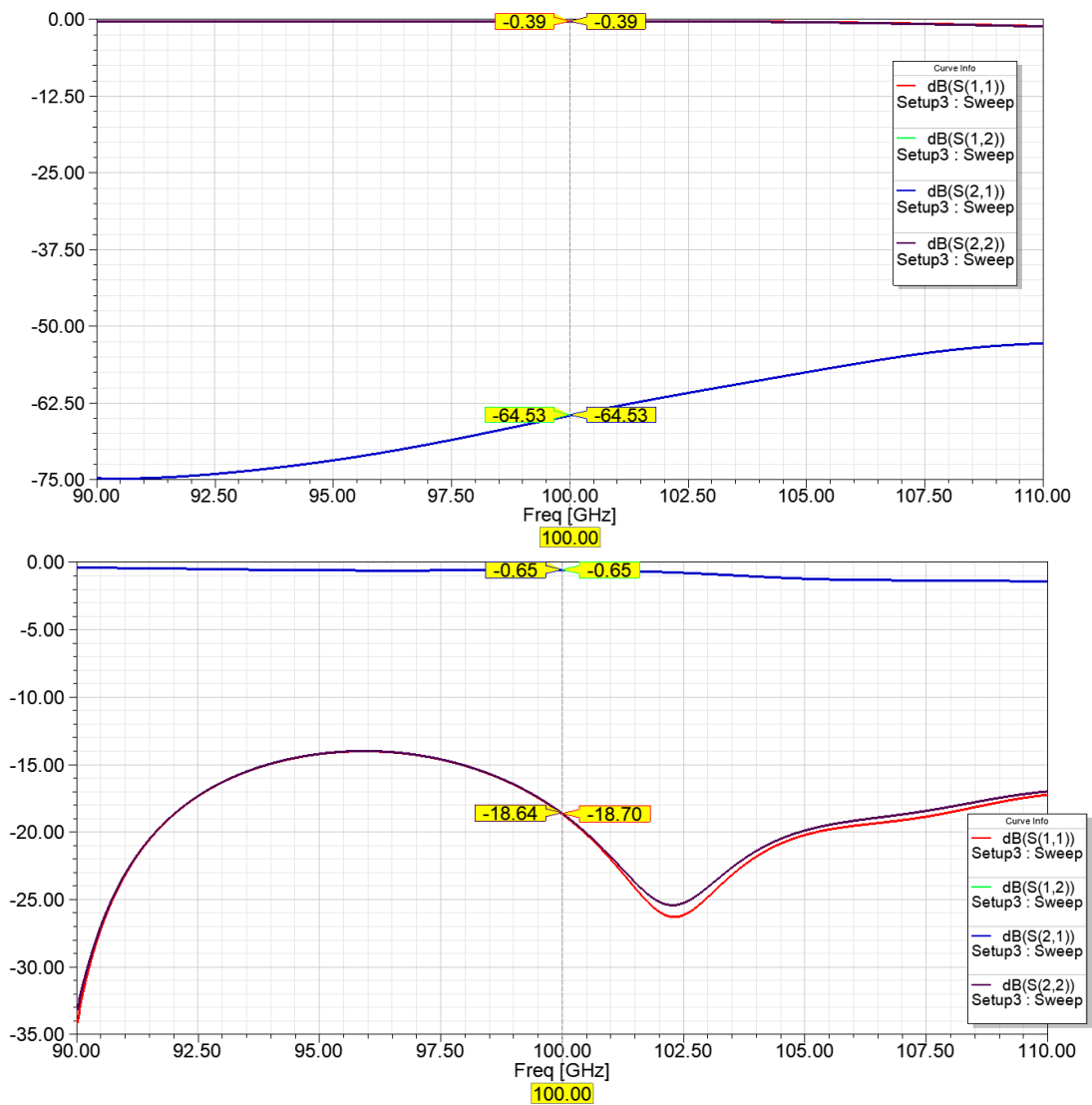
**Fig. 4.37.** Simulated S-Parameters of the Through (top), Reflect (Short) (middle) and Line (bottom) standards.
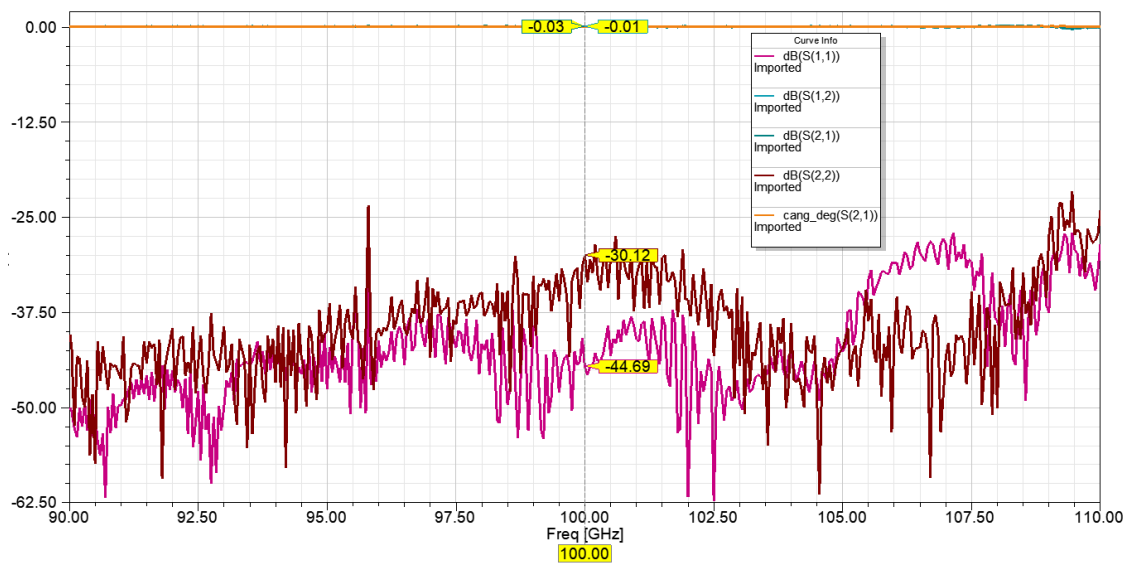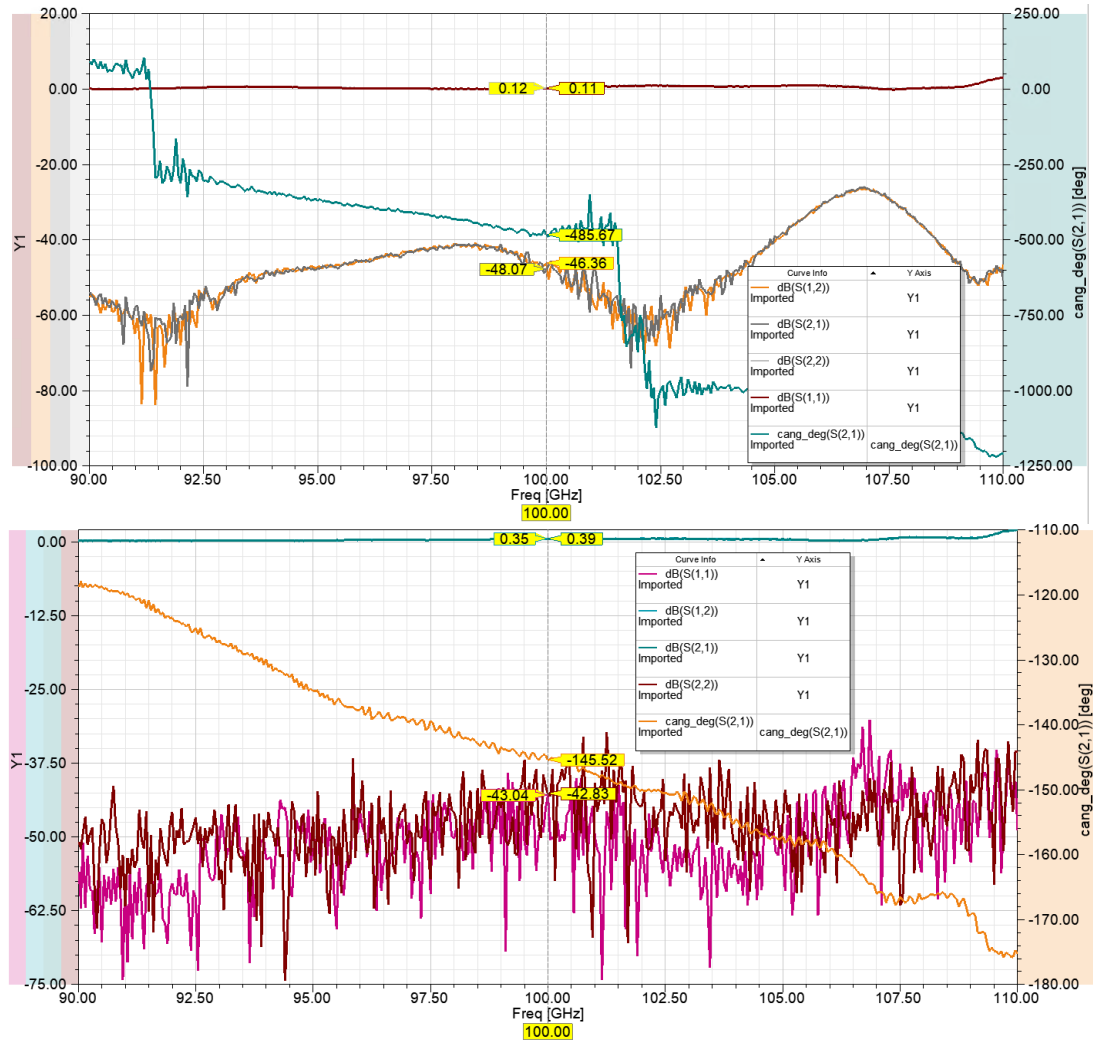
**Fig. 4.38.** Measured S-Parameters of the Through (top), Reflect (Short) (middle) and Line (bottom) standards.

## 4.8. Conclusions

In this chapter, a 4x4 differential series-fed antenna array and its corresponding TRL calibration kit was designed, fabricated and experimentally measured, observing some discrepancies with the simulated results, leaving us to believe that, apart from some minor issues regarding the measurement setup, there is a considerable possibility that the manufacturer's accuracy and precision in via placement wasn't enough to obtain a fabricated PCB almost identical to the simulated HFSS model. Concerning the TRL calibration kit, it showed good agreement regarding the excepted behaviour of each standard and its S-parameters/transmission coefficient phase.

# Chapter 5: Concluding Remarks

In this thesis, a cost effective antenna element and antenna array and its corresponding TRL calibration kits were designed, manufactured and experimentally measured to work in the sub-Terahertz range, at an operation frequency of 100 GHz. This work focused on exploring known antenna feeding techniques and reliable transmission lines that were compatible with the use of a single substrate layer, given the complexity and cost associated with the fabrication of very small PCBs for sub-Terahertz applications. The objective was to test apply already known RF frequency concepts to the millimetre wave spectrum, analysing its behaviour, performance and accuracy.

In Chapter 3, a squared loop fed CPW antenna element is described, exploring the use of a CPW feed line at frequencies around 100 GHz for a single patch antenna, having obtained a good agreement between simulated and measured results.

In Chapter 4, a differential series-fed 4x4 antenna array is presented, using a SIW transmission line type for the feed network. The analysis of the performance of array feeding configurations, such as corporate and series feed networks, as well as transmission line types such as CPW, GCPW and SIW, was performed. Given that radiation loss dominates at millimetre wave frequencies, many issues and restrictions/limits were identified, regarding the application of certain techniques and the manufacturing accuracy process for small sized PCBs, reducing the list of reliable and realizable feeding structures to be applied in this frequency domain.

The goals set for this thesis were completed and can provide some contribution to the state-of-art regarding the design of antenna structures that perform infallible at the millimetre wave spectrum. Upon the inspection of the obtain results in this work, and labelled as future work, further investigation will be necessary, concerning the manufacture accuracy constraints and the improvement of the used experimental measurement setup so that future works in the millimetre wave domain can be measured easily, accurately and reliably.

# References

[1] Celik, A. and Alouini, M.-S. (n.d.). Wireless Data Center Networks: Advances, Challenges, and Opportunities. [online] . Available at: https://arxiv.org/pdf/1811.11717.pdf.

[2] Akyildiz, I.F., Jornet, J.M. and Han, C. (2014). Terahertz band: Next frontier for wireless communications. Physical Communication, 12, pp.16–32.

[3] Rappaport, T.S., Xing, Y., Kanhere, O., Ju, S., Madanayake, A., Mandal, S., Alkhateeb, A. and Trichopoulos, G.C. (2019). Wireless Communications and Applications Above 100 GHz: Opportunities and Challenges for 6G and Beyond. *IEEE Access*, [online] 7, pp.78729–78757. Available at: https://wireless.engineering.nyu.edu/presentations/Ted_mmWC_02.28.2019Final.pdf.

[4] Ramachandran, Kishore & Kokku, Ravi & Mahindra, Rajesh & Rangarajan, Sampath. (2008). 60 GHz Data-Center Networking: Wireless ⇒ Worry less?. NEC Research Paper. 1.

[5] Webber, J., Kamoda, H., Kukutsu, N. and Kumagai, T. (2015). Millimeter-wave wireless communication in a data center cabinet with adaptive control of propagation. *2015 21st Asia-Pacific Conference on Communications (APCC)*.

[6] Hamza, A., Deogun, J. and Alexander, D. (2016). Wireless Communication in Data Centers: A Survey. *CSE Journal Articles*. [online] Available at: https://digitalcommons.unl.edu/csearticles/140/.

[7] Zhang, Z., Xiao, Y., Ma, Z., Xiao, M., Ding, Z., Lei, X., Karagiannidis, G. and Fan, P. (2019). 6G Wireless Networks: Vision, Requirements, Architecture, and Key Technologies. *IEEE Vehicular Technology Magazine*. [online] Available at: https://www.semanticscholar.org/paper/6G-Wireless-Networks%3A-Vision%2C-Requirements%2C-and-Key-Zhang-Xiao/ffa6396d0749697fc11e24a5d9ce53f8bf10c1fc.

[8] HORIZON 2020 Milestone: Final proposed Title: Report on the design and simulation of THz integrated antennas. (2019). [online] . Available at: https://terapod-project.eu/wp-content/uploads/2019/05/TERAPOD-D3.4-Report-design-and-simulation-of-THz-integ-antennas.pdf.

[9] Topak, E., Hasch, J., Wagner, C. and Zwick, T. (2013). A Novel Millimeter-Wave Dual-Fed Phased Array for Beam Steering. *IEEE Transactions on Microwave Theory and Techniques*, 61(8), pp.3140-3147.

[10] Han, C., Wu, Y., Chen, Z. and Wang, X. (n.d.). *Terahertz Communications (TeraCom): Challenges and Impact on 6G Wireless Systems*. [online] . Available at: https://arxiv.org/pdf/1912.06040.pdf.

[11] Xing, Y. and Rappaport, T. (2018). *Propagation Measurement System and Approach at 140 GHz-Moving to 6G and Above 100 GHz*. [online] , pp.1–6. Available at: https://arxiv.org/pdf/1808.07594.pdf.

[12] Santos, H.M.G.P. dos (2020). Antenna Design for Integration into Active Devices Targeting 5G and Beyond. *repositorio-aberto.up.pt*. [online] Available at: https://hdl.handle.net/10216/128602.

[13] Balanis, C.A. (1992). Antenna theory: a review. *Proceedings of the IEEE*, 80(1), pp.7–23.

[14] Balanis, C.A. (2016). *Antenna theory analysis and design*. Hoboken, New Jersey Wiley.

[15] Hillbun, M. (n.d.). *Practical Antennas 1 1.1 1.2 Antenna Measurements*. [online] . Available at: https://ewh.ieee.org/r6/scv/aps/archives/2010Hillbun.pdf.

[16] Antenna Measurement, "Antenna measurement theory," Keysight.com. [Online]. Available: https://www.keysight.com/upload/cmc_upload/All/ORFR-Theory.pdf.

[17] Rabbani, M.S. and Ghafouri-Shiraz, H. (2015). Size improvement of rectangular microstrip patch antenna at MM-wave and terahertz frequencies. *Microwave and Optical Technology Letters*, 57(11), pp.2585-2589.

[18]     www.antenna-theory.com. (n.d.). *Microstrip Antennas: The Patch Antenna*. [online] Available at: https://www.antenna-theory.com/antennas/patches/antenna.php.

[19]     Liu, Jingtian & Chen, Shuming & Xiao, Ke & Chen, Xiaowen. (2019). 100 GHz Silicon-based micro-machined patch antenna and arrays. The Journal of Engineering. 2019. 10.1049/joe.2019.0241.

[20]     Microstrip, Stripline, CPW, and SIW Design. (n.d.). [online] . Available at: https://www.qsl.net/va3iul/Microstrip_Stripline_CPW_Design/Microstrip_Stripline_an d_CPW_Design.pdf.

[21]     Pozar, D.M. (2012). *Microwave engineering*. Hoboken, Nj: Wiley.

[22]     Rainee Simons (2001). *Coplanar waveguide circuits, components, and systems*. New York: John Wiley.

[23]     Menzel, W. and Grabherr, W. (1991). A microstrip patch antenna with coplanar feed line. *IEEE Microwave and Guided Wave Letters*, [online] 1(11), pp.340–342. Available at: https://ieeexplore.ieee.org/document/93905.

[24]     Preuss, V.H.B. and Sousa, F.R. de (2019). *A Study on Low-Cost Calibration Kits for U.FL Connector Systems*. [online] IEEE Xplore. Available at: https://ieeexplore.ieee.org/document/8868761.

[25]     Chai, W., Zhang, X. and Liu, J. (2007). Characteristics Study of Four Coplanar Waveguide Feeding Devices. *PIERS Online*, 3(1), pp.48–51.

[26]     Milijić, M., Nešić, A. and Milovanović, B. (2017). *Study of dielectric substrate effect on modelling CPW-fed slot antenna arrays*. [online] IEEE Xplore. Available at: https://ieeexplore.ieee.org/document/8246239.

[27]     Ghosh, B., Antar, Y.M.M., Petosa, A. and Ittipiboon, A. (2004). Feed configurations of CPW fed DRA. *IEEE Antennas and Propagation Society Symposium, 2004.*

[28]     Agilent Technologies. "Advanced calibration techniques for vector network analyzers" Umd.edu.                     [Online].                     Available: http://anlage.umd.edu/Agilent_Advanced_VNA_calibration.pdf.

[29]     Keysight (n.d.). *Specifying Calibration Standards and Kits for Keysight Vector Network Analyzers*.     [online]     Keysight.     Available     at: https://www.keysight.com/zz/en/assets/7018-01375/application-notes/5989-4840.pdf.

[30]     Fleury, J., & Bernard, O. (2001). Designing and Characterizing TRL Fixture Calibration Standards for Device Modeling.

[31]     Alley, C.L. and Atwood, K.W. (1973). *Electronic engineering*. New York: John Wiley And Sons.

[32]     www.microwaves101.com.     (n.d.). *TRL calibration*.     [online]     Available     at: https://www.microwaves101.com/encyclopedias/trl-calibration.

[33]     Vector Star and Shock Line, "Theory and Methodology," Cdn-anritsu.com. [Online]. Available:     https://dl.cdn-anritsu.com/en-us/test-measurement/files/Application-Notes/Application-Note/11410-00492C.pdf.

[34]     Mailloux, R.J. (2018). *Phased array antenna handbook*. Norwood, Ma Artech House.

[35]     Khattak, M., Siddique, O., Ahmed, W., Sven-, E. and Sandström (2011). *Degree Project Design and Simulation of Microstrip Phase Array Antenna using ADS*. [online] . Available at: http://www.diva-portal.org/smash/get/diva2:417327/fulltext01.

[36]     Zivanovic, B. (2012). Series-Fed Aperture-Coupled Microstrip Antennas and Arrays. *Graduate     Theses     and     Dissertations*.     [online]     Available     at: https://scholarcommons.usf.edu/etd/4425/.

[37]     Bochra, R., Mohammed, F., & Tao, J. (2011). Design of optimal chamfered bends in Rectangular Substrate Integrated Waveguide.

[38]     Simpson, J.J., Taflove, A., Mix, J.A. and Heck, H. (2006). Substrate integrated waveguides optimized for ultrahigh-speed digital interconnects. *IEEE Transactions on Microwave Theory and Techniques*, [online] 54(5), pp.1983–1990. Available at: https://ieeexplore.ieee.org/document/1629040.

[39] www.microwaves101.com. (n.d.). *Microwaves101 | Substrate Integrated Waveguide*. [online] Available at: https://www.microwaves101.com/encyclopedias/substrate-integrated-waveguide.

[40] Kazemi, Robab & Sadeghzadeh, Ramezan & Fathy, Aly. (2012). Design of a wide band eight-way compact SIW power combiner fed by a low loss GCPWTO-SIW transition. Progress In Electromagnetics Research C. 26. 10.2528/PIERC11110909.

[41] Tang, W.X., Zhang, H.C., Liu, J.F., Xu, J. and Cui, T.J. (2017). Reduction of radiation loss at small-radius bend using spoof surface plasmon polariton transmission line. *Scientific Reports*, [online] 7(1), p.41077. Available at: https://www.nature.com/articles/srep41077.

[42] Bouchra, R. and Amina, A. (2019). Development of Ku Compact Broadband 1x4, 1x8 and 1x16 Power Dividers with SIW Optimized Chamfered Bends. *Electrical and Electronic Engineering*, [online] 9(1), pp.17–26. Available at: http://article.sapub.org/10.5923.j.eee.20190901.03.html.

[43] Nawaz, M.I., Hui-ling, Z. and Kashif, M. (2014). *Substrate Integrated Waveguide (SIW) to Microstrip Transition at X-Band*. [online] undefined. Available at: https://www.semanticscholar.org/paper/Substrate-Integrated-Waveguide-(SIW)-to-Microstrip-Nawaz-Hui-ling/7a3baa27c860d5c19672581b5b45a65a39b19cb6.

[44] Prakoso, Teguh & Ngah, R. & Abd Rahman, Tharek. (2008). Representation of antenna in two-port network s-parameter. 10.1109/RFM.2008.4897428.

[45] www.antenna-theory.com. (n.d.). *S-Parameters for Antennas (S11, S12, ...)*. [online] Available at: https://www.antenna-theory.com/definitions/sparameters.php.

[46] Zhang, C., Lai, Q. and Gao, C. (2017). Measurement of active S-parameters on array antenna using directional couplers. *2017 IEEE Asia Pacific Microwave Conference (APMC)*.

[47] Albert, Chirappanath. (2017). Comparative Analysis of Antenna Array Radiation Patterns Under the Influence of Number of Elements and Spacing between the Elements with Uniform and Non-uniform Excitations. 10.13140/RG.2.2.22180.37760.

[48] Urbanec, T. and Lácík, J. (2016). *Compact size substrate integrated waveguide phase shifter*. [online] IEEE Xplore. Available at: https://ieeexplore.ieee.org/document/7477427.